Ph. D. Thesis
박사 학위논문

Compact Bone Drilling Robotic System with High Rigidity

Seongbo Shim (심 성 보 沈 晟 輔)

Department of
Robotics Engineering

DGIST

2020

Ph. D. Thesis
박사 학위논문

Compact Bone Drilling Robotic System with High Rigidity

Seongbo Shim (심 성 보 沈 晟 輔)

Department of
Robotics Engineering

DGIST

2020

Compact Bone Drilling Robotic System with High Rigidity

Advisor : Professor Jaesung Hong

Co-advisor : Professor Sanghyun Joung

by

Seongbo Shim
Department of Robotics Engineering
DGIST

A thesis submitted to the faculty of DGIST in partial fulfillment of the requirements for the degree of Ph. D. of Science in the Department of Robotics Engineering. The study was conducted in accordance with Code of Research Ethics[1]

01.03.2020

Approved by

Professor Jaesung Hong (Advisor) (signature)

Professor Sanghyun Joung (Co-Advisor) (signature)

[1] Declaration of Ethical Conduct in Research: I, as a graduate student of DGIST, hereby declare that I have not committed any acts that may damage the credibility of my research. These include, but are not limited to: falsification, thesis written by someone else, distortion of research findings or plagiarism. I affirm that my thesis contains honest conclusions based on my own careful research under the guidance of my thesis advisor.

Compact Bone Drilling Robotic System with High Rigidity

Seongbo Shim

Accepted in partial fulfillment of the requirements for the degree of Ph. D. of Science.

01.03.2020

Head of Committee	Prof. Jonghyun Kim	(signature)
Committee Member	Prof. Jaesung Hong	(signature)
Committee Member	Prof. Joonho Seo	(signature)
Committee Member	Prof. Dongwon Yun	(signature)
Committee Member	Prof. Sanghyun Joung	(signature)

Ph.D/RT
201533005

심 성 보. Seongbo Shim. Compact Bone Drilling Robotic System with High Resolution and Rigidity. Department of robotics Engineering. 2020. 70p. Advisors Prof. Jaesung Hong, Co-Advisors Prof.

ABSTRACT

One of the most important and difficult tasks during the bone drilling is to guide the orientation of the drilling axis for the target and to maintain the orientation against the reaction force of drilling during the procedure. To assist the drilling task, a remote center of motion (RCM) mechanism is proper for aligning the orientation without changing the entry point. However, existing RCM mechanisms do not provide sufficient resolution and rigidity to deal with hard tissues. We proposed a new type of RCM mechanism which uses two pairs of linear actuators and gearless-arc guide. For the drilling motion, we designed a single motor-based 2-axis control mechanism based on the rolling friction. In addition, a release mechanism for instant stopping of the drilling motion as requested was added. For the automatic control of guiding and drilling, a CT based navigation system with an optical tracking system was incorporated. The effectiveness of the integrated robotic system was demonstrated in a series of experiments and ex-vivo drilling test on swine femurs. The proposed robotic system withstood an external force of up to 51 N to maintain the joint angle, and an average targeting error was less than 1.2 mm.

Keywords: Bone drilling, drilling mechanism, image guided navigation, remote center of motion mechanism

Contents

List of contents

List of tables

List of figures

I. INTRODUCTION

1.1 Introduction of Bone Drilling

Bone drilling is a frequently operated procedure in a number of surgical fields, including the orthopedic, ear, maxillofacial, and neural [1]–[6]. A bone biopsy is one example of such a drilling procedure, in which bone marrow is sampled using a biopsy needle or medical screw to penetrate the bone.

Once the target point and the path of drilling are determined, a surgeon drills a hole in the bone using a hand drill while evaluating the X-ray images acquired using portable C-arm systems. However, it is difficult to precisely align the orientation of the drill axis to the target. Even if the initial orientation is correct, it is very difficult to maintain it during the procedure owing to the strong reaction force of drilling. Accordingly, if the surgeon fails to maintain the orientation, the drilling will deviate from the planned path. As a result, an irreparable hole appears in the bone and the hole may affect subsequent trials unlike the case of the needle insertion in soft tissues, whereby the procedure can be repeated with minor complications. In addition, a number of X-ray images are necessary to identify the position of the drill during the procedure, which exposes the patient and the clinical personnel to radiation [7].

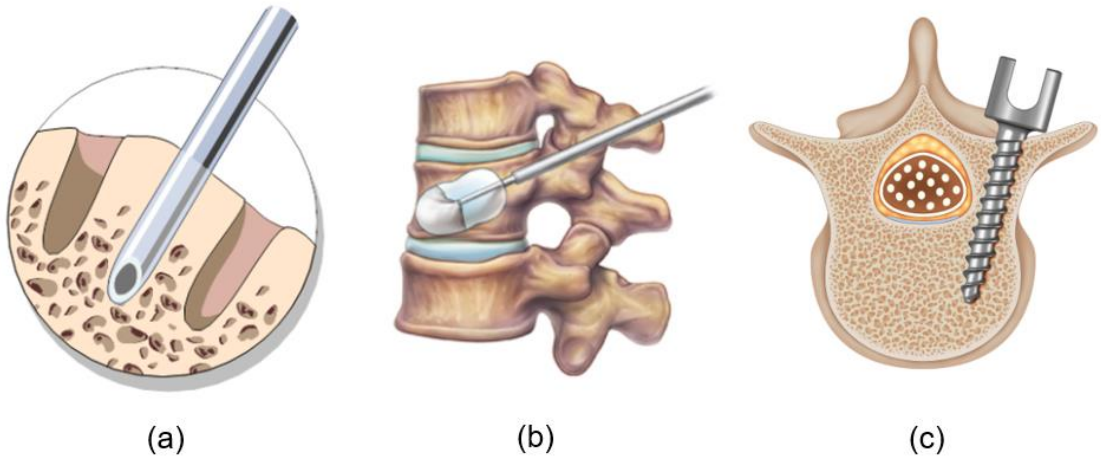

Fig. 1. Bone drilling surgery. (a) Bone biopsy, (b) vertebroplasty, and (c) pedicle screw placement

1.2 Reported Bone Drilling Robotic System

Boiadjiev et al. [8] and Molliqaj et al. [9] argued that a robotic drilling system may be an alternative to the problematic manual procedure. To achieve precise drilling and ensure minimal risks from the ionizing radiation, various robotic systems have been developed for bone drilling. Most drilling robots used a serial robot arm, which has high degrees-of-freedom (DOFs) for positioning and guiding the orientation of the drill [10]–[13]. SPINEBOT [14] and CoRA [15] utilized the prismatic joints for precise and robust XYZ positioning. Although the serial robot-arm-based drilling robot provides a smaller footprint than that of the prismatic joint robot, high-torque motors are required. Nevertheless, a relatively large footprint is still generated compared with the small surgical site. In addition, these multi-DOFs robotic system cannot ensure remote center of motion (RCM) mechanically, so that the control method becomes complicated and the stability of the RCM is reduced.

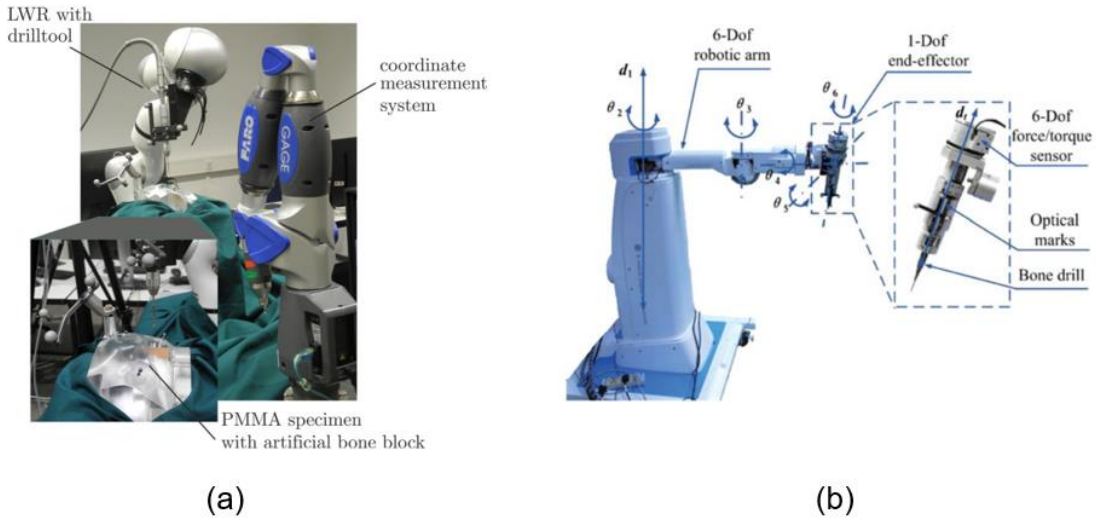

Fig. 2. Serial robot arm based drilling robot. (a) [10], (b) [13]

These existing robot systems automatically perform all the drilling procedures, which include the positioning, setting of the orientation, and insertion of the drill. In fact, the initial positioning of the drill at the entry point can be manually performed by the surgeon, and the robot is required to realize remote center of motion after its positioning at the entry point. Although the existing bone drilling robots can achieve RCM

by controlling each joint using a software program, they are unable to achieve mechanical RCM performance that makes the entire system more reliable and compact compared to the serial arm control. The effectiveness of the RCM implementation after manual position was also verified by the commercial endoscope positioner VIKY EP (Endocontrol SA, La Tronche, France).

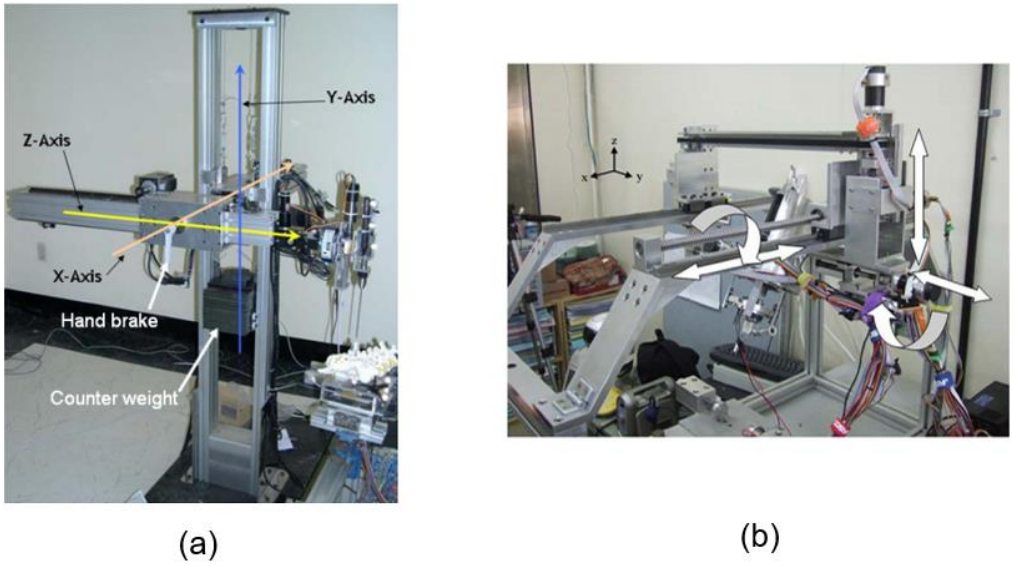

Fig. 3. Prismatic joint based drilling robot. (a) [14], (b) [15]

1.3 Challenges of the Reported Robotic System

A number of mechanical RCM systems have been developed for medical applications [16]–[23]. However, the existing RCM mechanisms are not appropriate for bone drilling because they were used only for soft tissue applications. Thus, they could not withstand the large forces applied on these mechanisms. The parallelogram RCM mechanism type is one of the most common RCM mechanisms. It contains a number of revolute joints and linkages [16]–[18], which cause large inertial moments and lead to insufficient rigidity [19]. Another common RCM mechanism is the use of a circular guided arc. To achieve RCM, the actuator needs to move along the gear on the arc link [20]–[22]. Given that the force used to support the orientation is applied entirely on the small gear part on the arc, it is not appropriate to deal with the large drilling force owing to stability and reliability issues. In addition, the requirement of manufacturing and assembly precision hinders the use of arc-type RCM mechanisms [19].

To achieve high resolution and rigidity in RCM mechanism for the bone drilling, a prototype RCM mechanism has been reported previously by the authors [23]. This mechanism is based on a trigonometric ratio and employs a pair of linear actuators and a gearless arc guide. Given that the trigonometric RCM mechanism is applied only on one axis, the resolution and rigidity of the entire mechanism is insufficient for the actual bone drilling. In addition, this preliminary study showed that the workspace of the prototype was limited within an incomplete conical shape volume owing to the space required by the motor part for the rotation of the mechanism. The proposed second version has also resolved this limitation of the previous prototype.

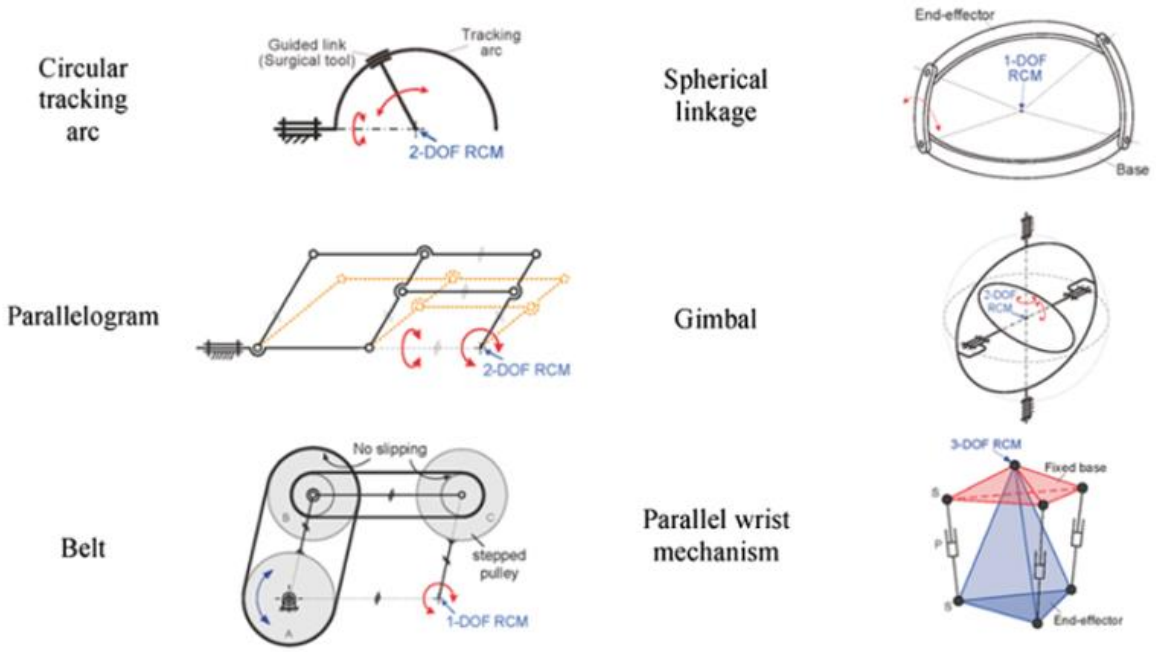

Fig. 4. Type of RCM mechanism. [Kinematic design considerations for minimally invasive surgical robots an overview]

1.4 Contribution and Research Contents

In this study, we have completed a bone drilling robotic system with novel RCM and drilling mechanisms, as shown in Fig. 1. A dual trigonometric-ratio-based RCM mechanism (DT–RCM) is proposed to provide a) sufficient resolution and rigidity for both RCM axes, and b) a complete conically shaped workspace that has a motion angle of approximately 60°. In addition, a static analysis was conducted to obtain the theoretical resolution and rigidity of the mechanism. For the drilling, we proposed a rolling-friction-based drilling mechanism with a single motor to generate the linear and rotational motions simultaneously. To enhance the surgical safety, a release mechanism was implemented, which enabled prompt and intuitive detachment of the drill part from the robot body. We also integrated it with an image-guided navigation system with the use of an optical tracking system (OTS) to drive the proposed bone drilling robot toward the bony tissue target. The feasibility of the proposed mechanism was confirmed by a series of experiments and ex vivo drilling tests on swine femurs. To the best of our knowledge, the robotic system is the first bone drilling robot that satisfies the resolution, rigidity, and safety requirements for use in conjunction with an RCM mechanism.

The remainder of this paper is organized as follows. Section II describes the proposed drilling mechanism based on rolling friction. The proposed guiding mechanism based on RCM mechanism is described in section III. Section IV presents the integrated robotic system with advanced drilling and RCM mechanisms. Section V shows experimental results of the proposed bone drilling robotic system using a phantom and swine femur samples. Section VI discusses the advantages and limitations of the proposed robotic system. Finally, section VII presents the concluding remarks.

II. ROLLING FRCITION BASED DRILLING MECHANISM

2.1 Introduction of drilling mechanism

Several robotic systems have been developed to conduct an automatic drilling procedure, as well as the guiding procedure [24–29]. Moreover, some reports have indicated that automatic drilling yields better results than manual drilling. However, surgeons still seem to prefer manual drilling because of the safety issue. For this reason, commercial robotic systems provide only a guiding function, discarding automatic drilling or insertion. Renaissance (Mazor Robotics Ltd. Caesarea, Israel) and iSYS 1 (iSYS Medizintechnik GmbH, Kitzbuehel, Austria) are some examples. Therefore, an automatic drilling system that can guarantee surgical safety from the viewpoint of surgeons should be developed by increasing the manipulability of the drilling robot. Specifically, a surgeon may wish to stop the procedure and detach the drill tip if an unexpected problem occurs. In the reported drilling mechanisms, the drill tip was mechanically connected to a rotary motor to enable a rotational drilling motion, and was serially connected to a linear motor to enable a linear drilling motion [24–29]. Therefore, it was difficult to remove the drill tip instantly during operation, because the only means of doing so required turning off the power to the robotic system and removing the entire robot with the drill tip. To increase the manipulability and enhance surgical safety, it should be possible to stop the drilling motion and detach the drill tip immediately when necessary.

In this section, we applied rolling friction as the power source for drilling for the first time. This rolling-friction-based drilling mechanism has several advantages over previous drilling mechanisms. First, it is compact in the drilling direction. In previous drilling mechanisms, large linear actuators were employed to generate the linear drilling motion [24–29]. However, in the proposed drilling mechanism, rotational and linear motion can be generated simultaneously using angled rolling friction without any linear actuator. Second, a prompt release operation can easily be achieved. Because the proposed drilling mechanism is based on rolling friction, the power transmission from the motor to the drill tip can be disconnected via a simple mechanism, enabling the drill tip to be detached from the roller even while the drilling motor is in operation.

Third, the feed of the drilling motion can be changed in a straightforward manner. Previous drilling mechanisms required the calculation of the rotary and linear motor speeds to generate a desired feed of drilling motion. However, in the proposed drilling mechanism, the feed of the drilling motion is mechanically determined by the roller angle.

The objective of this section was to develop a robotic system for automatic bone drilling. To configure the system, we designed an orientation mechanism that can precisely guide the drill, and integrated an optical navigation system to enable accurate target tracking. The proposed robotic system consists of the drilling and orientation mechanisms, which are respectively indicated by the white and black parts in Fig. 5(a). For the navigation system, a calibrated stereo camera and three reference markers are used. The reference markers provide the coordinates of the robot, drill tip, and patient.

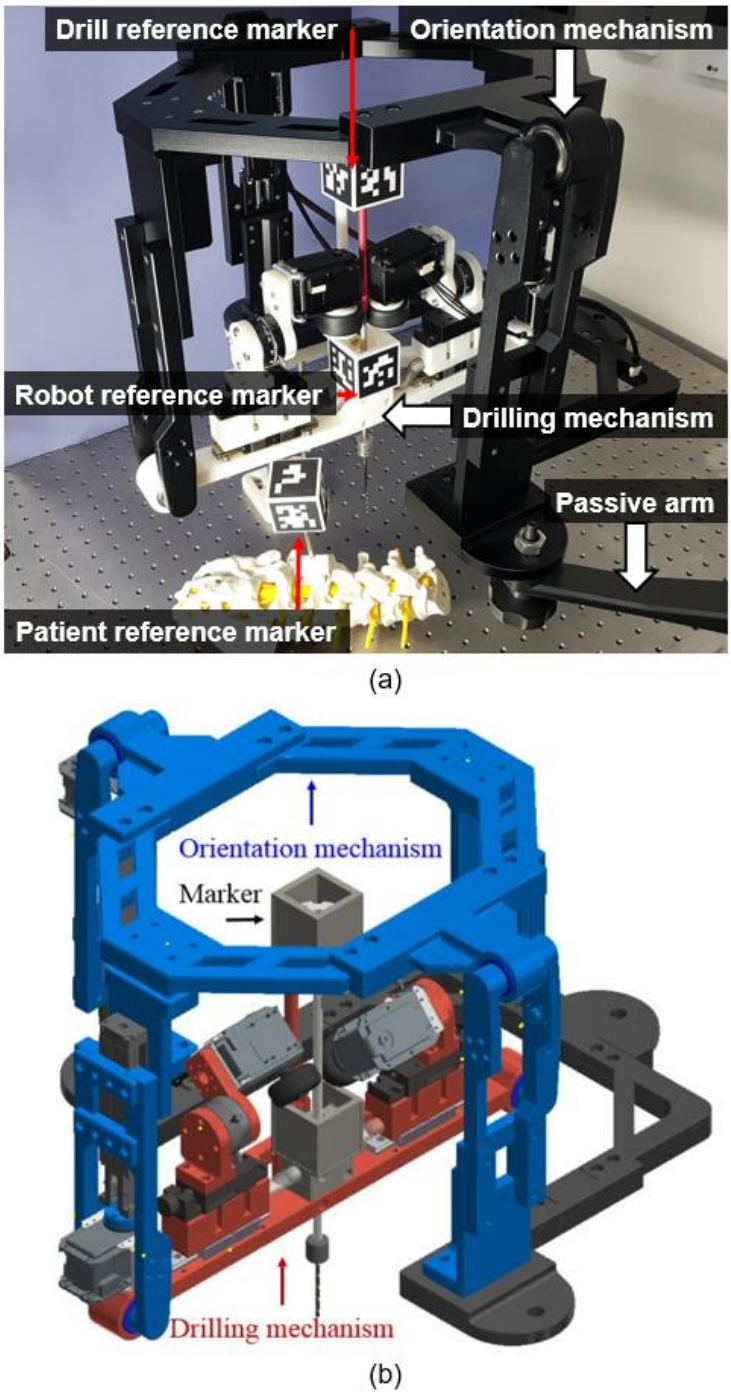

Fig. 5. (a) Configuration and (b) computer-aided design (CAD) model of the proposed robotic system

2.2 Mechanisms of robotic system

In order to generate a drilling motion and guide the drill, we designed the drilling and orientation mechanisms depicted in Fig. 5(b). Because the orientation mechanism is intended for fine orientation control, two passive arms with six degrees of freedom (DOFs) are employed at both sides of the orientation mechanism for gross positioning and to hold the robot in place.

2.1.1 Rolling Friction based Drilling Mechanism

When a roller is rotated with a normal force between itself and a cylindrical pipe, rolling friction can be induced at the contact surface between the roller and pipe. This rolling friction generates rotational and linear motions, according to the roller angle, as illustrated in Fig. 6. The rolling friction force F is given by the following:

$$F = \mu_c N, \tag{1}$$

where μ_c and N represent the coefficient of friction and normal force between the roller and pipe, respectively. Based on the rolling friction, rotational and linear drilling motions are simultaneously generated using an angled roller (see Fig. 6(c)). In other words, the force of the rolling friction is distributed into two forces to generate rotational and linear motions for drilling, according to roller angle θ, as follows:

$$F_r = \mu_c N cos\theta \tag{2}$$

and

$$F_t = \mu_c N sin\theta, \tag{3}$$

where F_r and F_t are the rotational and thrust forces applied to the pipe for the drilling motion, respectively.

Using this concept, we designed a novel drilling structure based on rolling friction, as illustrated in Fig. 7. A drill tip is attached to the bottom of a cylindrical pipe using a coupling mechanism. The pipe is guided by a linear bush, in order to fix its orientation while transmitting the rotational and thrust force without any friction. The purpose of the pipe is to translate the rotational and thrust forces from the location at which the rolling friction force is exerted to the drill tip. To generate the rolling friction, a rotating roller should be designed with a normal force between itself and the pipe. The motor to which the roller is attached is assembled with a positioning unit, in order to induce a normal force. The normal force exerted by the roller on the pipe is induced by moving the positioning unit toward the pipe. In addition, an angle-adjusting unit is located between the motor and the positioning unit, in order to change the roller angle. When the roller angle is 0°, rotational motion is induced without linear motion. The rotational and linear motions for drilling are generated by adjusting the roller angle to between 0° and 90°. To efficiently generate the rolling friction force, we applied a pair of rollers on both sides of the pipe, and line-symmetrically changed the two roller angles with respect to the pipe. Besides increasing the rolling friction force, the use of two rollers also prevents the pipe from bending as a result of the normal force. Even if the roller angles are not perfectly line-symmetrical, the linear bush ensures that the drill axis is maintained.

Unlike previous drilling mechanisms, which required linear guides equal in length to the drilling depth, the proposed drilling mechanism is compact in the drilling direction. Furthermore, the feed of the drilling motion can be adjusted by changing the roller angle. As the roller angle approaches 0°, the feed decreases. The feed of the drilling motion *f,* the translation per turn of the pipe, is calculated as follows:

$$f = 2\pi r_p \tan\theta, \tag{4}$$

where r_p and θ represent the pipe radius and angle of the roller, respectively.

We used two Maxon motors (MX-64R, Robotis Corp., Seoul, Korea) to rotate the rollers. These

motors were synchronized to minimize the speed difference between the two rollers. To increase the coefficient of friction, rubber rollers were used, and a shrinkable tube was placed on the pipe. X-axis positioning units (XKCS30, MISUMI Group Inc., Tokyo, Japan) were employed to generate normal forces between the roller and pipe. The positioning unit could hold up to 9.8 N, and the displacement of the unit was 25 mm. In addition, angle-adjusting units (REG25, MISUMI Group Inc., Tokyo, Japan) were used to change the roller angles. The unit could hold up to 9.8 N, and the angular range of the unit was 360°.

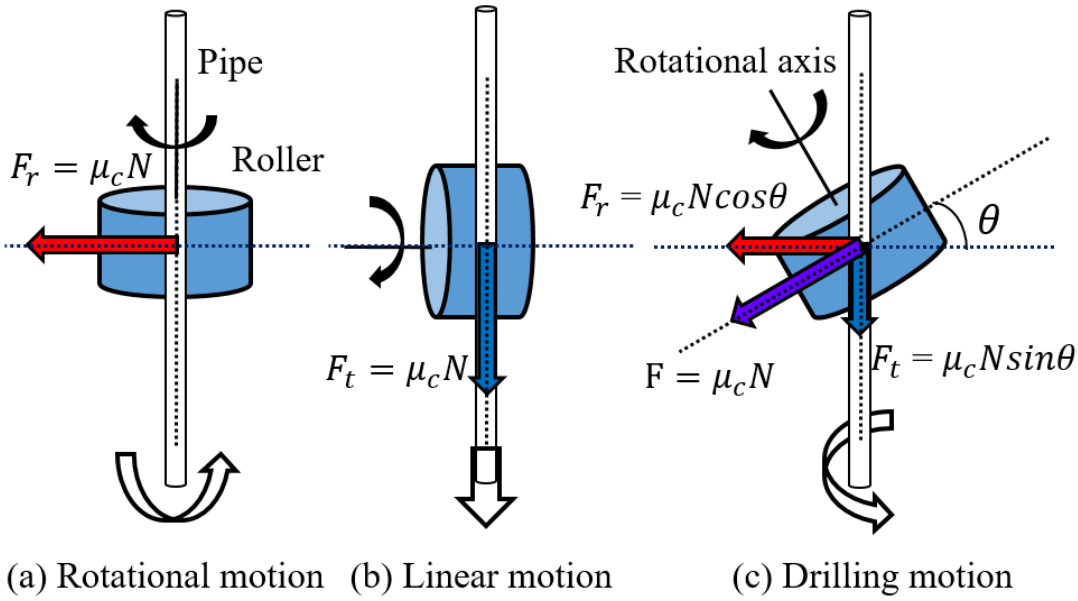

Fig. 6. Drilling motion using rolling friction.

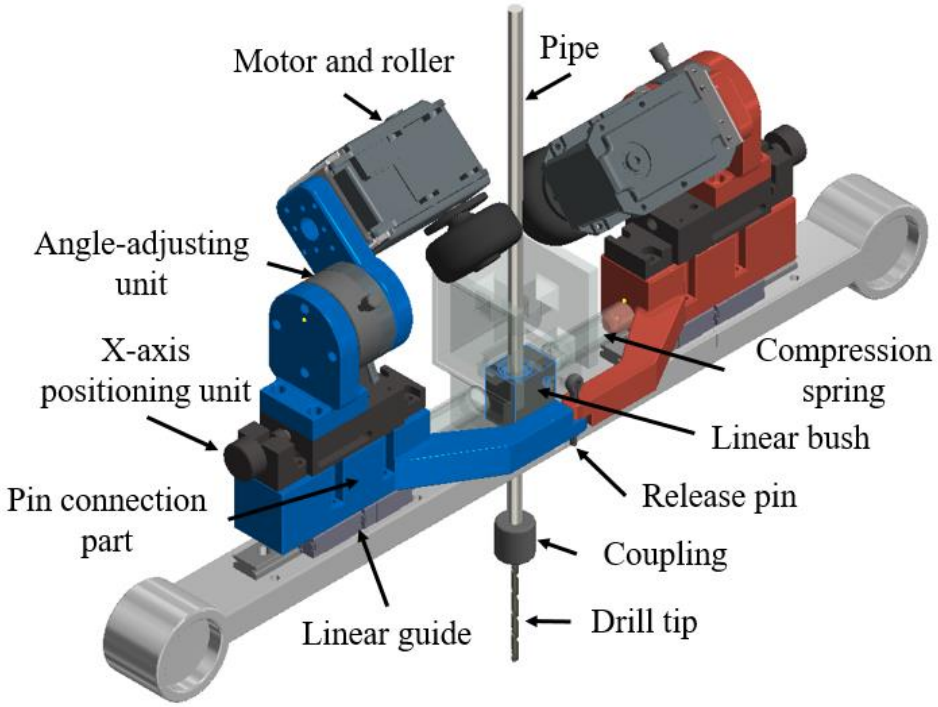

Fig. 7. CAD model of the drilling mechanism.

2.1.2 Release Mechanism

In surgical robots, the inclusion of a safety function is important. For surgical safety, the drilling robot should be designed to facilitate surgeon–robot interaction. In the case of emergencies, it should be possible to detach the drill tip from the robot instantly. One of the main advantages of the proposed rolling-friction drilling mechanism is the inclusion of an easy and quick release function. Because the power transmission method of the proposed mechanism is rolling friction, the friction force is removed by separating the roller from the pipe. As a result, the pipe connected to the drill tip can be removed from the robot, even when the motors are running.

To implement the release mechanism, we used a linear guide, compression spring, and release pin, as shown in Fig. 7. The motor part from the pin connection part to the motor with the roller was assembled in the linear guide. Because the compression springs are located between the linear bush and each motor part, a force pushing the motor parts in the opposite direction of the pipe is generated. In the operation mode, the motor parts are connected by the release pin, as shown in Figs. 7 and 8(a). This prevents the motor parts from moving away from the pipe, and allows the roller to transmit the friction force to the pipe. However, if the operator pulls the pin out, the compression springs push both motor parts back from the pipe, as shown in Fig. 8(b). Consequently, the power transmission from the rolling friction ceases, and the drill tip can be removed.

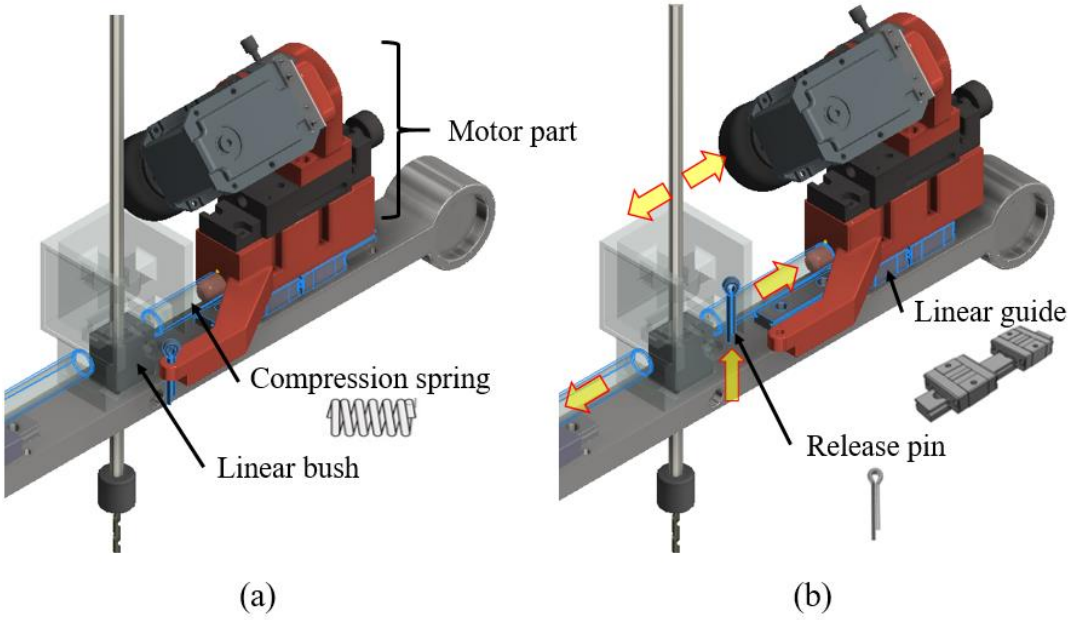

Fig. 8. Release mechanism. (a) Operation mode and (b) stop mode.

2.1.3 Orientation Mechanism

We also developed a mechanism for controlling the drill orientation. To reach the target using a guiding robot, at least two DOFs for orientation are necessary, except for the insertion motion [30, 31]. If two DOFs for positioning are added here, both the target position and insertion path can be determined, as with iSYS 1 (iSYS Medizintechnik GmbH, Kitzbuehel, Austria) and a needle guiding robot [32]. In this study, however, we designed a guiding mechanism with two DOFs to simplify the robotic system. After rough positioning is performed by the passive arms, the proposed orientation mechanism is employed to precisely guide the drill to the target point.

To design the orientation mechanism, we considered two factors. First, it was necessary for the end effector of the orientation mechanism to be connected to the bar-type drilling mechanism, whose dimensions were approximately 340 mm × 30 mm. To ensure a reliable connection between the drilling and orientation mechanisms, the end effector of the orientation mechanism should have a bar structure. Second, the orientation mechanism should have high resolution. If a target drilling point is deep, even a small orientation error

could cause significant targeting error.

To satisfy these conditions, we developed a four-bar linkage, consisting of two prismatic and two revolute joints (2P2R), as illustrated in Fig. 9. The silver base in Fig. 7 and the silver bar at the bottom in Fig. 9 are the same parts. Two of the 2P2R four-bar linkages are connected orthogonally, to provide two DOFs for orientation. The base point of the second four-bar linkage is attached to the end effector of the first four-bar linkage. The second four-bar linkage is attached by rotating 90° along the Z_E axis, and 180° along the X_E axis, based on the first four-bar linkage. Each four-bar linkage consists of two passive revolute joints, one passive prismatic joint, and one active prismatic joint, as illustrated in Fig. 10. The active prismatic joint consists of a ball-screw-based linear guide and rotary motor (MX-64R, Robotis Corp., Seoul, Korea). When the active prismatic joint is operated, the orientation of the end link between the revolute joints is changed. Unlike a conventional four-bar linkage, which directly uses a rotary actuator, we used a ball-screw-based linear actuator to ensure that the orientation mechanism would be robust against external forces and have a superior resolution.

When the linear actuator moves, the fixed revolute joint, θ_4, is rotated (see Fig. 10). Therefore, the four-bar linkage could be simplified to a two-link planar arm with one revolute joint. The relationship between the angle of the revolute joint θ_4 and the displacement of the linear actuator d_2 is given by the following:

$$\theta_4 = sin^{-1}\left(\frac{d_2}{l_E}\right), \tag{5}$$

where l_E is the length of the end link between the passive revolute joints. Fig. 11 presents a kinematic representation of the simplified orientation mechanism. The axes are labeled according to the distal Denavit–Hartenberg (D-H) conventions, and the corresponding D-H parameters are listed in Table I. To understand the kinematic model intuitively, we consider the frame of joint E1, which is the end effector of the first four-bar linkage. Joints 1 and 2 are revolute joints, and joint E2 is the end effector of the entire orientation mechanism. Joint C connects joints E1 and 2. Because it is not possible to express the relationship between joints

2 and E1 directly using D-H notation, joint C must be employed. The dimensions shown in Fig. 11 are as follows: l_1 = 270 mm and l_2 = 170 mm. The end link is 340 mm long, and the displacement of the linear guide (LX1502C-B1-N-100, MISUMI Group Inc., Tokyo, Japan) is approximately 60 mm. Substituting these values into (5) yields yaw and pitch rotation ranges of approximately 10° each. The resolution of the orientation mechanism, $\theta_{res,}$ is given by the following:

$$\theta_{\mathrm{res}} = \left(tan^{-1}\frac{\mathrm{L_{bs}}}{\mathrm{l_E}}\right) \times \left(\frac{\theta_{\mathrm{res.M}}}{360°}\right), \tag{6}$$

where $\mathrm{L_{bs}}$ is the lead of the ball-screw-based linear guide, and $\theta_{\mathrm{res.M}}$ is the resolution of the motor in the linear actuator. Because the lead of the linear guide is 2 mm, and the resolution of the motor is 0.088°, the resolution of the orientation mechanism is approximately 0.0001°.

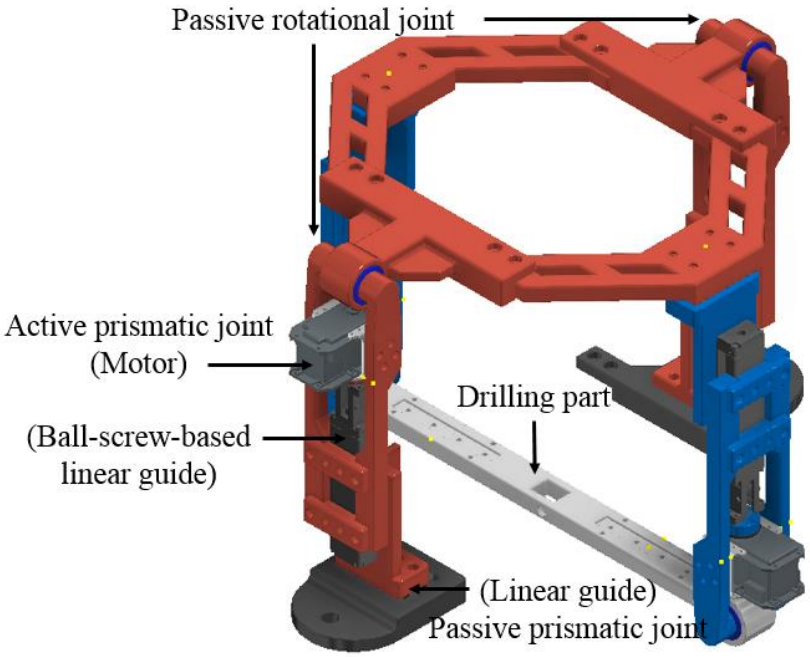

Fig. 9. CAD model of the orientation mechanism.

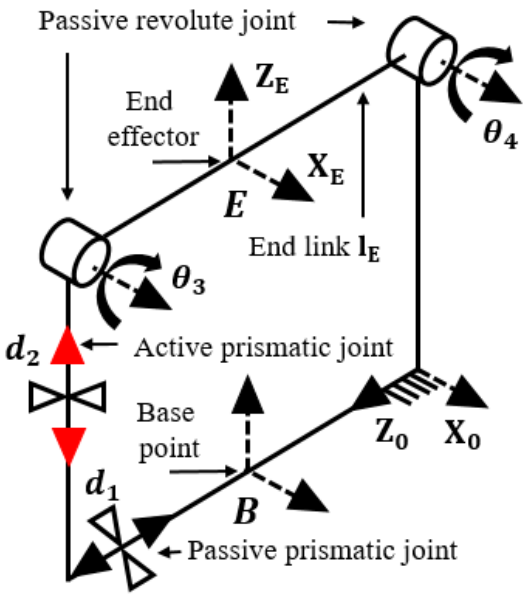

Fig. 10. Kinematic model of the 2P2R four-bar linkage.

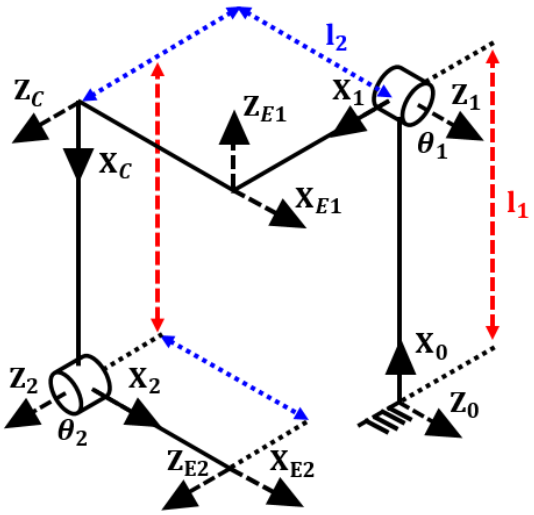

Fig. 11. Kinematic model of the simplified orientation mechanism. The axes are labeled according to the distal D-H convention.

TABLE I

D–H PARAMETERS OF ORIENTATION MECHANISM

Joint i	α_{i-1}	a_{i-1}	d_i	θ_i
1	0	l_1	0	θ_1 = variable + $\frac{\pi}{2}$
E1	$\frac{\pi}{2}$	l_2	0	$\frac{\pi}{2}$
C	$\frac{\pi}{2}$	- l_2	0	$-\frac{\pi}{2}$
2	0	l_1	0	θ_2 = variable + $\frac{\pi}{2}$
E2	0	l_2	0	0

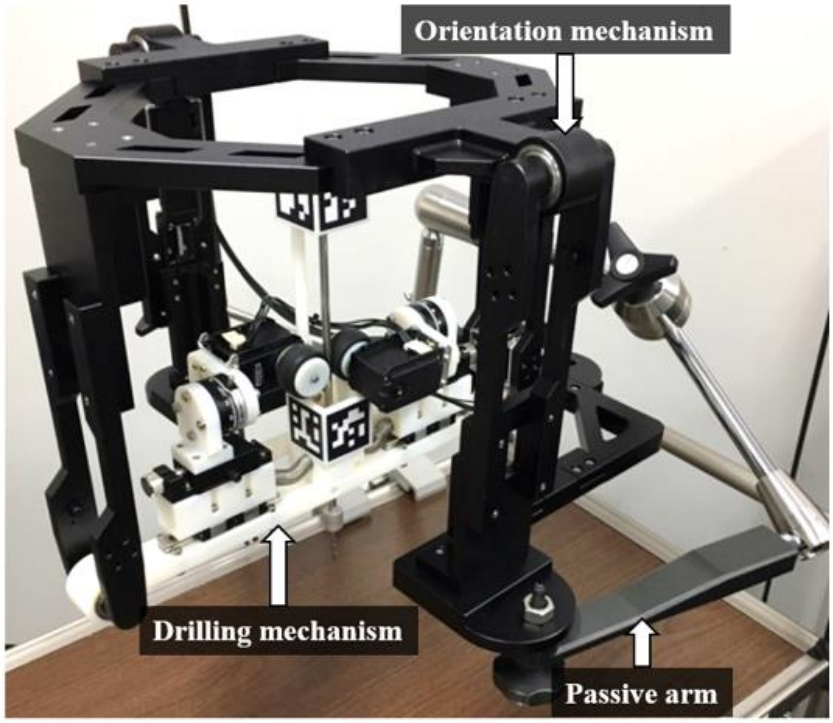

Fig. 12. Configuration of the Robotic system.

2.3 Navigation System

To enable automatic targeting for the proposed robotic drilling system, a CT-guided navigation system using an optical tracker was developed. The system is composed of a stereo camera and three reference markers: one reference marker is used to estimate the pose of the patient, and two reference markers are used to compute the orientation and depth of the drill tip. We obtained the position and orientation of each reference marker in 3D space using a calibrated stereo camera (ZED, Stereolabs Inc., San Francisco, USA), as indicated in Fig. 13. Each pose of the reference marker can be described by a 4 × 4 homogeneous transformation matrix in the camera coordinate frame. The resolution of the optical tracking system (OTS) is approximately 0.7 mm. The navigation system is intended to align the drill with the target point, and to insert the drill tip into the target as planned using CT images.

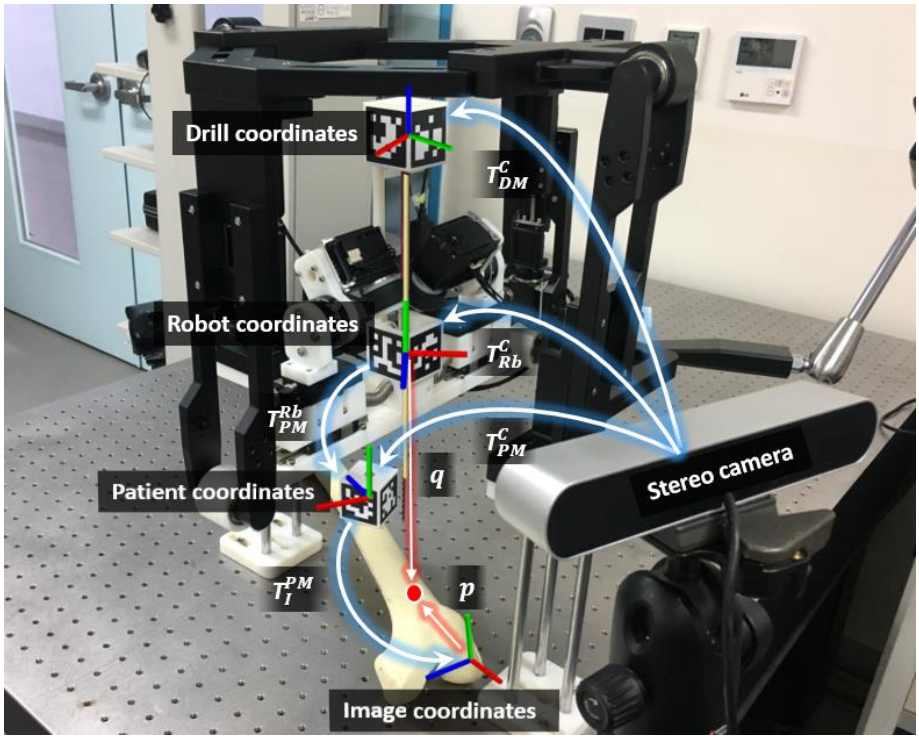

Fig. 13. Configuration of the navigation system.

2.3.1 Robot and Drill Calibration

Each reference marker in this system has a regular cubic structure, with side lengths of 45 mm, and the basis coordinate frame of each marker is located at the center of the cube. Each marker has a different pattern on each side, and its position and orientation are obtained using the stereo vision technique. The robot reference marker is attached to the linear bush, thereby aligning the y-axis of the reference maker with the drill axis. No extra calibration is required between the robot and reference marker coordinates to obtain the drill orientation. The drill tip orientation is determined using the robot reference marker. The drill reference marker is attached to the top of the pipe. To acquire the position of the drill tip attached to the bottom of the pipe, pivot calibration is performed for the pipe connected to the drill [33]. Using these two markers, the drill orientation and position are finally determined based on the camera coordinates.

2.3.2 Frame Matching between the Robot and CT Image

In order to align the drill tip of the robot with the target point in the patient, the robot and patient should both be tracked. A reference marker is firmly fixed to the bone close to the target, so that it can be tracked using the stereo camera [27, 34]. To obtain a homogeneous matrix representing the relationships between the reference coordinates of the patient and those in the preoperative CT image T_I^{PM}, patient-to-image registration is required. In this registration process, at least three fiducial markers that can be detected in the CT image are necessary. In this study, four screws were inserted into the bone to serve as fiducial markers. Finally, a homogeneous transformation matrix from the robot coordinates to the image coordinates T_I^{Rb} is calculated using the following equation:

$$\mathrm{T}_I^{Rb} = (\mathrm{T}_{Rb}^{C})^{-1}\mathrm{T}_{PM}^{C}\mathrm{T}_I^{PM}, \tag{7}$$

where T_{Rb}^{C} and T_{PM}^{C} are the matrices representing the relationships between the camera coordinates and the robot and patient coordinates, respectively.

2.3.3 Navigation Algorithm

The proposed navigation algorithm for performing automatic drilling consists of two main steps: drill angle alignment and drilling to the target depth. First, to align the drill with the target, the y-axis of the robot coordinate system, which has same orientation as the drill axis, should be aligned with the target. For convenience, a vector q from the robot coordinates to the target is defined as follows, as shown in Fig. 13:

$$\mathbf{q} = \mathrm{T}_I^{Rb}\mathbf{p}, \tag{8}$$

where T_I^{Rb} is the homogeneous transformation matrix from the robot coordinates to the image coordinates, and $\mathbf{p}$ is a vector from the image coordinates to the target. To align the y-axis of the robot coordinate system to q, the x- and z-axes of the robot coordinate system should be rotated by θ_1 and θ_2, respectively, which are defined as follows and indicated in Fig. 14:

$$\theta_1 = \frac{\pi}{2} - \tan^{-1}\left(\frac{|q_y|}{|q_z|}\right), \tag{9}$$

and

$$\theta_2 = \frac{\pi}{2} - \tan^{-1}\left(\frac{|\mathbf{q} \times \mathbf{q}_{xz}|}{|\mathbf{q} \cdot \mathbf{q}_{xz}|}\right), \tag{10}$$

where $\mathbf{q}$ and $\mathbf{q}_{xz}$ are (q_x, q_y, q_z) and $(q_x, 0, q_z)$, respectively. The visual feedback provided by the stereo camera makes it possible to control the automatic drilling in real time. The navigation system processes these angular calculations and visual feedback at 15 Hz.

Following the alignment of the drill axis with the target, drilling is performed to the target depth. The drill tip position is obtained using the reference marker on the pipe. The distance from the drill tip to the target point is calculated by considering the relationship between the coordinates of the drill and CT

image. In preparation for a situation in which the drilling angle is not perfectly aligned with the target and a distance of zero cannot be achieved, the drilling system was programmed to stop as soon as the distance reaches a minimum value and begins to increase.

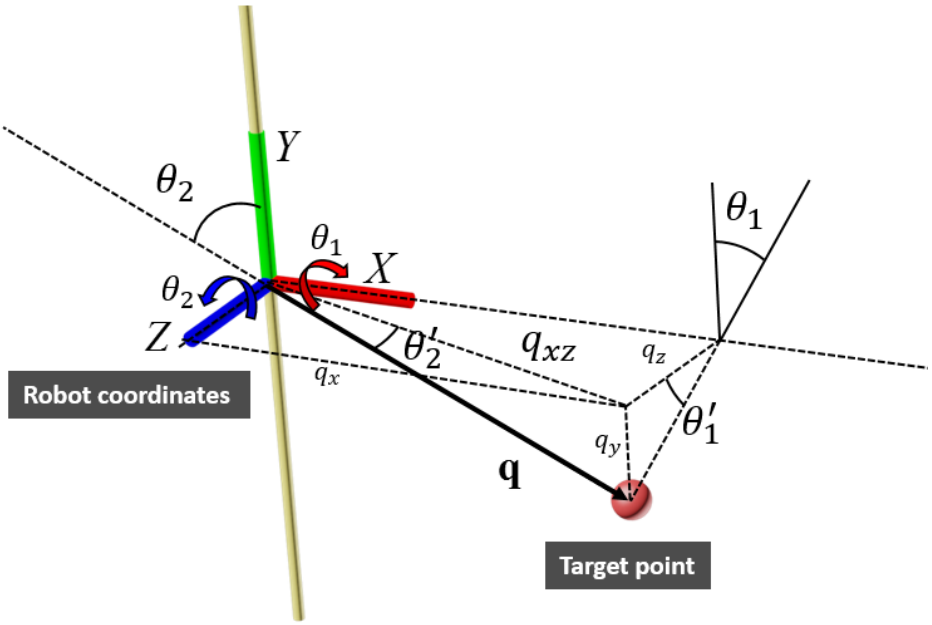

Fig. 14. Relationship between the robot coordinates and the target point.

2.4 Experimental and Results

We conducted a series of basic experiments to evaluate the proposed drilling mechanism, orientation mechanism, and navigation system. We also validated our system by performing ex-vivo tests on swine femurs.

2.4.1 Drilling Mechanism

The proposed drilling mechanism was designed to generate a drilling motion using angled rolling friction. To produce a drilling motion at the drill tip, the rotational and thrust forces should be transmitted through the pipe. To verify the drilling performance achieved by rolling friction, the rotational force and thrust force produced by the rolling mechanism were measured.

To demonstrate that the rotational and thrust forces change with the roller angles, the theoretical values of these quantities, as calculated using the equation (2) and (3), were compared with the measured values. A torque sensor (TRD-50KC, CAS Corp., Yangju, Korea) and load cell (UU-100K, CAS Corp., Yangju, Korea) were used to measure the rotational and thrust forces, respectively. Fig. 15 depicts the experimental setup employed to measure the rotational and thrust forces. We designed a jig to connect the load cell to the torque sensor, so that the torque sensor was assembled with the load cell. The torque sensor and load cell were connected to the pipe on which the rolling friction force was exerted. Using this experimental setup, the rotational and thrust forces produced by the drilling mechanism were measured, and the drilling force was displayed by a digital indicator.

In order to calculate the theoretical rolling friction force using (1), it was necessary to obtain the normal force and coefficient of friction between the rollers and pipe. We assumed that the coefficient of friction was constant because each roller was replaced before its surface became degraded. Because it was difficult to exactly determine the coefficient of friction, we measured the rolling friction force when the roller angle was 0°. By substituting the obtained rolling friction force into (2) and (3), we calculated the

theoretical rotational and thrust forces at each angle. To compare the actual and theoretical forces of the drilling motion, we measured the rotational and thrust forces while the roller angles were positioned in 15° increments. Ten measurements were performed at each angle, using different normal forces. The mean percent error between the theoretical and measured forces was determined to be 6.95%, and Table II presents one set of results. The experimental results indicated that the drilling mechanism could generate a drilling motion with predictable rotational and thrust forces.

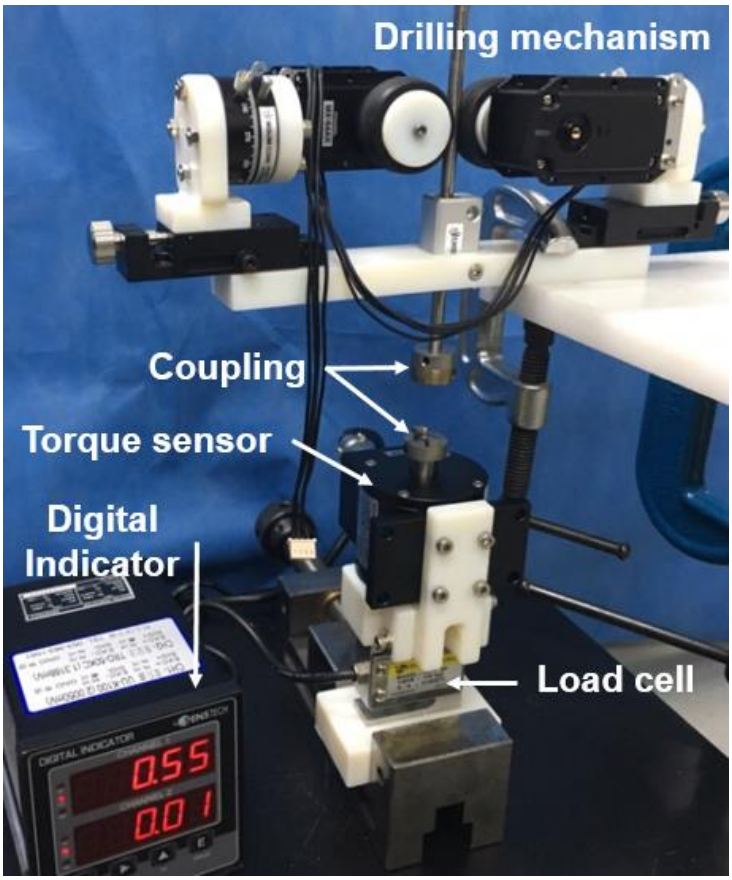

Fig. 15. Experimental setup used to measure the rotational and thrust forces.

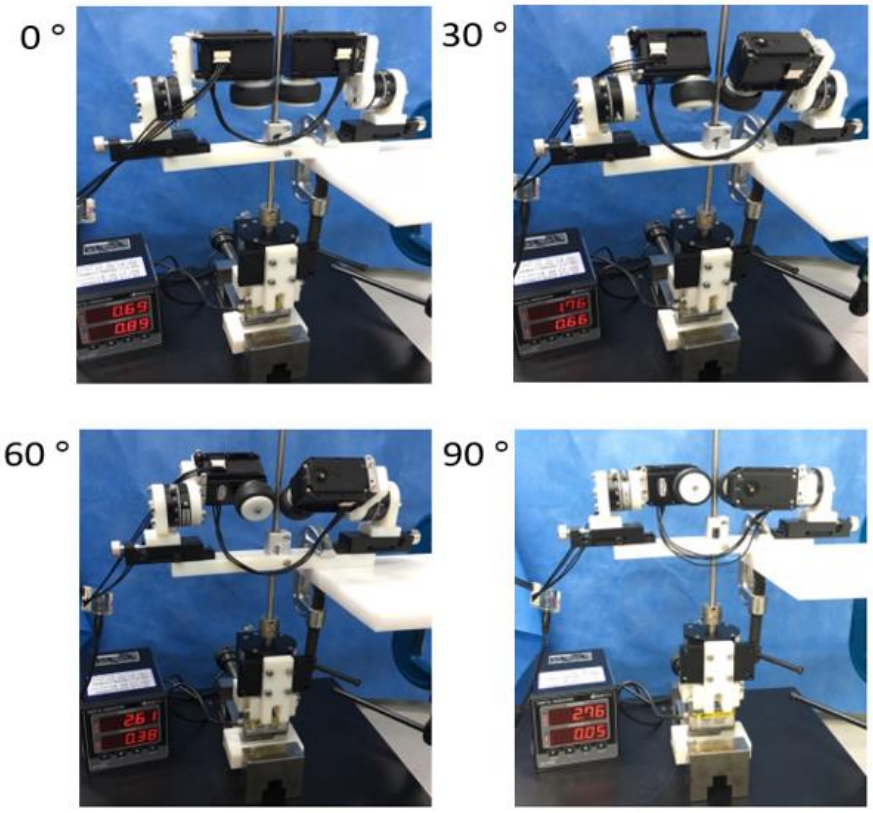

Fig. 16. Evaluation of the drilling mechanism.

TABLE II

COMPARISON OF THE MEASURED AND THEORETICAL FORCES

Angle (°)	F_r (N)		F_t (N)	
	Actual	Theory	Actual	Theory
0	0.00	0.00	16.46	16.46
15	3.63	4.21	15.29	15.88
30	7.84	8.23	13.72	14.21
45	11.76	11.66	12.15	11.66
60	15.68	14.21	9.41	8.23
75	18.91	15.88	5.88	4.21

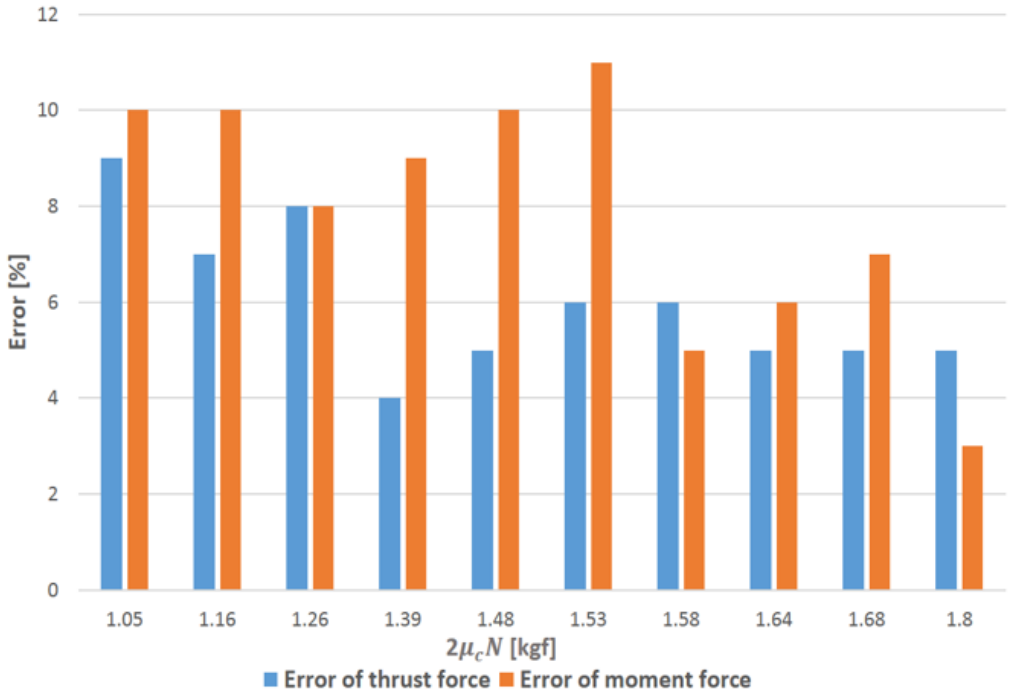

Fig. 17. Error between measured and theoretical values.

2.4.2 Orientation Mechanism

To evaluate the precision and repeatability of the orientation mechanism with the navigation system, we conducted a phantom experiment. The test consisted of the following four steps. First, a piece of paper with printed target points was pasted onto the reference marker. Second, the orientation mechanism was operated using the navigation system to guide the drill tip to the target point. Once the alignment was completed, the drill tip was inserted and penetrated the paper target. Finally, the errors between the designated and penetrated points were measured.

The experimental setup was almost the same as that depicted in Fig. 13. However, to obtain the target point with minimal calculations, we directly used the reference marker as the target. Thus, no matrix

transformation from the image coordinates to the target was necessary, thereby reducing the registration error. Because the reference marker was cubic, we attached a square-shaped paper target to the top of the marker. The paper target had four points, which formed a square with side lengths of 22.50 mm. We placed the marker under the robot in arbitrary positions, and conducted 10 targeting tasks using the orientation mechanism with a vision-guided navigation system. The four points on the paper target were penetrated at each position (see Fig. 19(a)). Points where two lines intersected orthogonally, which were surrounded by two rectangles, were designated as the target points, as shown in Fig. 19. To determine the error between the designated and penetrated points, we used an Artec Spider 3D scanner and Artec Studio 9 software (Artec Europe Corp., Luxembourg, Germany), which has an accuracy of 0.03 mm. A 0.1 mm diameter drill tip was employed to enable precise error measurements.

The mean in-plane distance between the target and penetrated point was determined to be 0.68 mm, with a standard deviation of 0.37 mm and a maximum deviation of 1.61 mm. However, these values included the errors resulting from the incorrect attachment of the paper target to the reference marker. To eliminate this additional error, we drew a rectangle using the four penetrated points, and compared the side lengths with the desired side length of 22.50 mm. The side lengths are listed in Table III, and Fig. 19(b) shows one of the results obtained using the 3D scanner and software. The mean in-plane side length error of the repeated pointing tests was 0.47 mm, with a standard deviation of 0.35 mm. In addition, the repeatability performance of the orientation mechanism was evaluated by the coefficient of variation (CV) [35, 36]. Because the mean distance between penetrated points was approximately 22.52 mm, and the standard deviation was 0.35 mm, the CV was approximately 1.55%, which included the navigation error, as well as the mechanical error of the proposed system.

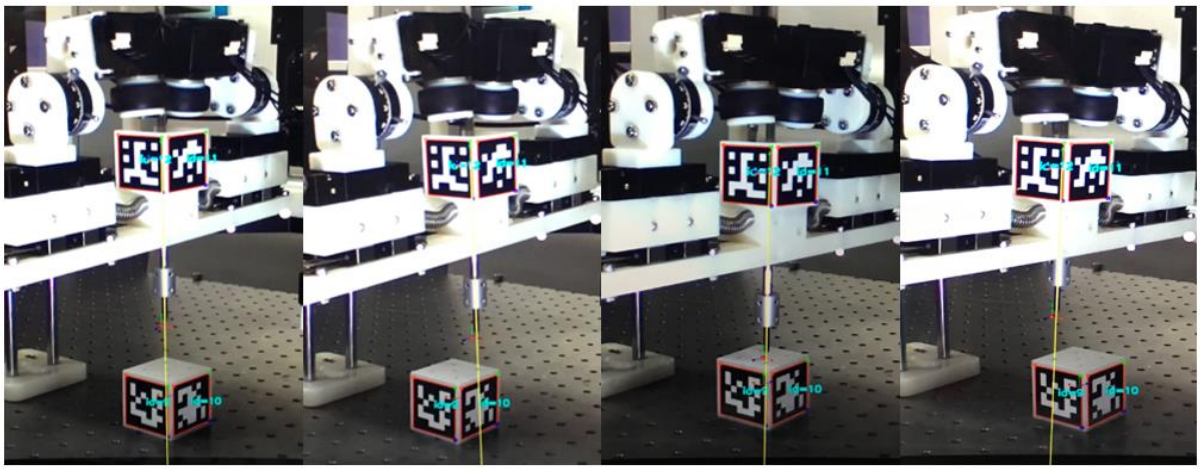

Fig. 18. Pointing test using the proposed navigation and robotic system.

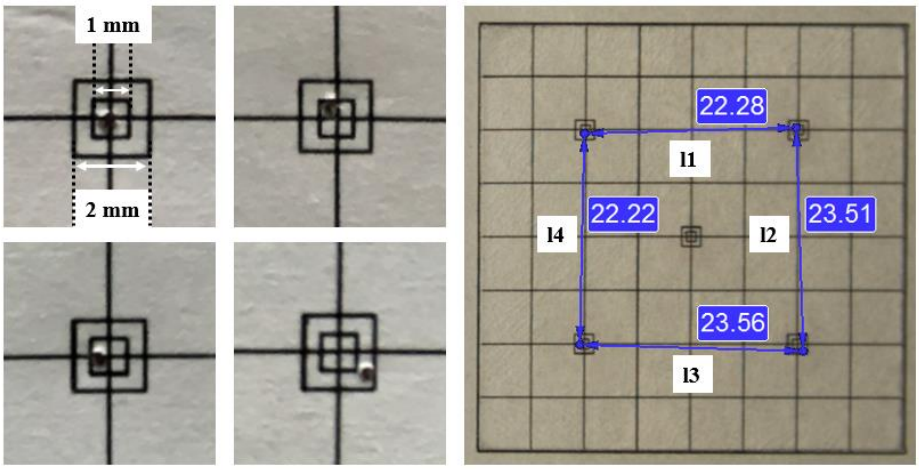

Fig. 19. Pointing results. (a) Close-up of the target and (b) distances between the desired and penetrated points.

TABLE III

POINTING ERROR

Side number	l_1(mm)	l_2(mm)	$l_{\backslash 3}$(mm)	l_4(mm)
1	22.282	23.508	23.557	22.224
2	21.133	22.602	21.788	22.816
3	22.047	22.983	22.479	23.168
4	23.004	23.510	21.923	23.248
5	22.752	22.379	22.560	22.438
6	22.498	22.845	21.935	22.816
7	23.467	22.088	22.483	23.004
8	20.930	22.007	22.747	23.147
9	22.183	22.508	22.924	22.449
10	21.999	22.002	22.058	22.164

2.4.3 Ex-Vivo Drilling Test

The feasibility of the proposed system was investigated by performing an ex-vivo drilling test on a swine femur. Drilling procedures are required for bone biopsies to diagnose bone tumors or marrow. Because swine bones closely resemble human bones in terms of the density and fracture stress [37, 38], we selected a swine femur for ex-vivo testing. As the structures and properties of non-dry and living bone tissues do not differ significantly, samples from a bone kept in cold storage were used [39, 40].

Because the target lesion of the bone biopsy was located in the bone marrow, we designated a point close to the middle of the bone marrow as the target point using 3D Slicer (www.slicer.org), which is an open-source software package for visualizing and analyzing medical image data, with a preoperative CT image. Four screws were inserted into the swine femur to serve as fiducial markers. These fiducial markers were employed for two types of registration: patient-to-image registration to match the coordinates in the real-time visual image to those in the postoperative CT image of the bone, and image-to-image registration

to determine the errors between the designated targets in the preoperative CT image and the drilled holes in the postoperative CT image. To enable a clear identification of the drilled points in the final CT image, the bone marrow was pulled out and medical cement was inserted.

In actual surgeries, screws should not be used as fiducial markers, to reduce the damage to the normal tissue. However, in this experiment, four screws were utilized as the fiducial markers, in order to minimize the fiducial registration error (FRE), which affects the target registration error (TRE) [41]. In addition, the robot was fixed to a vibration-free table during the experiments. To minimize the errors caused by the vibrations of the passive arms, two fixed jigs were employed, as shown in Fig. 20.

Fig. 20 depicts the experimental setup of the ex-vivo drilling test, and the workflow is summarized in Fig. 21. First, we took preoperative CT images of the prepared swine femur with the cement and fiducial markers. On the CT image, we marked a point on each fiducial marker for patient-to-image registration and a target lesion using 3D Slicer. After fixing a reference marker to the swine femur, we conducted patient-to-image registration by matching the fiducial markers on the actual bone to those in the CT image. Using a calibrated probe with a stereo camera, we matched the screws on the swine femur to each screw on the preoperative CT image. Through this registration, the position of the target could be obtained on the real-time visual image. Using the patient and robot reference markers, the navigation-guided robotic system aligned the drill axis with the target, and drilled to the target depth. Finally, to measure the accuracy, we obtained postoperative CT images and compared them to the preoperative CT images, as shown in Fig. 23. For this comparison, image-to-image registration was performed using the fiducial markers that were used for the previous patient-to-image registration. The end of the drilled point was identified in the postoperative CT image, and the distance between the identified point and target point was calculated using 3D Slicer.

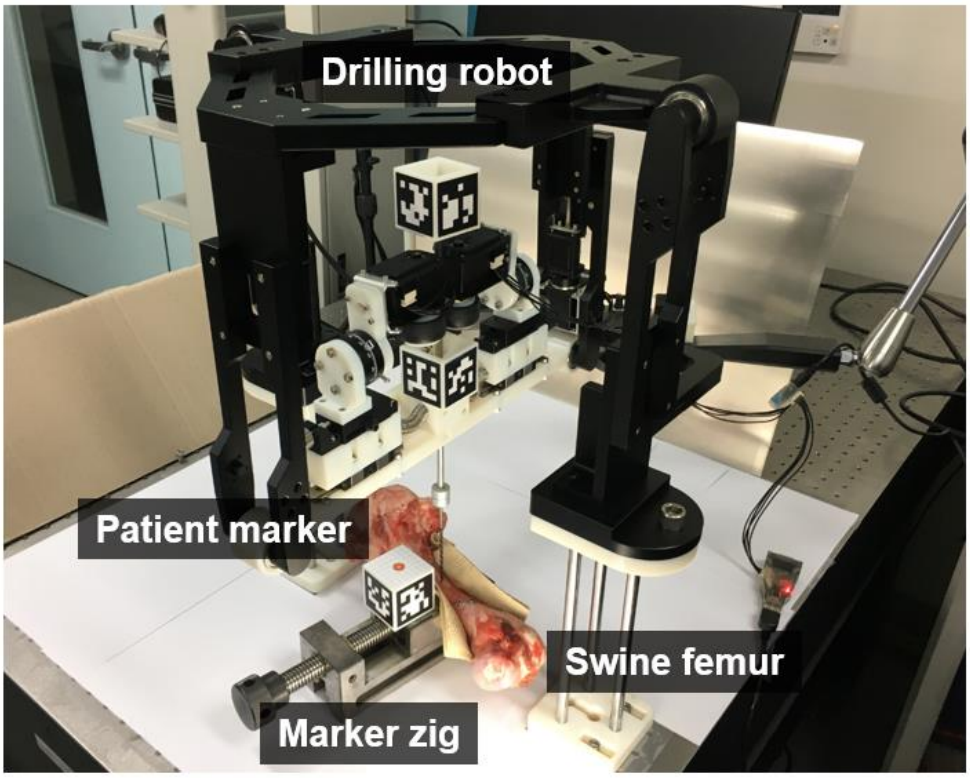

Fig. 20. Experimental setup used for the ex-vivo swine femur test.

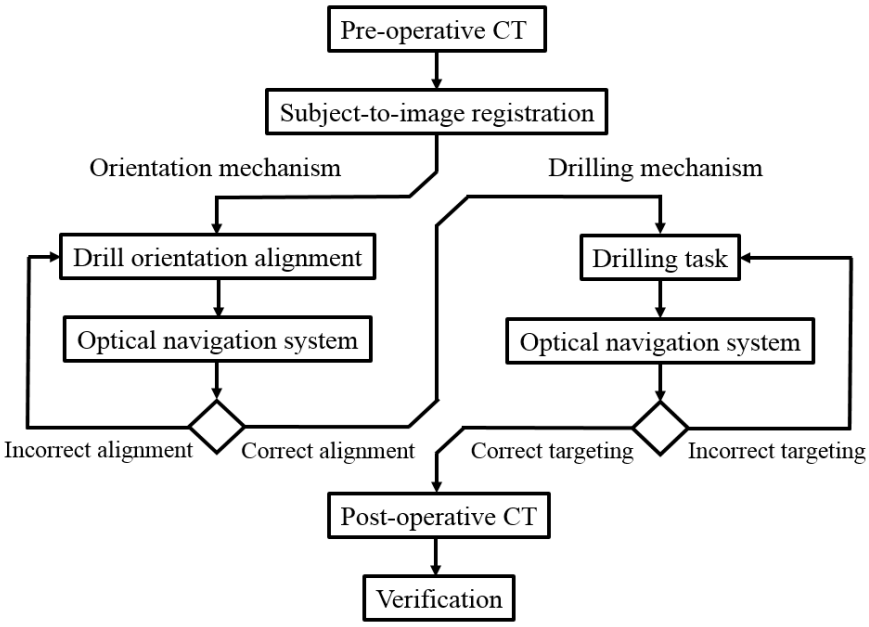

Fig. 21. Workflow of the navigation-guided drilling test.

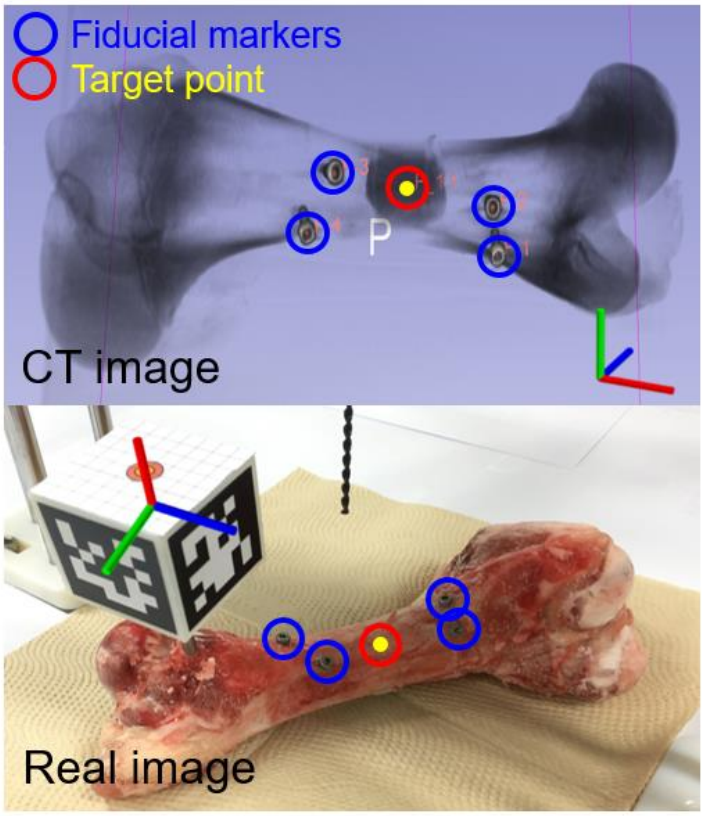

Fig. 22. Patient to image registration.

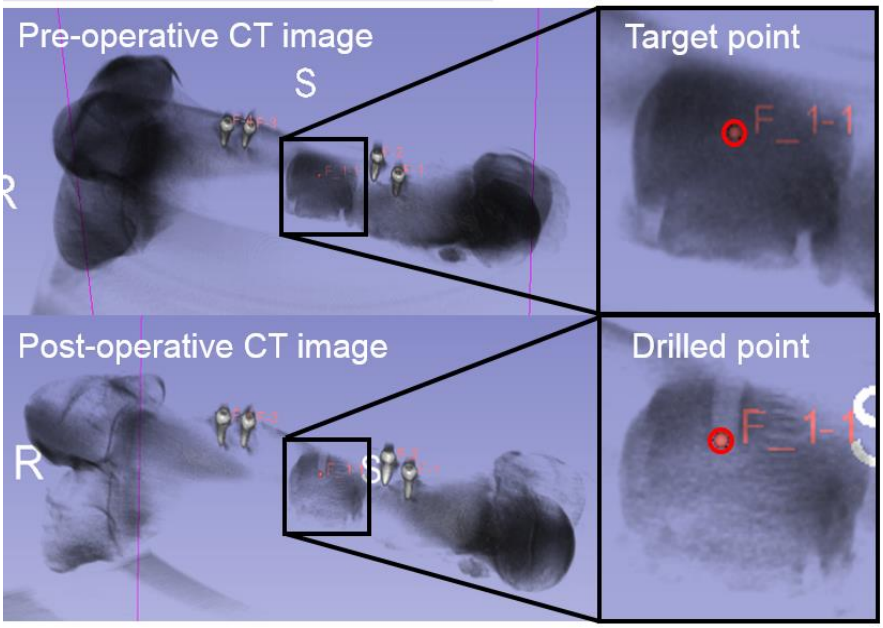

Fig. 23. Pre- and postoperative CT images.

TABLE Ⅳ

FRE AND TARGETING ERROR OF THE DRILLING TEST

	FRE (mm)	Targeting Error (mm)
1	0.399	2.76
2	0.485	2.62
3	0.657	2.15
4	0.279	1.94
5	0.418	1.75
6	0.267	2.59
7	0.385	1.39
8	0.363	2.35
9	0.618	2.63
10	0.164	2.79
Avg.	0.404	2.30

2.5 Discussion

The rolling friction mechanism made it possible to remove the drill tip safely from the robot in an emergency. In addition, the mechanism does not require a linear actuator to perform a linear drilling motion, which allows the structure to be compact in the drilling direction. However, some errors were observed between the theoretical and measured drilling forces. When the normal force exerted by the roller on the pipe was too small, slips could occur, and the drilling force became smaller than the theoretical value. When the normal force was sufficient, i.e., greater than the 1.58 kgf friction force observed in this study, the theoretical and measured forces had a difference of less than 7%. Another source of error was the variation of the coefficient of friction. Unlike rigid body friction, the rolling friction of rubber varies in proportion to the contact area. Because the surface of the rubber roller used in this study had a convex shape rather than flat, the contact area varied according to the roller angle, and the rolling friction changed. In addition, because the contact area varied with the normal force applied to the roller, it was difficult to accurately calculate the friction. Nevertheless, we confirmed that the final force at the drill tip was sufficient to perform bone drilling. In addition, the rubber roller is to be used as a disposable component to ensure the constant coefficient of friction and to avoid the risk of infection. In this study, the changes in the rotational and thrust forces resulting from the roller angle were studied, and the rolling-friction-based drilling mechanism was demonstrated to generate both rotational and thrust forces for drilling motion. In the future, a torque sensor can be installed between the motor and the roller to obtain the actual rolling friction force. Using this sensor, a slip of the rotating pipe can also be detected, which will improve the safety of the rolling friction mechanism for clinical use. Furthermore, we have will apply a mechanism for setting the angle of the roller to become perfectly line-symmetrical and prevent the power loss and lippage between the roller and the pipe.

The release mechanism was designed to facilitate the rapid separation of the rollers from the instrument, and the operator can simply pull the release pin to achieve this separation. On the other hand, the following procedure is required to resume the operation. First, the operator rotates the handle of the x-axis unit to move the roller in the opposite direction to the pipe (see Fig. 3). Second, the operator pushes the motor parts on the linear guide in the direction of the pipe, and the pin connection parts will be in contact

before the rollers contact the pipe (see Fig. 3 and Fig. 4). Third, when the pin connection parts are in contact, the pin holes are automatically aligned, allowing the operator to easily insert the pin. Last, the positioning unit should move toward the pipe again to induce the normal force and generate the rolling friction force between the rollers and the pipe. Although it is not difficult to put the pin back because of the easy alignment of the two holes, the above procedure may take some time. In this study, however, we assumed that operators would have some time to resume the surgical procedure after the occurrence of such an emergency, and focused on the rapid removal in the case of an emergency. Since strong normal force makes it difficult to remove the release pin, a linear bush will be applied to minimize the friction on the pin in the future.

The proposed 2P2R four-bar linkage, with a ball-screw-based linear actuator, was applied in the orientation mechanism. Although the range of orientations achievable using this mechanism is not as wide as that of the previous orientation mechanism, the proposed mechanism has a high accuracy, and is robust against external forces. Furthermore, the range of orientations could be increased by increasing the displacement of the linear actuator or decreasing the length of the end link, according to (5). Because the resolution of the orientation mechanism is much higher than that of the measuring system (OTS), we only specified the mechanical resolution and conducted the accuracy and repeatability test which included navigation error.

Because the proposed orientation mechanism has two DOFs, the drilling system can only perform guiding to the target point: it does not consider the entry point. During a bone biopsy, the entry range is relatively wider than the target lesion. Therefore, we chose to use two DOFs for guiding the drill to the target point to reduce the complexity of the system. To perform gross positioning for the entry point, a six-DOF passive arm was employed, as in the insertion system described in [42]. Because the navigation system provides the information of the related position between end effector and the entry point in real time, surgeons can place the robot up to the entry point without much offset. Although gross positioning should be conducted manually, the fine positioning and drilling tasks, which are the most important and difficult tasks during surgery, can be performed by the proposed robotic system. In addition, the proposed orientation mechanism is not a remote center of motion (RCM) mechanism. Therefore, it is difficult to calculate the position of the drill tip when changing the orientation. However, because the drilling is conducted after fixing the orientation, it is not necessary to know the position of the drill tip during the operation of the orientation

mechanism.

In the vision-guided navigation system, a stereo camera and three reference markers are used to obtain the reference coordinates of the patient, robot, and drill. Because the orientation of the robot coordinates is the same as that of the drill coordinates, the drill tip orientation and position can be obtained using only one reference marker on the drill. However, the reference marker on the drill should be located at the top of the long pipe. The pipe could be bent or oscillate during drilling, resulting in an orientation error. If the drilling depth is large, then even a small orientation error can cause a significant targeting error. To minimize this error, separate reference markers were used on the robot and drill.

It is arguably difficult to compare the results of this study with those of existing studies using other drilling robots because the systems in these published studies were evaluated using different experimental conditions, including the OTS, target stiffness, depth of the target lesion, and drill tip. The ex-vivo drilling test on the swine femur yielded an average targeting error of 2.30 mm in this study. Because the mean lesion size in 186 bone biopsy cases was found to be 31 mm, ranging from 6 mm to 98 mm [43], the targeting error which was approximately 7% of the mean lesion size is acceptable for bone biopsies. This error includes the errors introduced by both the navigation and mechanical systems. The navigation error was attributed to errors in the patient-to-image registration, image-to-image registration, camera calibration, pivot calibration, and visual feedback delay, among other factors. In particular, when the patient-to-image and image-to-image registrations were conducted, each registration resulted in an FRE of approximately 0.4 mm. In the mechanical system, some slips and bending of the drill occurred upon the initial contact between the drill and the bone, resulting in a misalignment between the drill and the target, which produced a certain amount of error.

A problem related to the soft tissue should be considered before using the proposed drilling system for clinical applications. When a drilling task is conducted without any protective guide, the rotating drill damages soft tissues, including the skin, muscles, nerves, and blood vessels. To minimize such damage, a soft tissue protection guide or sleeve that provides a barrier between the soft tissue and instrument is necessary. In addition, sterilization methods should be considered for clinical applications. We have a plan to use a sterile cover for the entire robot except for the linear bush through which the pipe passes. In addition, the

drilling mechanism should be modified to make the linear bush detachable for sterilization. The pipe will be sterilized for reuse, and the drill tips, which have direct contact with the patient, will be disposable. Furthermore, to verify the feasibility of the proposed drilling system for real surgery, an in-vivo bone biopsy test using swine or cadaver bone will be conducted in the future.

2.6 Conclusion

We have presented a prototype of a navigation-guided auto-drilling system. This drilling system was the first successful trial based on rolling friction. The drilling mechanism can generate both rotational and insertion motions using angled rolling friction. The rolling friction mechanism has the advantages of facilitating drill tip detachment in emergency situations and enabling the robot to have a compact structure. Furthermore, the proposed four-bar linkage with a ball-screw-based linear actuator ensures the robustness and high resolution of the orientation mechanism. The integration of the robotic system with a vision-guided navigation system enables the automatic alignment of the robot with the target, and the insertion of the drill tip into the target.

An ex-vivo drilling test performed on 10 swine femur samples verified the effectiveness of the proposed robotic drilling system. The experiments confirmed that the rolling-friction-based drilling mechanism could be used to drill into bone tissue, and that the ball-screw-based orientation mechanism could yield a high accuracy. The robotic system achieved an acceptable targeting error of 2.30 mm, which was approximately 7% of the average target size.

III. REMOTE CENTER OF MOTION BASED GUIDING MECHANISM

3.1 Introduction of Guiding Mechanism

To enable the surgeon and robotic system to collaborate efficiently, it is necessary to divide the surgical tasks for the surgeon and robot. Guiding and maintaining the orientation of the drill, which is the most difficult task in the whole drilling process, should be conducted by the robot. Conversely, positioning the drill tip near the entry point and inserting the drill, which are relatively easy tasks, can be performed by the surgeon manually. To satisfy these conditions, a remote center of motion (RCM) mechanism is a prominent candidate for an assistive drilling mechanism. When the surgeon locates the drill tip around the entry point, the RCM mechanism can guide the orientation of the drill toward the target point while maintaining the entry point.

Although various types of RCM mechanisms have been developed, such as the circular guided arc type [44]-[47], parallelogram type [48]-[50], belt type [51], spherical linkage type [52], and others [53][54], they are not suitable for the purpose of bone drilling. To the best of our knowledge, recent studies have not investigated assistive robots for bone drilling using an RCM mechanism. Because the original motivation for the RCM mechanism was for laparoscopic surgery or needle insertion into soft tissue [55][56], it was not necessary to provide a high rigidity against external force. For the circular guided arc type, the actuator has to move along the arc link, or the circular arc itself has to move, to have a remote center of motion. These actions may reduce the stability and reliability of the system. In addition, the high precision required in manufacture and assembly limits the use of circular prismatic joints [57]. The parallelogram type also has drawbacks; because it requires a number of revolute joints and linkages, a large inertial moment is inevitable, leading to a lack of absolute rigidity [57].

Because a large external force is applied to the orientation mechanism during the drilling process, the RCM mechanism for bone drilling needs to have high rigidity. Otherwise, the RCM mechanism cannot

withstand the drilling force, and the orientation of the drill may deviate from the target point. The RCM mechanism should also have high resolution because the orientation cannot be modified after starting to drill, unlike needle insertion into soft tissue. Depending on the drilling depth, the targeting error can be large, even when the orientation error of the drilling is small. Various efforts have been made to improve the rigidity of the RCM mechanism. For example, Yip et al. [58] developed a RCM mechanism using a linear actuator. However, the RCM mechanism consists of one linear actuator and three passive joints, namely, circular prismatic, linear prismatic, and revolute joint. When the orientation is controlled, the linear motion of the linear actuator should be transferred to curved motion through the passive circular prismatic joint. In this process, power loss is inevitable; thus, this mechanism is not suitable for withstanding a large drilling force. In the RCM mechanism developed by Kim et al. [59], the orientation can be controlled using only linear actuators. As the ratios of their displacements are equal to the ratios of the distances between them and a point, the mechanism can make a remote center of motion. However, their RCM mechanism has one degree of freedom (DOF), and the mechanism has a parasitical movement along the end-effector axis [57]. When the tilting motion is generated in the mechanism, an unintentional linear motion necessarily occurs along the end-effector axis. Therefore, it is classified as a non-mechanical RCM type [55].

In this section, we propose a 2-DOF RCM mechanism based on a trigonometric ratio for bone drilling. The proposed mechanism is a new mechanical RCM mechanism type that employs type synthesis between the linear-actuated and arc-guided types. The proposed mechanism is not only highly rigid and has high resolution, but it also maintains the RCM point mechanically. Further, it has an integrated vision-guided navigation system for ascertaining the positional relationship between the robot and patient without fixing the robot to the patient and automatically manipulating the mechanism to the target. To verify the feasibility of the proposed mechanism and system, a prototype was built and experiments were conducted.

3.2 Design of the Proposed RCM Mechanism

A remote center of motion mechanism using a trigonometric ratio was developed to align the orientation to the target.

3.2.1 Design Consideration

To design an assistive RCM mechanism for bone drilling, the surgical procedure using the assistive robotic system has to be considered. The robotic bone drilling procedure consists of four steps:

1. Through CT images, the doctor determines the entry and target entry point, and specifies an optimal drilling path that avoids critical vessels or nerves.

2. The surgeon places the RCM point of the mechanism near the entry point of the drilling and fixes the RCM mechanism using a passive arm.

3. Through a vision-guided navigation system, the RCM mechanism aligns the orientation of the drill to the target.

4. The drilling task is performed manually, while the orientation is maintained by the RCM mechanism.

Up to step 3, a guiding rod, with accurate length from the arc-guide to the RCM point, is used without a drill tip. The rod physically informs the RCM point and helps to locate the RCM point to the entry point of drilling. In step 4, the guiding rod is removed, and a drill rod in which a drill tip is mounted is inserted into the RCM mechanism.

In the bone drilling procedures, the RCM mechanism needs to guide and maintain the orientation of the drill, which is the most important and most difficult task. To achieve this objective, the RCM mechanism should satisfy the following conditions:

1. To withstand the drilling force, the RCM mechanism should have high rigidity for tilting rotation.

2. To conduct the drilling precisely, the RCM mechanism should have a high resolution.

3. To position the RCM mechanism using a passive arm, the mechanism should have a compact structure.

During the bone drilling process, a large external force is applied to the drill. Wolf et al. [60] conducted clinical experiments and found that the bone drilling robotic structure should be capable of withstanding a load of 10 N, which is the force typically exerted by a surgeon during operation. In particular, the force applied toward the tilting direction, which is the y-axis in this paper, is much larger than that applied toward the x-axis, and the maximum applied force on the y-axis is approximately 17.3 N during bone drilling. Because the external force on the y-axis is large, the rigidity of the tilting mechanism, which is for yaw rotation, should be high to enhance the stability of the drilling mechanism. In addition, because the orientation of the drill cannot be modified during the bone drilling process, the orientation should be precisely aligned in the first trial. Therefore, the resolution of the RCM mechanism should be high. Finally, considering that the position of the RCM mechanism is manually adjusted and the surgical site is confined, the RCM mechanism should have a compact structure.

3.2.2 Structure and Workspace of the RCM Mechanism

Considering all of the above design considerations, we designed a trigonometric ratio-based RCM mechanism (T-RCM) to aid the bone drilling process, as shown in Fig. 24. The T-RCM has two DOFs, for yaw and roll rotation. To withstand the large drilling force exerted on the y-axis, a pair of linear actuators is applied based on the trigonometric ratio. This yaw-rotational RCM mechanism was designed by making the ratio of the height from the RCM point to each linear actuator equal to the feed rate of each linear actuator, as shown in Fig. 25. We determined that the height and feed ratios of the top and bottom are all 3:2. The two linear guides (LX1502C-B1-N-125, LX1502C-B1-N-100, MISUMI Group Inc., Tokyo, Japan) move via one

rotary motor (MX-64R, Robotis Corp., Seoul, Korea) with two set of belt and pulley mechanisms. To achieve a different feed rate, we used a different pulley ratio of 2:3. Two oil-less linear bushes (SMA6GUU, NIPPON BEARING CO. LTD., Niigata, Japan) were attached to the tip of each linear actuator with a revolute joint. Through these two linear bushes, the orientation of the drill is guided while the translational and rotational frictions between the holder and the drill rod are reduced during drilling. In addition, a gearless arc-guide is applied to keep the depth of the insertion axis constant and maintain a position on the RCM point. Two bearings are assembled onto the guiding rod, and it is connected to the top and bottom of the arc-guide.

To obtain a compact structure, the other DOF is designed on the z-axis. The yaw RCM mechanism has a triangular workspace. When one DOF is added on the z-axis to the yaw RCM mechanism, as shown in Fig. 25, the resulting two-DOF RCM mechanism has a cone-shaped workspace. When the additional joint is on the y-axis instead of the z-axis, the linear actuators of the yaw RCM mechanism should cover all of the yaw workspace and therefore have a bulky structure. The workspace of the proposed RCM mechanism is graphically illustrated in Fig. 26. The proposed RCM mechanism provides a partial circular cone workspace with a central angle that range from approximately 6.2° to 32.6°. The range of the yaw angle is determined by the length of the linear guides and value of the trigonometric ratio. Because of the part used for roll rotation, an exclusion space occurs in the cone-shaped workspace. To minimize backlash, anti-backlash gears (NS80AL50B+0810, NS80AL70B+0810, KYOUIKU GEAR MFG CO. LTD, Tokyo, Japan) are applied for roll rotation; these gears are rotated by a rotary motor (MX-64R, Robotis Corp., Seoul, Korea). The base of the RCM mechanism is designed to connect to a passive arm. Most of the parts were machined from aluminum, and the arc-guide was fabricated using a rapid prototyping machine (Eden 250TM, Stratasys Ltd., Eden Prairie, USA). Fig. 27 shows the prototype of the T-RCM, and the size of the mechanism is approximately [250, 150, 240] mm.

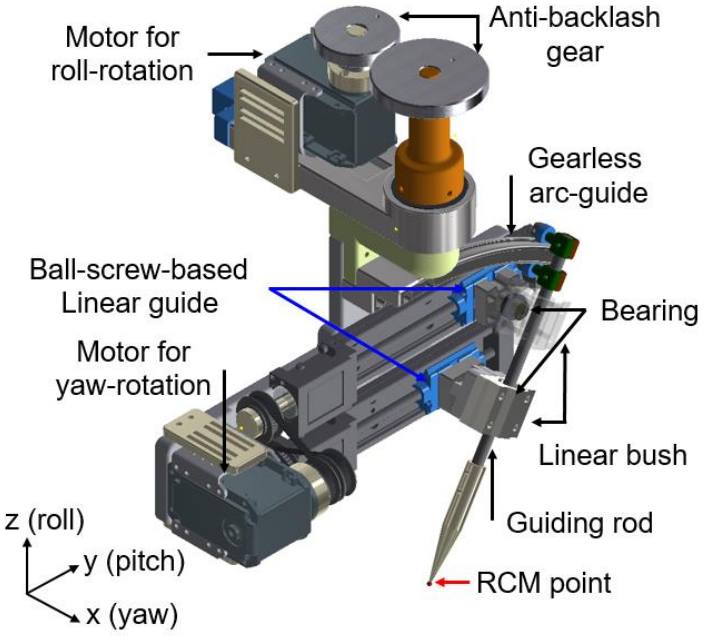

Fig. 24. CAD model of the T-RCM.

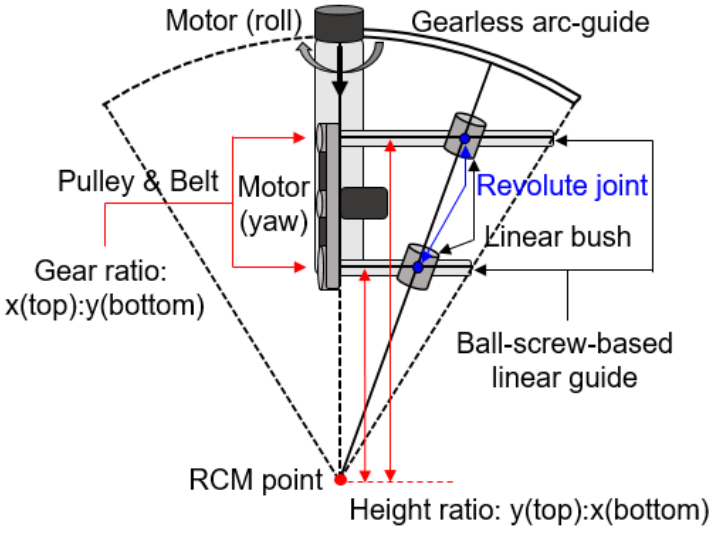

Fig. 25. Kinematic model of the T-RCM.

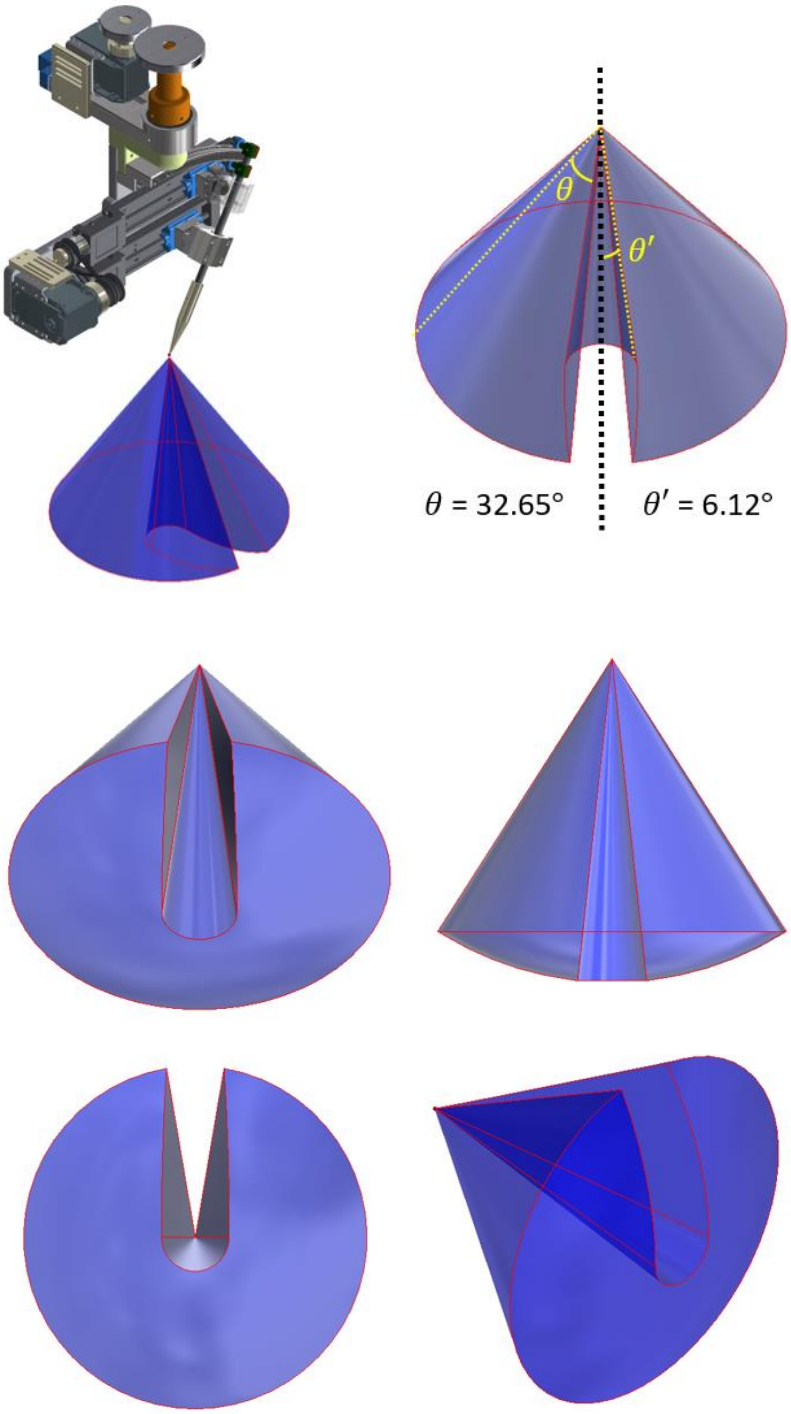

Fig. 26. Workspace of the T-RCM.

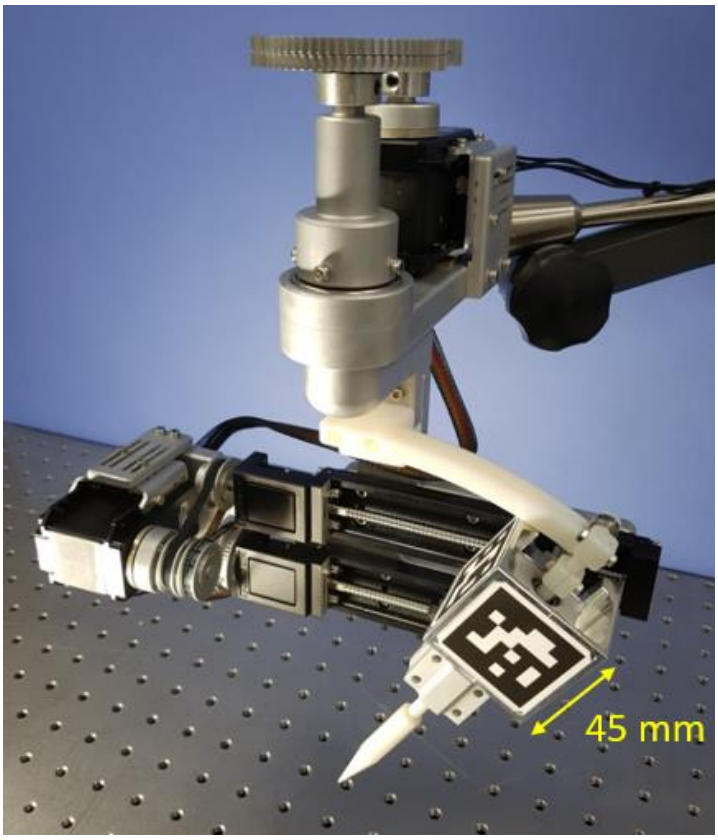

Fig. 27. Prototype of the T-RCM.

3.3 Navigation System

A vision-guided navigation system using an optical tracker was developed to align the orientation of the T-RCM to the target.

3.3.1 System Configuration

The vision-guided navigation system consists of a stereo camera (ZED, Stereolabs Inc., San Francisco, USA) and two reference markers—one for tracking the T-RCM, and the other for tracking the patient (Fig. 28). To alleviate the line-of-sight problem of the optical tracker caused by the roll rotation of the T-RCM, the reference marker has a regular cubic structure, in which each face is painted with a different pattern. The side length of each face is 45 mm, and the basis frame of the marker is located at the center of the cube.

The pose of each reference marker in three-dimensional (3D) space was obtained using the following steps: 1) Take the left and right images from the calibrated stereo camera. 2) Extract the corner points of the two reference markers. 3) Reconstruct the 3D pose using the triangulation method.

To eliminate extra calibration between the T-RCM and the reference marker frame, we mechanically aligned the basis frame of the reference marker to the center line of the linear bush (Fig. 28). From this task, the drilling axis can be regarded as the z-axis of the T-RCM frame.

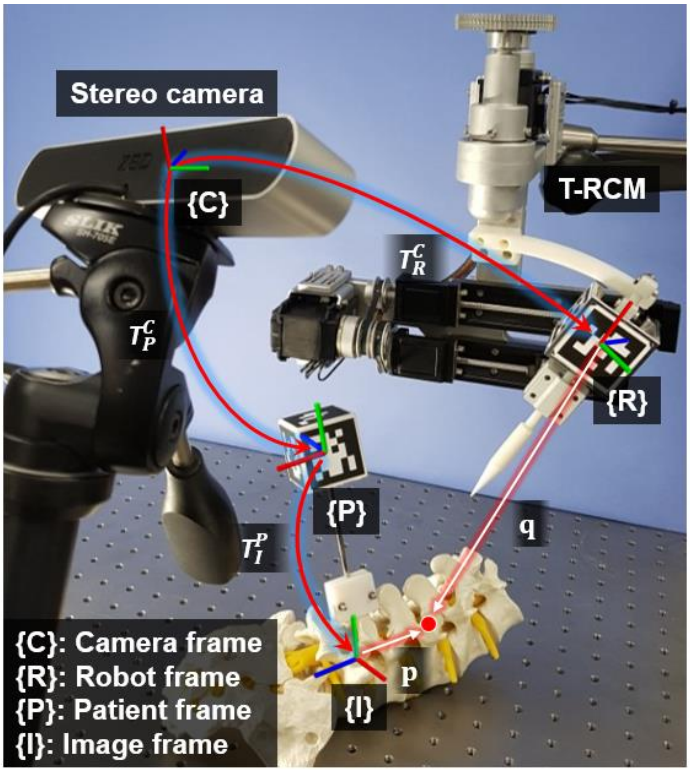

Fig. 28. Configuration of the navigation system.

3.3.2 Frame Matching between the Robot and CT Image

The transformation matrix representing the relationships between the patient and the preoperative CT image, $\mathbf{T}_\mathbf{I}^\mathbf{P}$, are typically calculated using anatomical landmarks, fiducial markers, or template-assisted markers [61]. To simplify the patient-to-image registration process and focus on the assistive bone drilling mechanism, we used the template-assisted marker, which can be tightly positioned on the surface of bone. Because the template-assisted marker was pre-registered to the CT image [61], the target with respect to the CT image can be tracked by the stereo camera after placing the marker on the desired location. At the same time, the orientation of the T-RCM can be obtained by tracking the reference marker on the tip of the mechanism. From these patient and T-RCM reference markers, a transformation matrix from the T-RCM frame to the image frame ($\mathbf{T}_\mathbf{I}^\mathbf{R}$) is calculated using the following equation:

$$\mathbf{T}_{\mathbf{I}}^{\mathbf{R}} = (\mathbf{T}_{\mathbf{R}}^{\mathbf{C}})^{-1}\mathbf{T}_{\mathbf{P}}^{\mathbf{C}}\mathbf{T}_{\mathbf{I}}^{\mathbf{P}}, \tag{11}$$

where $\mathbf{T}_{\mathbf{R}}^{\mathbf{C}}$ and $\mathbf{T}_{\mathbf{P}}^{\mathbf{C}}$ are the transformation matrices representing the relationship between the camera and T-RCM frames and that between the camera and patient frames, respectively.

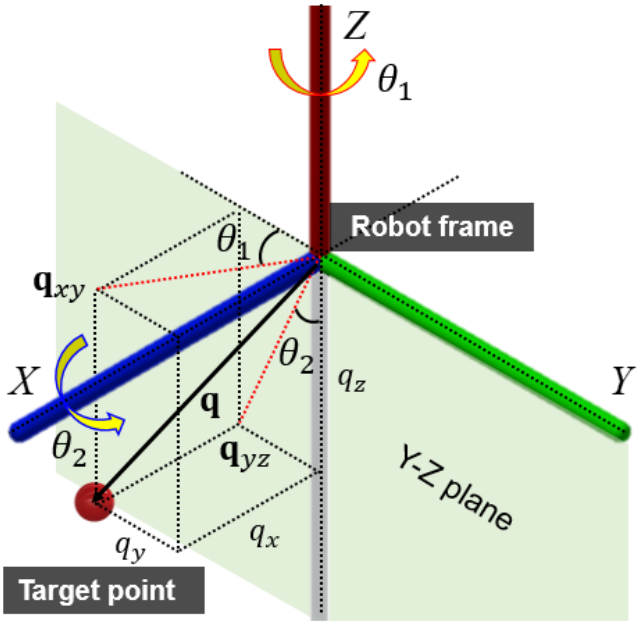

Fig. 29. Relationship between the T-RCM frame and the target point.

3.3.3 Tracking Algorithm

The z-axis of the T-RCM frame, which has the same orientation as the drilling axis, should be aligned with the target. That is, the target should lie on the z-axis of the T-RCM frame. To align the z-axis of the T-RCM frame to the target point with respect to the image frame (**p**), two rotation angles are calculated using the following steps: first, the target point with respect to the T-RCM frame, q, is calculated as follows (Fig. 28):

$$\mathbf{q} = \mathbf{T}_{\mathbf{I}}^{\mathbf{R}}\mathbf{p}, \tag{12}$$

Next, the angles denoted by θ_1 and θ_2 are calculated as follows (Fig. 29):

$$\begin{aligned} \theta_1 &= tan^{-1}\left(\frac{|q_x|}{|q_y|}\right), \\ \theta_2 &= tan^{-1}(\frac{|q_y|}{|q_z|}), \end{aligned} \tag{13}$$

where $q_x, q_y,$ and q_z are the elements of $\mathbf{q}$. Based on these angles, the drill orientation is automatically aligned to the target with a frame rate of 15 fps.

3.4 Experiments and Results

To verify that the developed mechanical system is ready for pre-clinical trials, verification of the robot's RCM accuracy, rigidity, and targeting test were performed. For the targeting test, a developed navigation system was integrated with the T-RCM.

3.4.1 Existence of an RCM

To evaluate the accuracy of the remote center of motion, we conducted pivot calibration about the T-RCM. For the pivot calibration, we used an optical tracking system (OTS) (Polaris spectra, Northern Digital Inc., Waterloo, Canada) and attached an OTS marker at the end effector of T-RCM, as shown in Fig. 30. During the pivot calibration, the T-RCM's roll rotation was positioned in 5° increments, while the yaw rotation was swept back and forth through its range of motion. By measuring the homogeneous transformation matrix, $\mathbf{T}_{\mathbf{M}}^{\mathbf{O}}$, from the OST frame to the marker frame, the vectors $\mathbf{b}_{post}$ and $\mathbf{b}_{tip}$ from the OTS frame and the marker frame to the RCM point could be obtained as follows:

$$\mathbf{b}_{post} = \mathbf{R}_{\mathbf{M}}^{\mathbf{O}}\mathbf{b}_{tip} + \mathbf{t}_{\mathbf{M}}^{\mathbf{O}}, \tag{14}$$

$$\begin{bmatrix} \mathbf{R}_{\mathbf{M}_1}^{\mathbf{O}} & -\mathbf{I} \\ \vdots & \vdots \\ \mathbf{R}_{\mathbf{M}_n}^{\mathbf{O}} & -\mathbf{I} \end{bmatrix} \begin{bmatrix} \mathbf{b}_{tip} \\ \mathbf{b}_{post} \end{bmatrix} = \begin{bmatrix} \mathbf{t}_{\mathbf{M}_1}^{\mathbf{O}} \\ \vdots \\ \mathbf{t}_{\mathbf{M}_n}^{\mathbf{O}} \end{bmatrix}, \tag{15}$$

where $\mathbf{R}_{\mathbf{M}}^{\mathbf{O}}$ is the rotational component and $\mathbf{t}_{\mathbf{M}}^{\mathbf{O}}$ is the translational component of $\mathbf{T}_{\mathbf{M}}^{\mathbf{O}}$. Using the pseudo-inverse of Eq. 9, the best fit of the least squares for vectors $\mathbf{b}_{tip}$ and $\mathbf{b}_{post}$ were obtained. Using these values, the pivot calibration RMS error could be calculated by subtracting each RCM point from the obtained RCM point using all sample points.

The RCM point RMS error referenced from the optical tracking frame was calculated by pivot

calibration. The RMS error of each axis was [0.22 0.28 0.22] mm, and the total RMS error was approximately 0.42 mm. Fig. 31 illustrates the result of pivot calibration as lines from the marker frame to the RCM point.

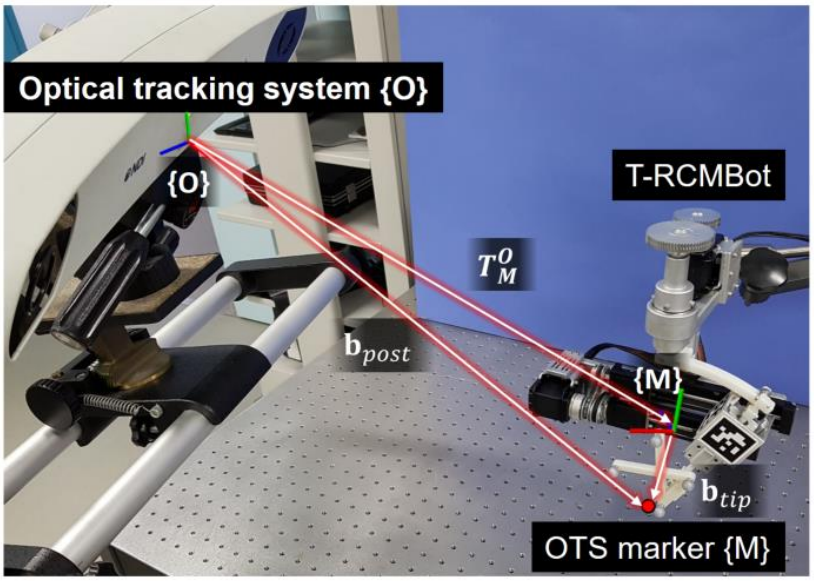

Figure 30. Experimental set-up of pivot calibration.

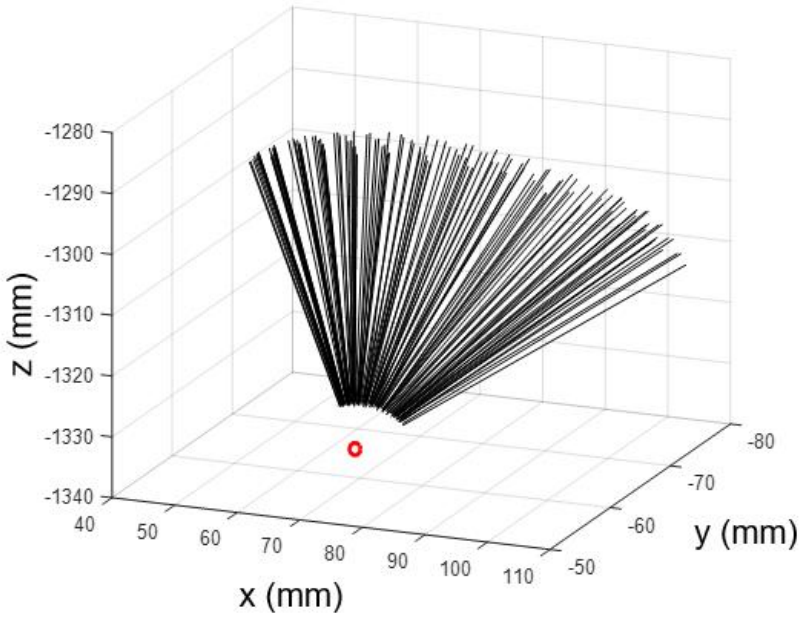

Figure 31. Calibration of the RCM point.

3.4.2 Rigidity Test about Tilting Motion

Because the maximum applied force on the y-axis of the drilling robot is approximately 17 N [60], the tilting mechanism, which is for yaw rotation, should be able to withstand more than 17 N for precise and safe operation. To confirm that the proposed RCM mechanism has sufficient rigidity to maintain the tilting angle, we conducted a tilting rigidity test, as shown in Fig. 32. Using a linear actuator-equipped load cell (UU-100K, CAS Corp., Yangju, Korea), an artificial external force was generated on the y-axis of the T-RCM. When this external force was applied to the T-RCM, we obtained the value of the applied force from the indicator and position information of the motor for yaw rotation. To intuitively show that the motor does not move during the tilting rigidity experiment, two stickers were attached to each belt. We then applied a 50 N force at tilting angles of 10°, 20°, and 30° and confirmed that the position of the motor did not change. In other words, the angle of the yaw rotation remained unchanged; therefore, the tilting mechanism of the T-RCM can withstand an external force that is sufficient to perform bone drilling.

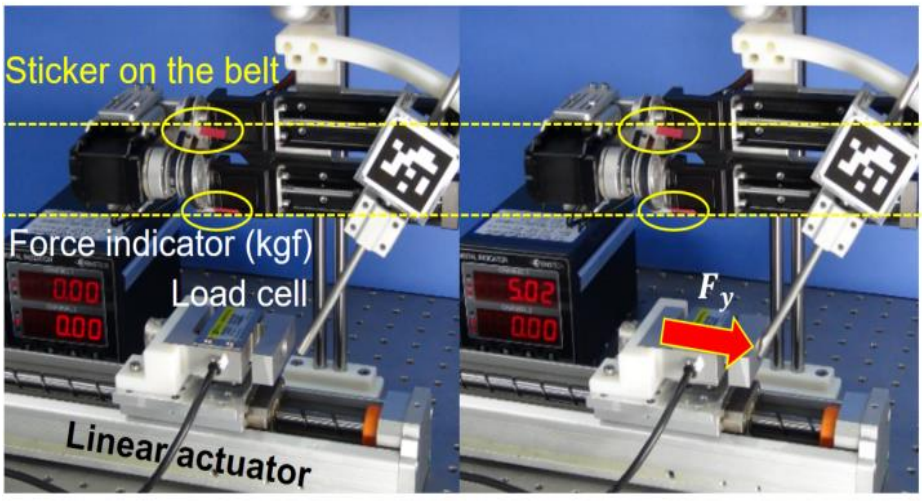

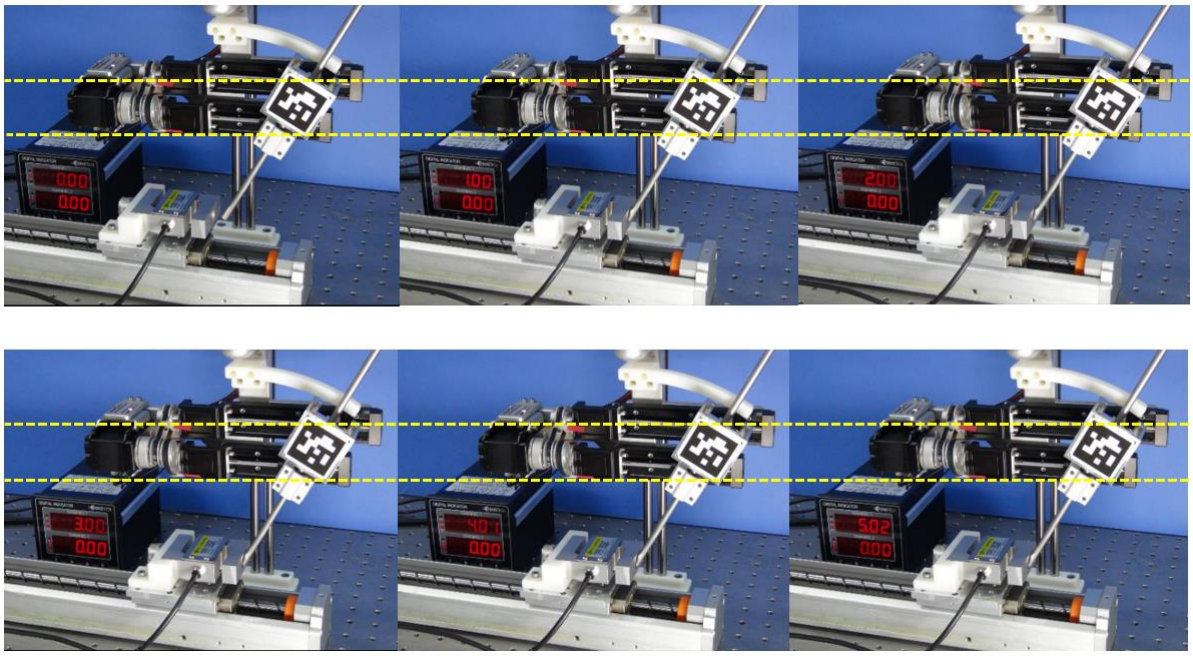

Fig. 32. Rigidity test. (a) Without an external force; (b) with an external force of approximately 50 N.

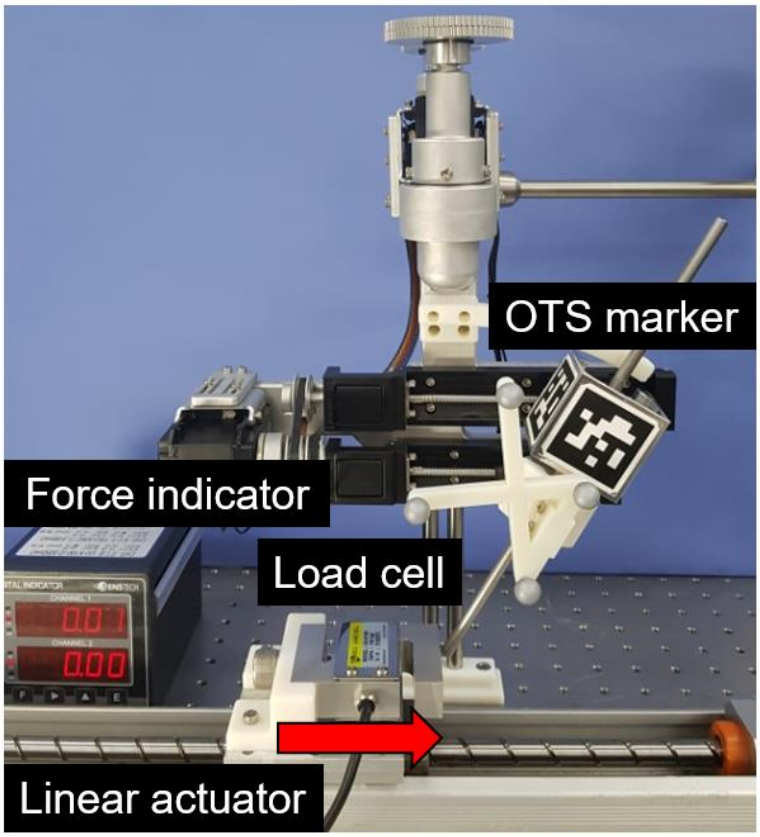

Fig. 33. Rigidity test using OTS and marker.

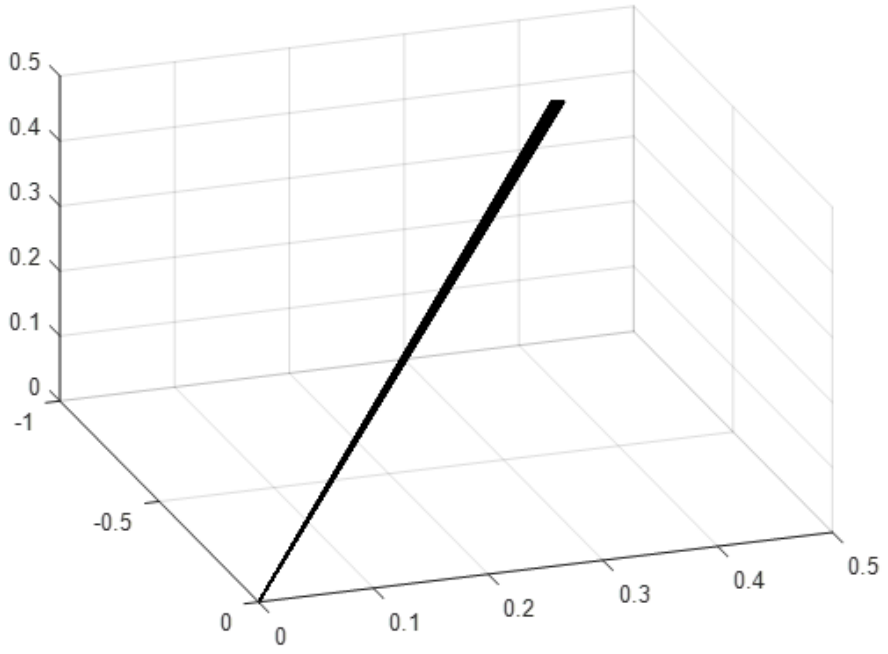

Fig. 34. Angular variation by external force from 10 N to 40 N (1.37°)

3.4.3 Targeting Test

To evaluate the precision of the T-RCM with the proposed navigation system, we conducted a set of targeting experiments. The targeting tests consisted of the following four steps:

1. A piece of paper with printed target points was pasted onto the reference marker.

2. The T-RCM was operated using the navigation system to align the drill axis toward the target point (Fig. 36(a)).

3. On completion of the alignment, the drill tip was inserted into and penetrated the paper target (Fig. 36(b)).

4. The distance errors between the designated and penetrated points were measured.

The experimental setup was virtually the same as that depicted in Fig. 28, expect that we directly used the reference marker as a target. Because we did not need to consider the image frame, the patient-to-image registration error was eliminated. A square-shaped paper target was attached to the top of the cubic marker, as shown in Fig 36(b). The paper target had four points, which formed a square with each side having a length of 22.50 mm.

We placed the marker under the robot in arbitrary positions and conducted 10 targeting tasks using the T-RCM with the proposed vision-guided navigation system. The four points on the paper target were penetrated at each position (see Fig. 36(c)). To measure the distance errors between each designated target point and penetrated hole, we used an Artec Spider 3D scanner and Artec Studio 9 software (Artec Europe Corp., Luxembourg, Germany), which has an accuracy of 0.03 mm. In addition, a 0.1-mm-diameter drill tip was used to ensure precise error measurements. If the pointing error is directly measured, the error could include additional error resulting from the incorrect attachment of the paper target to the reference marker. To reduce this error, we drew a rectangle using the four penetrated points, and compared the side lengths with the desired side length of 22.50 mm. The side lengths are listed in Table Ⅴ, and Fig. 36(d) shows one of the results obtained using the 3D scanner and software. The mean in-plane side length error was 0.28 mm, with a standard deviation of 0.34 mm and a maximum of 0.81 mm.

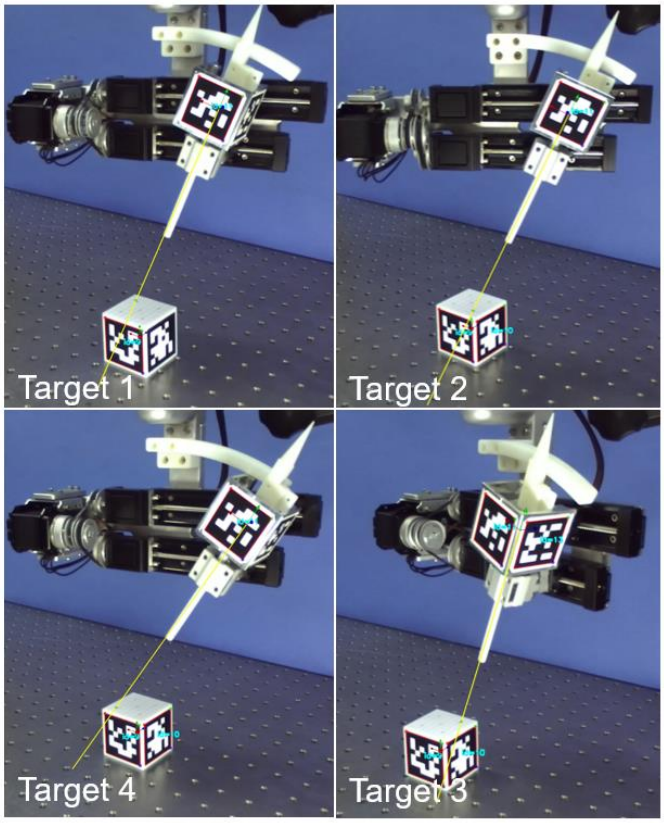

Figure 35. Targeting test about T-RCM with the navigation system

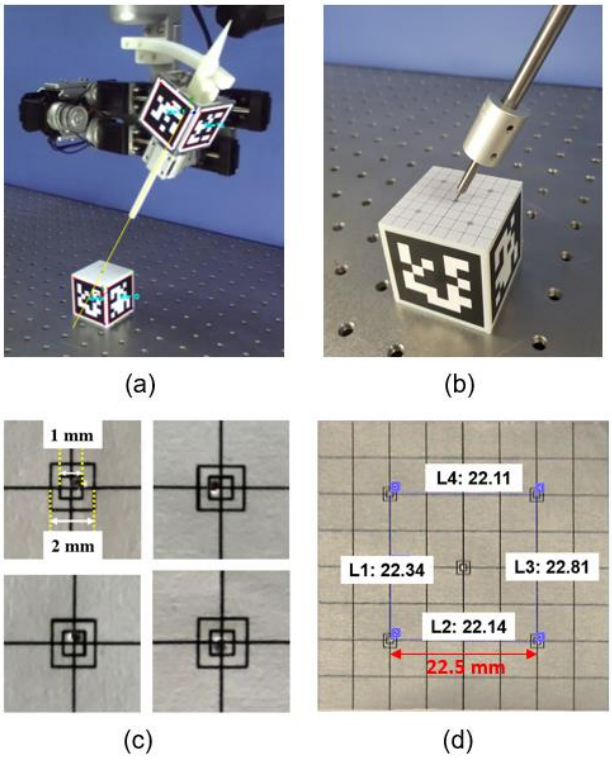

Figure 36. Targeting test. (a) Operation of the T-RCM with the navigation system; (b) pointing on the target; (c) close-up of the target; (d)

distances between the desired and penetrated points.

TABLE V

POINTING ERRORS OF THE PROPOSED RCM MECHANISM

Side number	l_1(mm)	l_2(mm)	$l_{\backslash 3}$(mm)	l_4(mm)
1	23.294	22.520	23.236	22.753
2	22.532	22.439	22.946	22.959
3	23.311	22.748	22.496	22.606
4	22.561	22.512	22.825	22.275
5	22.270	22.454	22.764	22.106
6	22.078	22.949	22.409	22.632
7	22.335	22.141	22.807	22.106
8	22.641	22.620	22.874	22.700
9	22.294	22.675	22.257	23.087
10	22.088	22.851	23.074	22.364

3.5 Discussion

The T-RCM mechanism, which has two DOFs, tilting and rotational motion, was developed to assist the bone drilling procedure and reduce the complexity of the drilling robot. Because the maximum applied force on the y-axis of the bone drilling robot is approximately 17 N [60], the tilting mechanism should be able to withstand more than 17 N for precise and safe operation. Using a rigidity test with respect to tilting, we have confirmed that the proposed mechanism can withstand up to 50 N without any change in the tilting angle; this force is approximately three times the maximum applied force to the tilting angle during bone drilling. Unlike other drilling robots, which use a high-performance motor [62][63], we improved the tilting rigidity by structurally reducing the torque applied to the motors. Not only tilting rigidity but also the flexural rigidity of the robot itself is important in real clinical applications. However, because the manufactured mechanism in this study is a prototype before clinical application, some deflections occur because of machining tolerance, assembly clearance, the contact angle of the bearing, and so on. To use the proposed mechanism for clinical applications, modifications of the components are required to achieve high flexural stiffness, and a flexural rigidity test should be completed.

Through the targeting test, it is confirmed that the robotic system has a targeting error of approximately 0.28 mm. Considering the mean lesion size of a bone biopsy, which is one of our target applications, is approximately 31 mm [64], a targeting error of 0.28 mm, which is approximately 1% of the target size, is sufficient. Although we focused on measuring the accuracy of the only mechanical system in this study, some inevitable error, such as errors in patient-to-image registration, camera calibration, and visual feedback delay, among other factors, should be considered in the vision-guided navigation system. For surgical practice, two major factors to decrease the system accuracy should be considered. First, the OTS's positioning error increases with the distance between the OTS and objects to be tracked [65]. This means that to ensure high system accuracy, the OTS should be positioned as close to the robot as possible. Second, although our system aimed to drill hard tissue, we should consider the patient motion caused by respiration or external drilling force. To compensate for the movement of the patient, image-to-patient registration is necessary. In this registration process, a reference marker is firmly fixed to the bone close to the target, so that it can be tracked

using the stereo camera [66]. After this image-to-patient registration, we can obtain information concerning the target position in real time, and the robotic system can align the drilling axis to the target using visual feedback (Fig. 6). Because this registration result highly affects the system accuracy, the registration should be accurately and reliably performed for surgical practice.

In the future, augmented reality (AR) techniques will be applied to show the workspace of the T-RCM and help the surgeon determine the initial position of the T-RCM. Further, we will improve the robotic system for use with specific applications, such as pedicle screw insertion and stereotactic brain surgery. To verify the feasibility of the robotic system for real surgery, additional experiments using swine or cadaver bones will be conducted afterward.

3.6 Conclusion

We developed a new mechanical-type RCM mechanism (T-RCM) for bone drilling based on a trigonometric ratio. To achieve high rigidity and resolution, a pair of linear actuators and a gearless arc-guide were applied to the proposed RCM mechanism. Integration of a vision-guided navigation system with the T-RCM enables automatic alignment of the robot with the target. The feasibility of the T-RCM integrated with a navigation system was verified for a novel medical application, i.e., bone drilling. The experimental results show that the T-RCM has sufficient RCM accuracy and rigidity for utilization by assistive robots for bone drilling. Through a targeting experiment, it was also confirmed that the proposed vision-guided robotic system guarantees high targeting performance. To the best of our knowledge, this is the first RCM mechanism designed for bone drilling.

IV. INTEGRATED ROBOTIC SYSTEM FOR BONE DRILLING

4.1 Dual Trigonometric Ratio based RCM Mechanism

To achieve high resolution and rigidity in RCM mechanism for the bone drilling, a prototype RCM mechanism has been reported previously by the authors [23]. This mechanism is based on a trigonometric ratio and employs a pair of linear actuators and a gearless arc guide. Given that the trigonometric RCM mechanism is applied only on one axis, the resolution and rigidity of the entire mechanism is insufficient for the actual bone drilling. In addition, this preliminary study showed that the workspace of the prototype was limited within an incomplete conical shape volume owing to the space required by the motor part for the rotation of the mechanism. The proposed second version has also resolved this limitation of the previous prototype.

4.1.1 Design Consideration

To conduct the bone drilling with the RCM mechanism, an orientation of the drill should be precisely guided and robustly maintained. Therefore, the RCM mechanism should satisfy the following conditions. First, the RCM mechanism should have high rigidity to withstand the reaction force of drilling. Second, the RCM mechanism should have high resolution to achieve precise drilling.

Wolf et al. [67] reported that the necessary force for tilting was approximately 17.3 N during bone drilling. To withstand the reaction force and enhance the stability of the robot, the RCM mechanism should have high rigidity. In addition, the modification of the drill orientation is not allowed during the bone drilling process unlike the needle insertion case in soft tissues. Therefore, higher resolution and accuracy are required for the precise alignment of the orientation in the first trial. The required target accuracy and rigidity of bone drilling are within 2 mm [9][11] and 17 N [67], respectively.

4.1.2 Structure and Workspace of the DT-RCM

The CAD design of the proposed DT–RCM is illustrated in Fig. 37. To generate RCM, a pair of ball-screw-based linear actuators, and a gearless arc-guide were used, as shown in Fig. 38. Accordingly, an RCM could be generated based on the same ratio between the height from the RCM point to each linear actuator and the feed rate of each linear actuator. For the implementation of the RCM mechanism to both axes, yaw and pitch rotations, we designed a connection mechanism that used a pair of linear guides with two blocks (SSE2BS8L–115–MC, MISUMI Group Inc., Tokyo, Japan). A pair of rails of linear guides was connected to the gearless arc-guide with bearings assembled on the guiding rods. Additionally, two of the blocks of each linear guide were connected to each ball-screw-based linear actuator with a revolute joint (see Fig. 39). To have yaw and pitch rotations in the execution of RCM, two sets of ball-screw-based linear actuators and a gearless arc-gude were orthogonally connected using the connection mechanism. Furthermore, based on the connection mechanism, a drilling mechanism could be assembled at the end of the RCM mechanism. Correspondingly, the workspace of the proposed RCM mechanism has a conical shape, which has 60° of the vertical angle (see Fig. 37).

We determined that the height ratio of the top and bottom are 2:1. The two ball-screw-based linear guides (LX1502C–B1–N-200, LX1502C–B1–N–100, MISUMI Group Inc., Tokyo, Japan) are operated by one rotary motor (MX–64R, Robotics Corporation, Seoul, Korea) and two sets of timing pulley and belt mechanisms. To equalize the feed rate of the linear actuators to the ratio of the height, we used a different pulley ratio equal to 1:2. The base of the DT–RCM was designed to connect to a passive arm. In addition, two ball-type reference markers (base and robot reference markers), were assembled on the robot. The base and robot reference markers were located at the base and end effector of the robot, respectively. Most of the parts were machined from aluminum, and the reference markers were fabricated using a rapid prototyping machine (Eden 250TM, Stratasys Ltd., Eden Prairie, USA). The size of the DT–RCM is approximately (340, 252, 243) mm.

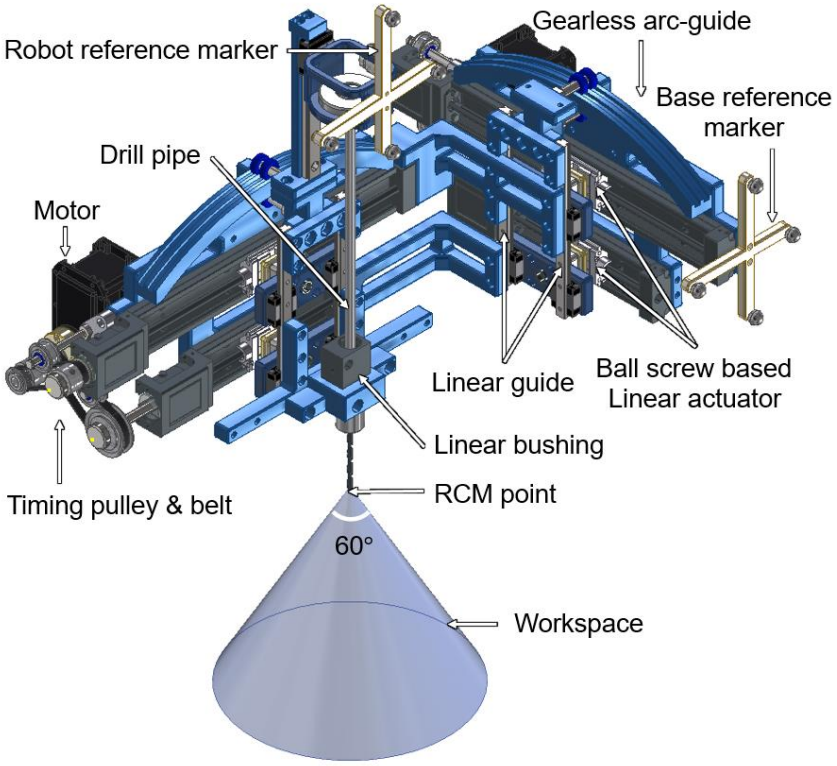

Fig. 37. Computer-aided-design (CAD) model and workspace of DT–RCM.

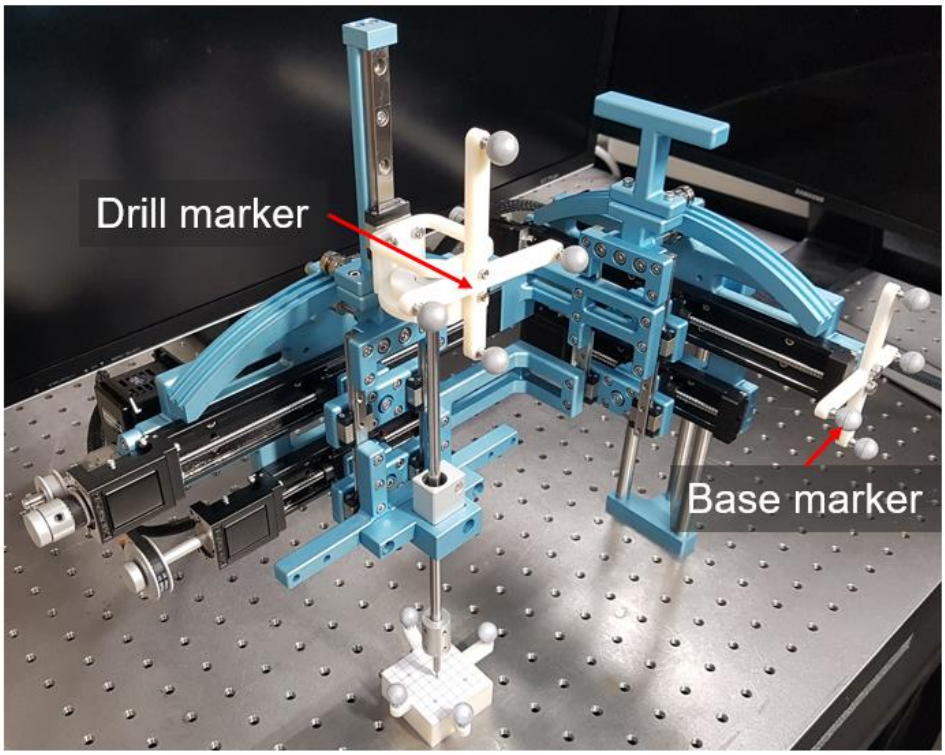

Fig. 38. Prototype of the DT–RCM.

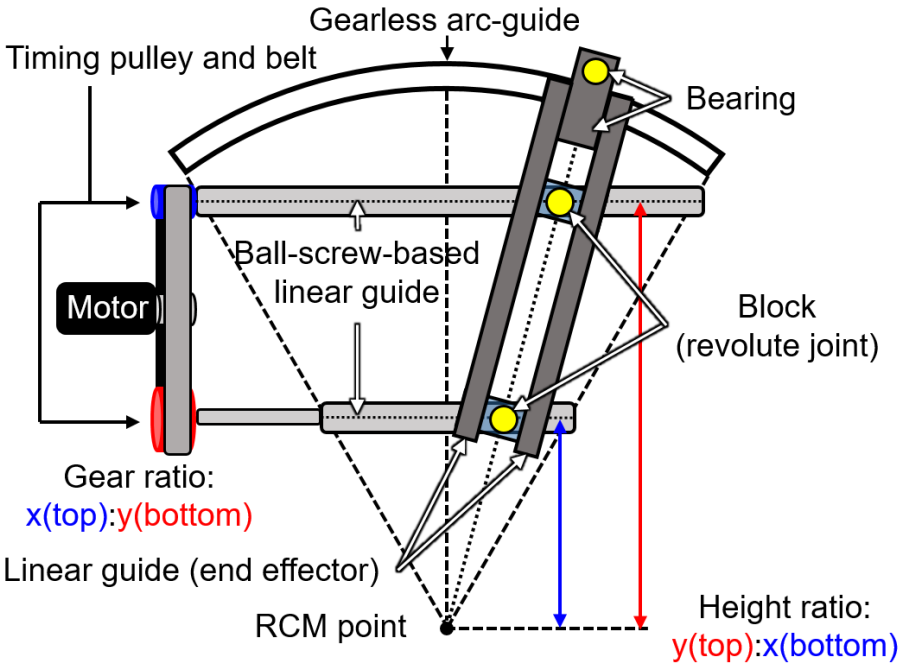

Fig. 39. Kinematic model for each rotational axis of dual trigonometric-ratio-based RCM mechanism (DT–RCM).

4.1.3 Static Analysis of Resolution and Force

A pair of linear actuators consisting of two ball-screw-based linear guides and a rotary motor was employed for yaw and pitch rotations. The lead of the linear guide was 2 mm/revolution, and the length between the upper linear guide and the RCM point was 100 mm. Therefore, when the rotary motor connected to the linear guide was rotated by one revolution, the tilting angle was changed by approximately 1.15°. The resolution of the tilting rotation is given by

$$\theta_{\text{res}} = \left(tan^{-1}\frac{l}{d}\right) \times \left(\frac{\theta_{\text{res.M}}}{360°}\right), \tag{16}$$

where l is the lead of the ball-screw-based linear guide, and d is the distance from the RCM point to the linear guide. As the resolution of the rotary motor $\theta_{res.M}$ is 0.088°, the mechanical resolution of the tilting rotation is theoretically equal to approximately 0.00028, and it is derived from the simplified model (Fig.

4(a)).

Using the ball-screw-based linear guide instead of directly using a rotary motor, the torque applied to the motor can be markedly reduced to maintain the orientation. When an external force, F_y, is applied to the RCM point, the reaction force applied to the ball-screw-based linear actuator, R_y, can be described as shown in Fig. 40(a). The applied force is divided into vertical and horizontal forces on the slope of the screw, as shown in Fig. 40(b). The horizontal force F_h affects the rotation of the screw and is expressed by

$$\sum F_h = 0; Pcos\beta - Qsin\beta = \mu N, \tag{17}$$

where the coefficient of friction μ in the ball-screw mechanism is zero, and Q is the same as the reaction force R_y. Therefore, P, which is the force that generates the torque on the screw, is obtained by

$$P = R_y tan\beta, \tag{18}$$

As the lead and diameter of the ball screw are 2 mm and 5 mm, respectively, the lead angle β is 21.8°, and P is approximately $0.4R_y$. Finally, the motor torque τ required to maintain the external force is calculated as follows:

$$\tau = P\frac{d}{2}, \tag{19}$$

where d is the diameter of the ball screw and the value of R_y is the same as the value of F_y. Therefore, the motor requires $0.001F_y$ mN to maintain the tilting angle from the external force F_y. Considering that 0.1Fy mN is required when a rotary motor is used directly, we have proven that the proposed RCM mechanism can reduce the required torque to maintain a tilting angle by a factor of 100. The proposed mechanism

acts not only as an RCM mechanism but also as a reducer of the motor.

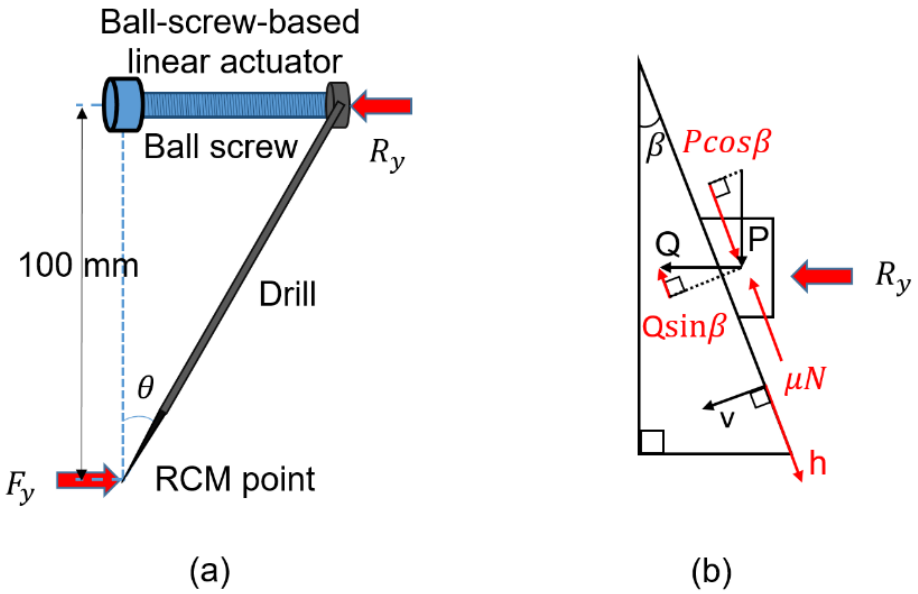

Fig. 40. Static analysis of the DT–RCM. (a) Free body diagram, (b) and force on the slope of the screw.

4.2 Single Motor based Drilling Mechanism

We propose a rolling-friction-based drilling mechanism generated with the use of a single motor. Although the rolling-friction-based drilling mechanisms have already been reported by the authors [68], we focused on the reduction of the number of the motors to be cost effective and free from motor synchronization. In addition, a release mechanism between the robot and the drill, which is one of main advantages of the friction-based-drilling mechanism, was still applied to ensure surgical safety.

4.2.1 Design of the Proposed Drilling Mechanism

The rolling-friction-based drilling mechanism uses a rolling friction force between a cylindrical pipe guided by linear bushing, and two linear, symmetrically angled rubber rollers on both sides of the pipe. Using the rolling friction force, the linear and rotational drilling motions could be generated on the pipe. To implement the rolling-friction-based drilling mechanism with a single motor, we designed a novel drilling mechanism, as illustrated in Fig. 41. To achieve an angular roller orientation, an angle-adjusting unit (REG25, MISUMI Group Inc., Tokyo, Japan) was applied. In addition, a positioning unit (XKCS30, MISUMI Group Inc., Tokyo, Japan) was used to generate a normal force from the rollers to the pipe. To rotate both rollers with one motor, timing pulleys were mounted on the motor and on both shafts on which each roller was fixed. A torque was conveyed with timing belts to achieve rotational motion of the roller. Two sets of the idler and guide rollers were used to apply an appropriate tension to the belts. The reasons for using the pulley and belt mechanism are to enable power transfer even when the roller is tilted, and to implement the release mechanism, as presented in the next section.

We set the angle of the roller to 1° and the diameter of the pipe to 6 mm so that the feed of the drilling motion f is approximately 0.33 mm. The feed of the drilling motion is calculated as follows:

$$f = 2\pi r_p tan\theta \ , \tag{20}$$

where r_p and θ represent the pipe radius and angle of the roller, respectively. The feed could be adjusted by changing the angle of the roller and the diameter of the pipe. Except for the commercial unit, most of the parts of the drilling mechanism were machined with aluminum.

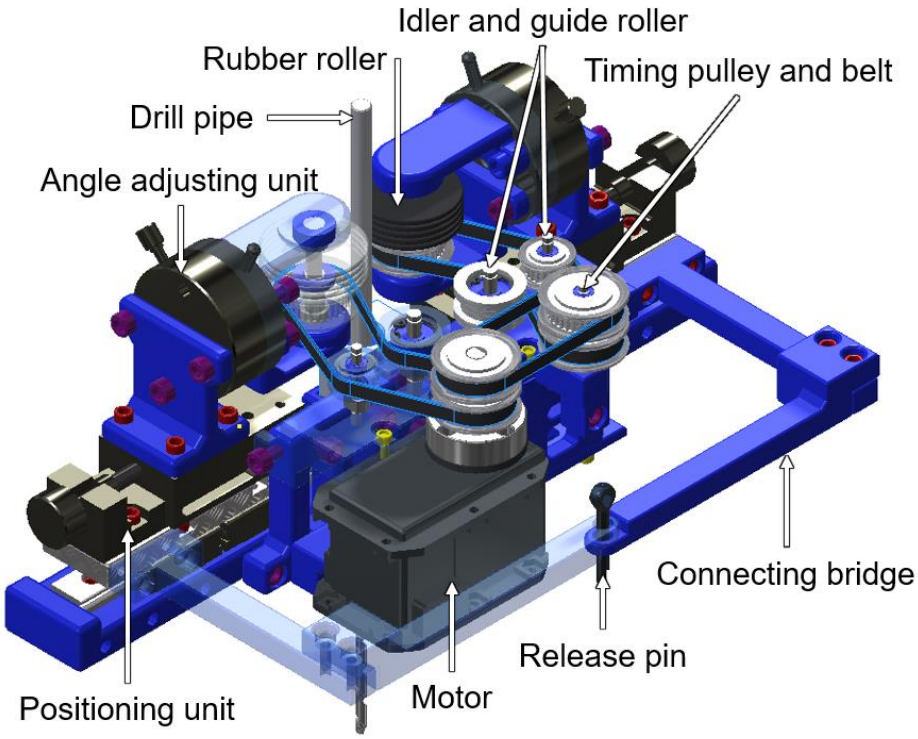

Fig. 41. CAD model of the proposed drilling mechanism.

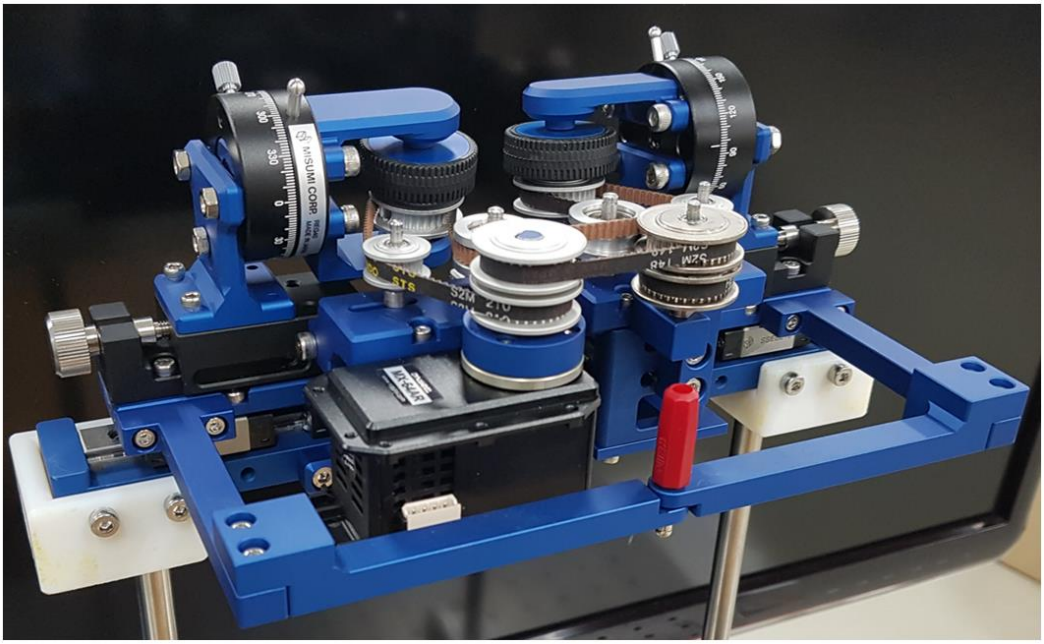

Fig. 42. Prototype of the proposed drilling mechanism.

4.2.2 Release Mechanism

A simple and quick release function is one of the main advantages of the rolling-friction-based drilling mechanism. When the operator only separates the rollers from the pipe, the friction force is removed and the drilling motion stops. Even if the motors are still running, the pipe with the drill tip can be removed from the robot.

To implement the release mechanism in the proposed drilling mechanism, we used the pulley and belt mechanism with pulley idlers and guide rollers, as shown in Fig. 43. Each roller is connected to the angle–adjusting unit, positioning unit, and on the corresponding part of the connecting bridge. This connected assembly is referred to as a roller part. In the drilling mode, both side roller parts are assembled by the release pin, as shown in Figs. 42 and 43(a). Given that the distance of the two parts is fixed by the release pin, a normal force for generating a fiction force could be applied from the rollers to the pipe using the positioning unit. When the positioning unit moves the roller part toward the pipe, the positions of the motor,

idlers, and guide rollers (which are fixed on the base of the drilling mechanism) are not changed, but the pulley connected to the roller moves toward the pipe (Fig. 43(a)). Consequently, the tension of the timing belts is generated, which transfers the rotational motion from the motor to the roller. Conversely, when the operator pulls out the pin, both roller parts are pushed to both sides by the reaction forces generated from the application of the normal force, and the rollers and pipe become disconnected, as shown in Fig. 43(b). Therefore, in the release mode, the drilling mechanism no longer transfers the rolling frictional force to the pipe, the drill stops, and can thus be easily removed.

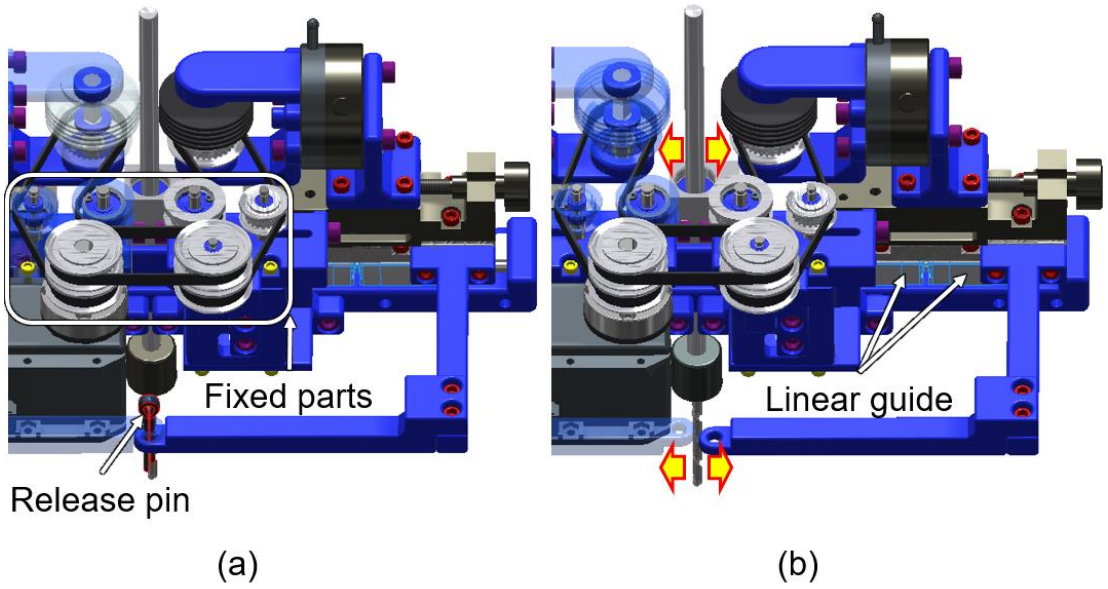

Fig. 43. Release mechanism using pin and linear guides. (a) Drilling mode. (b) Release mode.

4.3 Navigation System

An image-guided navigation system using infrared based OTS was integrated into the proposed robotic system to a) align the orientation of the drill and b) insert the drill tip to the target.

4.3.1 System Configuration

The navigation system consists of an infrared based OTS and three reference markers. These include the base, robot, and patient reference markers, as shown in Fig. 44. We used an OTS (Skadi, Digitrack Inc., Daegu, Korea), which has a precision of approximately 0.2 mm, and customized ball-based reference markers. The pose of each reference marker could be obtained from the OTS frame. Because the frame of the base reference marker is mechanically matched to the base of the robot, and because the relative position from the base to the RCM point is constant, the position of the RCM point could be tracked by the base reference marker. The entry point is known with respect to the patient reference marker based on the registration results, as explained in the next section. Therefore, from the base and patient reference markers, the relative position between the RCM point and the entry point of the drilling could also be tracked. This helps the operators to place the robot's RCM point around the entry point. In addition, given that the frame of the robot reference marker was aligned at the top-center of the pipe, which is the end-effector of the robot, the orientation and position of the drill could be obtained through the robot reference marker without the extra robot-to-OTS calibration or kinematic calculation. From the robot and patient reference marker, we could also estimate the angles and distance from the drill tip to the target.

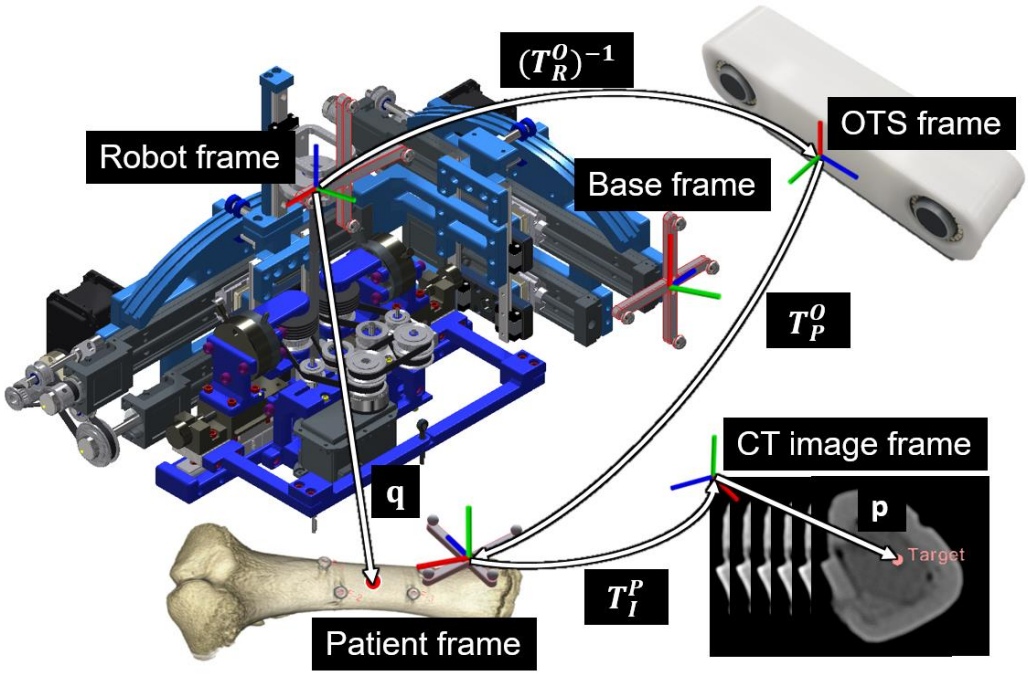

Fig. 44. Configuration of the navigation system.

4.3.2 Registration between the Robot and CT Image Frame

To guide the orientation of the drill and insert the drill tip to the target in the bone tissue with the robotic system, frame matching between the robot and computed tomography (CT) images should be conducted. For this frame matching, we have to formulate the transformations from a) the OTS to the robot frame ($\mathbf{T_R^O}$), b) from the OTS to the patient frame ($\mathbf{T_P^O}$), and c) from the patient to the CT image frame ($\mathbf{T_I^P}$). Using the robot and patient reference markers, $\mathbf{T_R^O}$ and $\mathbf{T_P^O}$ could be directly obtained from the OTS. Unlike these, $\mathbf{T_I^P}$ is an unknown. Thus, a paired-point registration [69] was conducted as a patient-to-image registration to identify accurate $\mathbf{T_I^P}$ estimates using artificial markers, which were attached on swine femur samples. Fig. 44 shows the configuration of the registration process, and a transformation from the robot frame to the image frame ($\mathbf{T_I^R}$) is calculated using the following equation:

$$\mathbf{T}_{\mathbf{I}}^{\mathbf{R}} = (\mathbf{T}_{\mathbf{R}}^{\mathbf{0}})^{-\mathbf{1}}\mathbf{T}_{\mathbf{P}}^{\mathbf{0}}\mathbf{T}_{\mathbf{I}}^{\mathbf{P}}, \tag{21}$$

4.3.3 Tracking Algorithm

A tracking algorithm for aligning and inserting the drill to the target has been developed. The algorithm ensures that the orientation of DT–RCM is aligned to the orientation of the target and that the drilling motion from the proposed drilling mechanism is conducted until the drill tip position reaches the target. Because the z-axis of the robot frame mechanically coincides with the drilling axis, we set the z-axis of the robot frame to be toward the target for the alignment. To accomplish this, the vector $\mathbf{q}$ from the origin of the robot frame to the target should be obtained as follows (Fig. 44):

$$\mathbf{q} = \mathbf{T}_{\mathbf{I}}^{\mathbf{R}}\mathbf{p}, \tag{22}$$

where $\mathbf{q}$ (q_x, q_y, q_z) is a vector from the origin of the robot frame to the target, and $\mathbf{p}$ is the vector from the origin of the image frame to the target. The yaw and pitch angles for the alignment of the z-axis of the robot frame are denoted by θ_1 and θ_2, and are calculated as follows (Fig. 45):

$$\begin{aligned} \theta_1 &= tan^{-1}\left(\frac{|q_y|}{|q_z|}\right), \\ \theta_2 &= tan^{-1}\left(\frac{|q_x|}{|q_z|}\right), \end{aligned} \tag{23}$$

According to the two desired angles, the orientation of DR–TCM is aligned to $\mathbf{q}$. Furthermore, q_z indicates the distance from the robot frame to the target. To allow the drill to reach the target, the proposed drilling mechanism is activated until q_z has a length that is equal to the distance from the robot's frame to the drill tip. This is mechanically determined by the length of the pipe and the drill tip. The calculation and

visual feedback of the tracking algorithm is processed with a frame rate of 54 frames per second (fps).

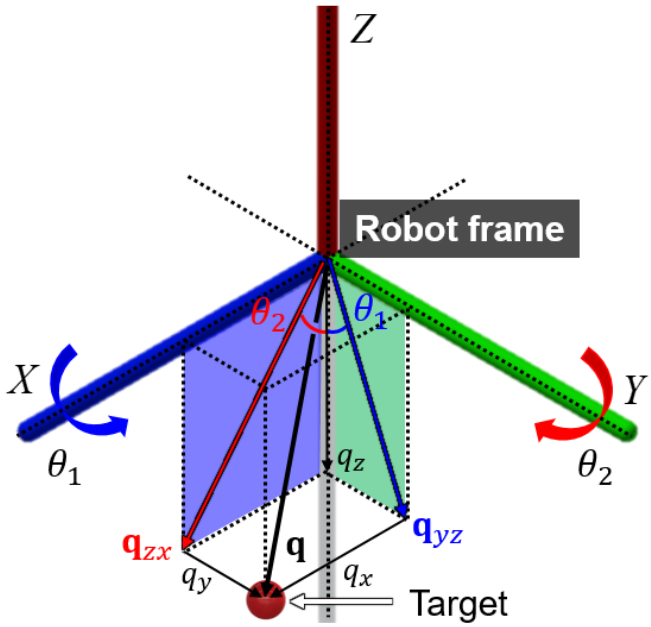

Fig. 45. Relationship between robot frame and target point.

V. EXPERIMENTS AND RESULTS

5 Experiments

To demonstrate that the proposed DT–RCM has increased resolution and rigidity, we conducted a series of experiments, including RCM accuracy, rigidity, targeting accuracy, and resolution tests. Furthermore, an ex vivo drilling test with swine femur samples was conducted to verify the feasibility of the bone drilling robotic system.

5.1 Accuracy Test for RCM

To evaluate the accuracy of the RCM, we conducted an RCM accuracy test based on a pivot calibration. We used the OTS and the robot reference marker, which was assembled at the end effector of the DT–RCM, as shown in Fig. 46. When the DT–RCM generates RCM, which implements tilting motions along the pitch axis by increasing the orientation by 15° with respect to the yaw axis from -30° to 30°, OTS tracks the robot reference marker. A homogeneous transformation matrix from the OTS frame to the robot frame $\mathbf{T}_{\mathbf{R}}^{\mathbf{O}}$ is measured, and the vector from the OTS frame to the RCM point $\mathbf{b}_{post}$ is obtained as follows,

$$\mathbf{b}_{post} = \mathbf{R}_{\mathbf{M}}^{\mathbf{O}}\mathbf{b}_{tip} + \mathbf{t}_{\mathbf{M}}^{\mathbf{O}}, \tag{24}$$

$$\begin{bmatrix} \mathbf{R}_{\mathbf{M}_1}^{\mathbf{O}} & -\mathbf{I} \\ \vdots & \vdots \\ \mathbf{R}_{\mathbf{M}_n}^{\mathbf{O}} & -\mathbf{I} \end{bmatrix} \begin{bmatrix} \mathbf{b}_{tip} \\ \mathbf{b}_{post} \end{bmatrix} = \begin{bmatrix} \mathbf{t}_{\mathbf{M}_1}^{\mathbf{O}} \\ \vdots \\ \mathbf{t}_{\mathbf{M}_n}^{\mathbf{O}} \end{bmatrix}, \tag{25}$$

where $\mathbf{b}_{tip}$ is the vector defined for the RCM point in the robot frame, and $\mathbf{T}_{\mathbf{R}}^{\mathbf{O}}$ is divided into the rotational component $\mathbf{R}_{\mathbf{M}}^{\mathbf{O}}$ and the translational component $\mathbf{t}_{\mathbf{M}}^{\mathbf{O}}$. The best solutions for the vectors $\mathbf{b}_{post}$ and $\mathbf{b}_{tip}$ were calculated from the pseudo-inverse of (10). With the pivot calibration, we were able to measure a root-

mean-square (RMS) error of 0.47 $\pm$ 0.22 mm, and a set of $\mathbf{b}_{tip}$ is illustrated in Fig. 47.

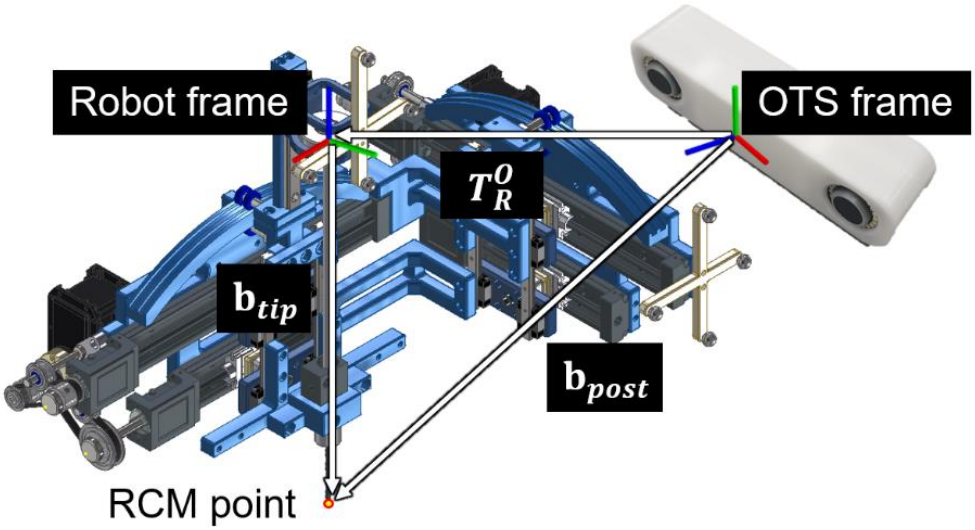

Fig. 46. Experimental setup of pivot calibration.

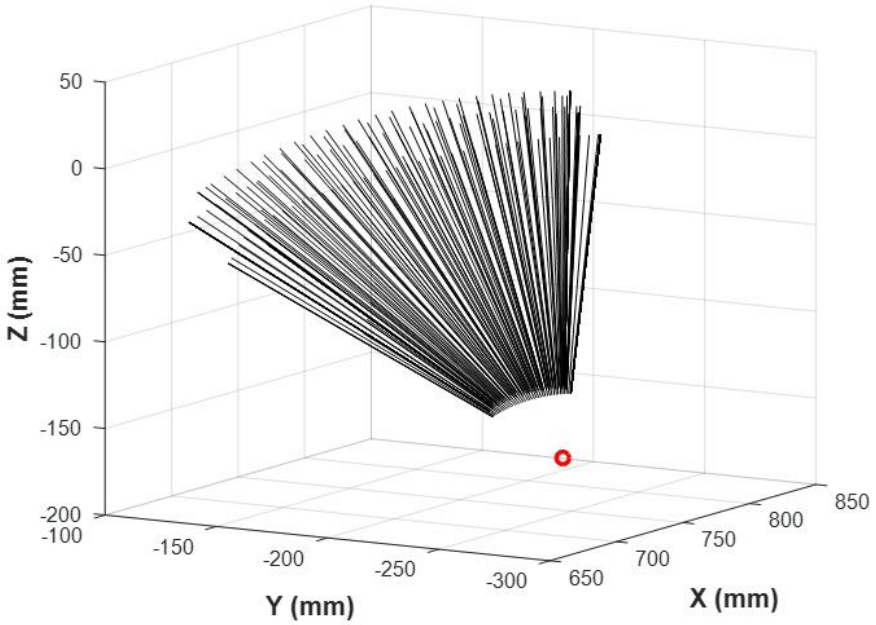

Fig. 47. Pivot calibration of the RCM point.

5.2 Rigidity Test for Yaw and Pitch Axes

To maintain the orientation of the drill during the bone drilling task, the DT–RCM should withstand forces larger than 17 N, that is the maximum applied drilling force on the tilting axis [67]. In this test, the maximum applied force at the end-effector was set to 51 N, which is three times the actual during force. We used a linear actuator and load cell (UU–100K, CAS Corporation, Yangju, Korea) to induce and measure an artificial force. The forces were applied to both axes of the yaw and pitch as shown in Fig. 48.

The position of the motor was measured with the equipped encoder during the application of the external force. It was thus confirmed that the position of the motor did not change until the external force increased to 51 N. This implies that the two DOF of the DT–RCM could be maintained from the drilling force. In addition, to measure the flexural rigidity of the mechanism, we obtained the homogeneous transformation matrices of the base and robot reference marker using the OTS during the rigidity test. Given that the base reference marker is fixed, and the only pose of the robot reference marker is affected by external forces, the changes of the rotation in the robot frame based on the base frame $\mathbf{R}_{\mathbf{R}'}^{\mathbf{R}}$ could be obtained using the following equation:

$$\mathbf{R}_{\mathbf{R}'}^{\mathbf{R}} = (\mathbf{R}_{\mathbf{R}}^{\mathbf{O}})^{-1}(\mathbf{R}_{\mathbf{B}}^{\mathbf{O}})(\boldsymbol{R}_{\mathbf{B}}^{\mathbf{O}})^{-1}(\boldsymbol{R}_{\mathbf{R}'}^{\mathbf{O}}), \tag{26}$$

where $\boldsymbol{R}_{\mathbf{R}}^{\mathbf{O}}$ and $\boldsymbol{R}_{\mathbf{R}'}^{\mathbf{O}}$ are the rotational matrices from the OTS frame to the robot frame before and after the induction of the external force, and $\boldsymbol{R}_{\mathbf{B}}^{\mathbf{O}}$ is the rotational matrix from the OTS frame to the base frame. Accordingly, use of the computed Euler angles from $\mathbf{R}_{\mathbf{R}'}^{\mathbf{R}}$ allows the estimation of the angular difference of the robot frame with and without the external force. The angular differences evoked owing to the external force of 51 N on the x-axis and y-axis are 0.3°° and 0.55°,° respectively. However, given that the joints of the DT–RCM did not move, the angular difference is only attributed to the bending of linkages.

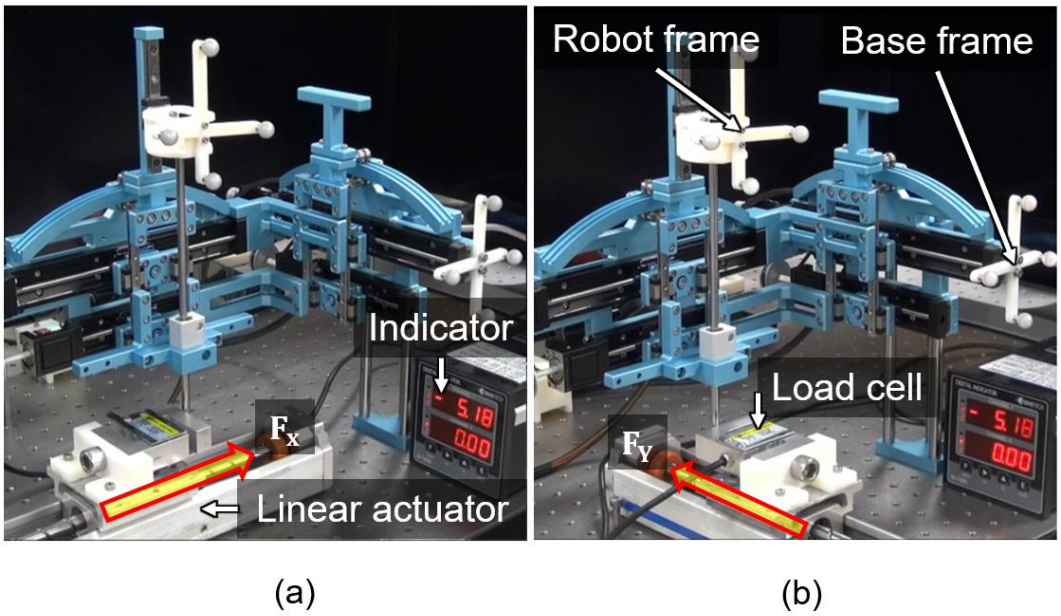

Fig. 48. Rigidity test. (a) Application of an external force of 51 N on the x-axis. (b) Application of an external force of 51 N on the y-axis.

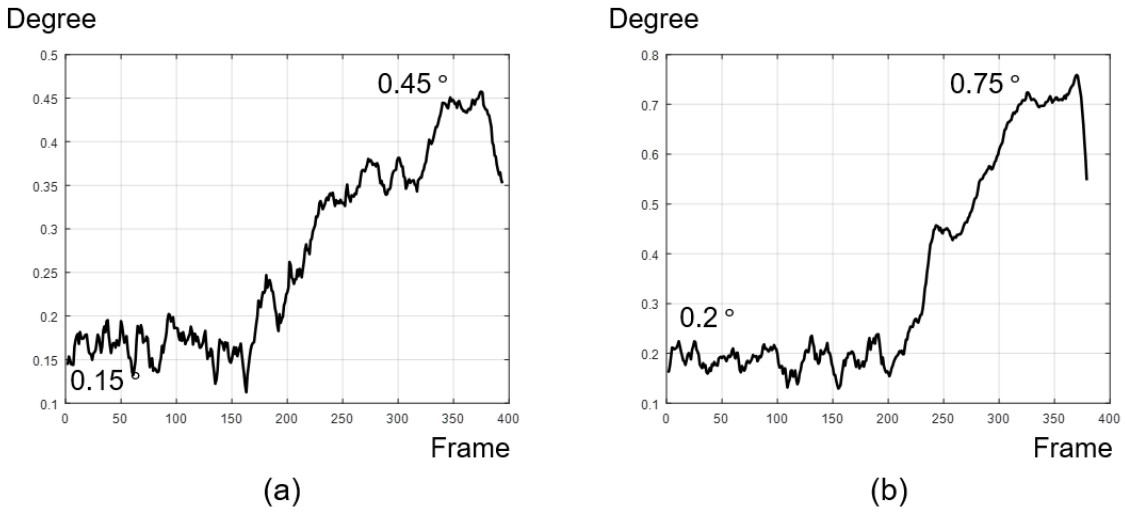

Fig. 49. Result of the rigidity test. (a) External force on x-axis. (B) on the y-axis.

5.3 Targeting Accuracy and Resolution

To evaluate the targeting accuracy and resolution of the DT–RCM, a targeting test was conducted with the navigation system. We used the DT–RCM, OTS, and the robot and patient reference markers, as shown in Fig. 50(a). To simplify the patient-to-image registration and focus on the mechanical targeting accuracy of the proposed RCM mechanism, a piece of paper with a square shape was pasted on the patient reference marker and was used as the target (Fig. 50(b)). The position of the targets could then be directly obtained from the OTS and the patient reference marker without an extra patient-to-image registration. Based on the proposed tracking algorithm, the drilling axis of the DT–RCM could be aligned to the targets. Subsequently, we inserted the drill tip in a specific direction so that the robotic system could guide it (Fig. 50(b)). We used a drill tip with a diameter of 0.1 mm to precisely measure the accuracy. Finally, we measured the distances of each side length from the penetrated four targeted points, and compared them with the designed length of 22.50 mm (Fig. 50(c) and (d)). The reason for measuring the side lengths of the square rather than directly measuring the targeting error about each point is to eliminate the human error, which could occur when the target paper is attached to the patient reference marker.

We conducted ten targeting test trials and obtained 40 side lengths, as listed in Table Ⅵ. The side lengths of the targeted points were measured with the use of the Artec Spider 3D scanner (with an accuracy of 0.03 mm) and the Artec Studio 9 software (Artec Europe Corporation, Luxembourg). The mean distance error of the targeted points was 0.138 mm with a standard deviation of 0.137 mm. In addition, to evaluate the repeatability performance of DT–RCM, we used the coefficient of variation (CV) [70]. The CV of the proposed RCM mechanism was approximately 0.6%, and was obtained by dividing the standard deviation and the mean distance between points corresponding to the penetrated locations.

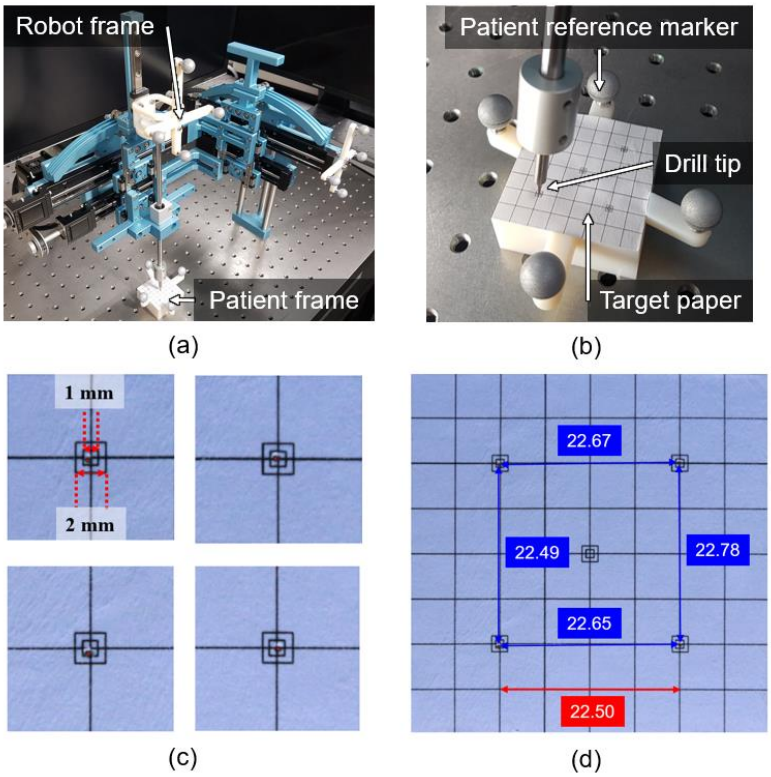

Fig. 50. Targeting test. (a) Aligning the orientation of the drill with DT–RCM and a navigation system. (b) Close-up view of the pointed target, (c) close-up view of the penetrated points, and (d) distances between the penetrated points.

TABLE VI

TARGETED SIDE LENGTHS

Side Number	l_1 (mm)	l_2 (mm)	l_{l3} (mm)	l_4 (mm)
1	22.674	22.783	22.649	22.493
2	22.621	22.576	22.849	22.676
3	22.765	22.342	22.582	22.413
4	22.559	22.712	22.544	22.665
5	22.358	22.714	22.669	22.683
6	22.349	22.509	22.634	22.795
7	22.469	22.438	22.719	22.487
8	22.750	22.754	22.560	22.681
9	22.663	22.264	22.574	22.471
10	22.594	22.568	22.502	22.596

5.4 Ex-Vivo Drilling Test on Swine Femurs

To verify the feasibility of the integrated bone drilling robotic system, which consisted of the DT–RCM, single motor-based drilling mechanism, and image-guided navigation system, an ex vivo drilling test was performed on swine femur samples. The reason for using bones from pigs is based on the fact that their densities and facture stresses closely resemble those of the human bones [71, 72]. In addition, we used bone samples, which were kept in cold storage because the properties and structures between living and nondried bones are different [73, 74].

Our target drilling task pertains to bone biopsies. In these instances, the surgeons need to drill at the target lesion to obtain a bone tumor or marrow for diagnosis. The experimental setup was the same as that depicted in Fig. 51, and the workflow of the drilling test is summarized in Fig. 52. Before conducting the drilling test, we pulled out the bone marrow and inserted medical cement to clearly identify the drilling path in the CT image. In addition, four screws were inserted on the surface of the bone samples. These were used as fiducial markers for the patient-to-image and image-to-image registrations. After the completion of the aforementioned preparations, the preoperative CT image of the bone sample was used to designate an arbitrary target point around the middle of the inserted cement using 3D Slicer (www.slicer.org). To obtain the position of the designated target based on the OTS frame, the patient-to-image registration—which was conducted to achieve frame matching between the actual bone anatomy and the pre-operative CT image—was conducted using the fiducial markers. After the patient-to-image registration was completed, the relative position between the robot and target was tracked using the navigation system. Based on the tracking information, the drill was aligned and inserted in the target using the DT–RCM and the drilling mechanism in successive order. Finally, to confirm the drilling outcome, a post-operative CT image was acquired and used. Based on the image-to-image registration for frame matching between the pre- and post-operative CT images, we measured the drilling error between the designated target in the pre-operative CT image and the actual drilled point in the post-operative CT image.

We conducted this ex vivo drilling test on 10 swine femurs. Fig. 53 shows typical pre- and post-

operative CT images. In both CT images, we can identify the four fiducial markers used for the registration, and designate the target point and drilled point. Based on the image-to-image registration using the fiducial markers from each CT image, we observed the homogenous transformation from the pre-operative to the post-operative CT images. By multiplying this matrix with the target point in the pre-operative CT image, and by comparing the drilled point in the post-operative CT image, the target registration error (TRE) was measured, as listed in Table Ⅶ. The fiducial registration errors (FRE) associated with the patient-to-image and image-to-image registrations, denoted by FRE1 and FRE2, are also listed in Table Ⅶ. The mean of the TRE, which denotes the drilling accuracy of the integrated robotic system, was 1.11 mm, and the standard deviation was 0.29 mm. This indicates that FRE1 and FRE2, which are error factors resulting from the navigation system, are equal to 0.38 mm and 0.28 mm, respectively.

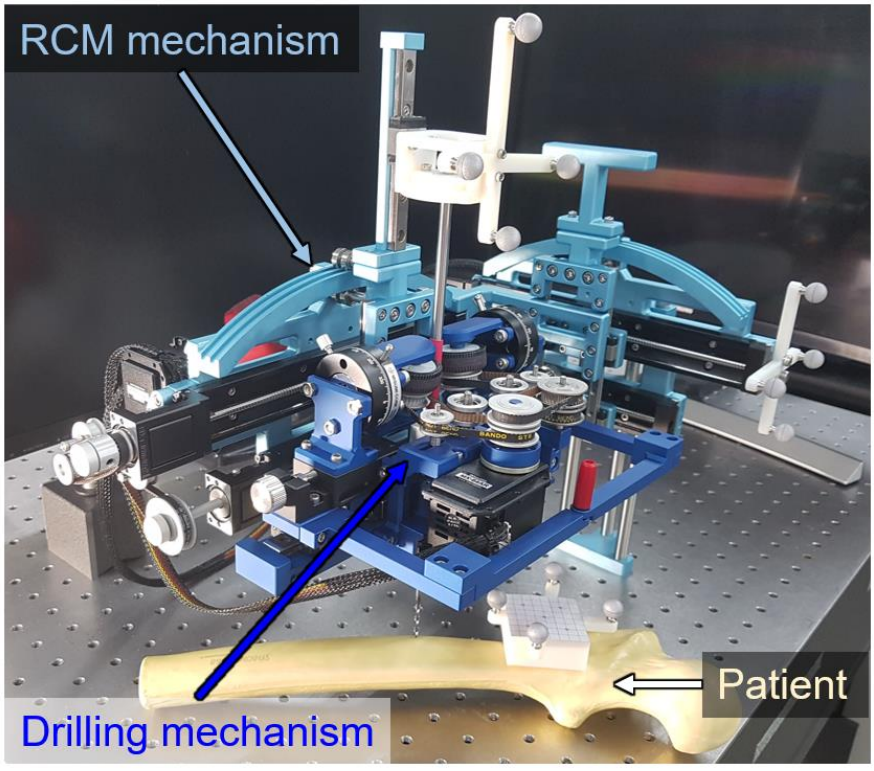

Fig. 51. Configuration of the proposed bone drilling robotic system

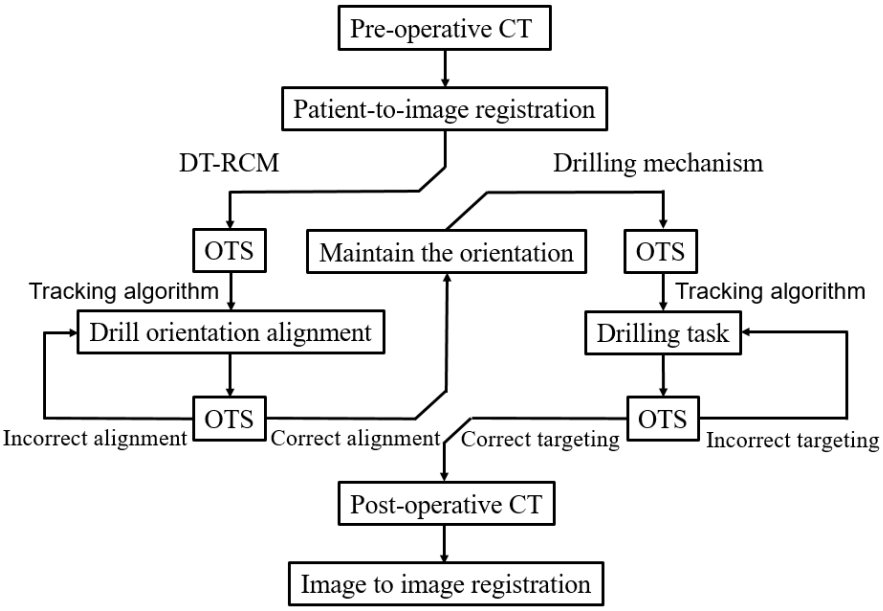

Fig. 52. Workflow of the drilling test.

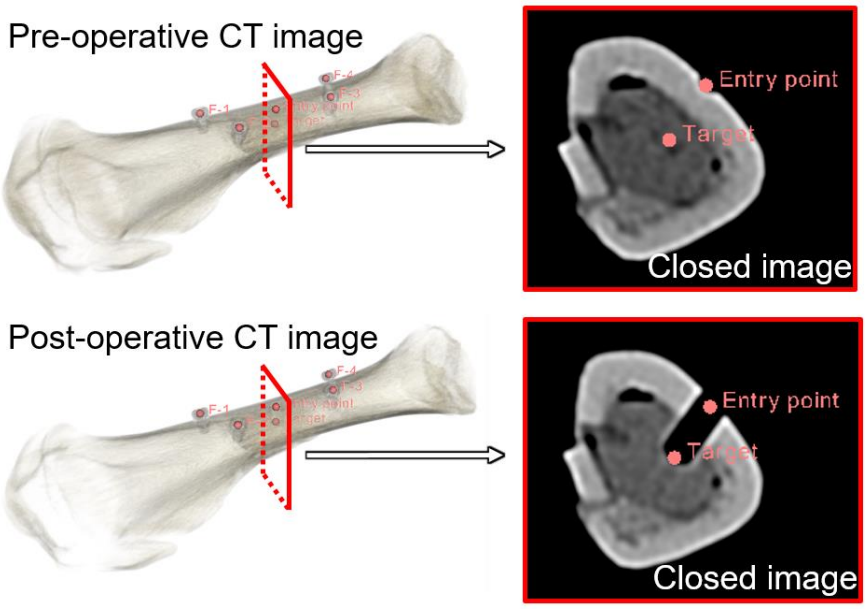

Fig. 53. Pre- and postoperative CT images of the swine femur.

TABLE Ⅶ

TARGETING ERRORS OF THE DRILLING TEST

	FRE_1 (mm)	FRE_2 (mm)	TRE (mm)
1	0.367	0.291	1.252
2	0.472	0.192	1.121
3	0.313	0.296	0.872
4	0.414	0.309	0.847
5	0.438	0.315	1.116
6	0.397	0.368	1.729
7	0.253	0.313	0.976
8	0.498	0.225	0.861
9	0.292	0.374	0.786
10	0.324	0.142	1.501
Aver-age	0.377	0.283	1.106

VI. DISCUSSION

A new type of RCM mechanism was developed and tested. Although the proposed mechanism theoretically guarantees the RCM point, the RMS error at this point was approximately 0.47 mm. This value included an initial setting error, which was associated with the positioning of the pairs of the linear actuators, a mechanical assembly tolerance, and an OTS error. The error can be compared to the RCM accuracy of a stereotactic neurosurgical frame that is approximately equal to 1.7 mm [75]. Therefore, we consider that the RCM accuracy of 0.47 mm is promising for the bone drilling applications.

Unlike the reported drilling robots that use high-performance motors [76, 77], we tried to mechanically improve the rigidity of the RCM mechanism based on its robust structure against an applied force. In principle, (2)–(4) show that the required motor torque is dramatically reduced by approximately 100 times compared to the parallelogram or the arc-guide RCM type. In addition, (1) shows that the proposed mechanism has a resolution that is enhanced by approximately 300 times compared to the original motor resolution, while the parallelogram RCM has the same resolution as the motor's resolution. This indicates the proposed RCM mechanism is capable of high-precision movements. The arc-guide RCM resolution depends on the manufactured arc gear and the level of backlash between the arc and the spur gears. Therefore, the proposed gearless arc-guide can be an alternative for bone drilling purposes.

In most drilling mechanisms, the drill tip is directly connected to the actuator part, such as the rotary and linear motors. This connection makes it difficult to stop the drilling motion instantly and remove the drill tip from the robot in emergency situations. To stop and remove the drill, the operator has to turn off the power and remove the entire robot with the drill. To address this undesired connection between the drill and the robot, we adopted the rolling friction [68]. Given that the rolling friction generates the drilling motion, it can stop the force transmission and detach the drill tip immediately by lifting up the rollers. This enhances the surgical safety. In addition, we reduced the number of the motors in this study from two to one, while we maintained the performance. This contributes to the low-cost, compactness, and no need for synchronization of the motors.

In fact, various robotic systems have been developed and reported only for bone drilling [10]-[15]. This is because manual drilling has critical problems, as described in Introduction. For example, the average error in bi-cortical drilling manipulations is as large as 6.31 mm [8]. It results in breaking tendons or blood vessels and damaging critical tissue. Such problems concern the precision and accuracy of the drilled holes [8][9], the improvement of which was aimed by our proposed robot. In the ex vivo bone drilling test, the drilling accuracy was 1.11 mm. This included the patient-to-image registration error, which was equal to 0.38 mm, the pre-CT-to-post-CT registration error, which was equal to 0.28 mm, the OTS error, which was approximately equal to 0.2 mm, and other minor factors, such as the deformations of mechanical parts. Considering that the average target lesion size of the bone biopsy is approximately 31 mm [78], we could conclude that the drilling accuracy of 1.11 mm (which is 4% of the target size) is acceptable for the patient.

We also expect that the proposed system can be utilized in the future for other bone-related applications, such as screw insertions in the pedicle and stereotactic brain surgery following necessary modifications and improvements. The proposed system can be used to only guide the drilling orientation by separating the drilling mechanism, and could apply the previous drilling mechanism for more compact size. In addition, given that the proposed RCM mechanism has a submillimeter resolution, it could be applied to endomicroscopic scanning robots in minimally invasive procedures [79].

VII. CONCLUSION AND FUTURE WORK

We developed a compact bone drilling robotic system using advanced RCM and drilling mechanisms with CT image guidance. To ensure RCM with high resolution and rigidity, we utilized two sets of linear actuators and a gearless arc-guide. The experimental results showed that the proposed bone drilling robotic system could provide higher accuracy, 1.11 mm, and rigidity, 50N, than the required specifications for bone drilling. A single, motor-driven, rolling friction mechanism was also proposed to achieve simultaneous rotation and translation motions of the drill with instant drill detachment. In the ex vivo drilling tests on swine femurs the proposed RCM mechanism was capable of maintaining the drilling force and precisely guiding the orientation with errors, which were less than 5% of the target size. Accordingly, this exemplifies the potential of the system for use in bone drilling applications.

References

[1] S. Malempati et al., “Bone marrow aspiration and biopsy,” *New Engl. J. Med.*, vol. 361, no. 15, pp. 182–183, Oct. 2009.

[2] S. G. Leffler and F. S. Chew, “CT-guided percutaneous biopsy of sclerotic bone lesions diagnostic yield and accuracy,” *Am. J. Roentgenology*,” vol. 172, no. 5, pp. 1389–1392, May 1999.

[3] B. Allotta, G. Giacalone, and L. Rinaldi, “A hand-held drilling tool for orthopedic surgery,” *IEEE/ASME Trans. Mechatron.*, vol. 2, no. 4, pp. 218–229, Dec. 1997.

[4] M. Louredo, I. Díaz, and J. J. Gil, “DRIBON: A mechatronic bone drilling tool,” *Mechatronics*, vol. 22, no. 8, pp. 1060–1066, Dec. 2012.

[5] D. Van Steenberghe et al., “Accuracy of drilling guides for transfer from three-dimensional CT-based planning to placement of zygoma implants in human cadavers,” *Clin. Oral Implants Res.*, vol. 14, no. 1, pp. 131–136, Feb. 2003.

[6] J. A. Smith et al., “30 years of neurosurgical robots: review and trends for manipulators and associated navigational systems,” *Ann. Biomed. Eng.*, vol. 44, no. 4, pp. 836–846, Oct. 2015.

[7] F. Roser, M. Tatagiba, G. Maier, “Spinal robotics current applications and future perspectives,” *Neurosurgery*, vol. 72, issue suppl. 1, pp. A12–A18, Jan. 2013.

[8] G. Boiadjiev et al., “Automatic bone drilling-more precise, reliable and safe manipulation in the orthopaedic surgery,” *J. Theor. Appl. Mech.*, vol. 46, no. 2, pp. 51–64, Apr. 2016.

[9] G. Molliqaj et al., “Accuracy of robot-guided versus freehand fluoroscopy-assisted pedicle screw insertion in thoracolumbar spinal surgery,” *Neurosurg. Focus*, vol. 42, no. 5, pp. E14, May 2017.

[10] S. Tauscher et al., “High-accuracy drilling with an image guided light weight robot: autonomous versus intuitive feed control,” *Int. J. Comput. Assist. Radiol. Surg.*, vol. 12, no. 12, pp. 1763–1773, Oct. 2017.

[11] C.-C. Lin et al., “Neurosurgical robotic arm drilling navigation system,” *Int. J. Med. Robot.*, vol. 3, no. 3, Sep. 2016.

[12] W-Y Lee and C-L Shih, “Control and breakthrough detection of a three-axis robotic bone drilling system,” *Mechatronics*, vol, 16, no. 2, pp. 73–84, Mar. 2006.

[13] H. Jin et al., “Kinematics and cooperative control of a robotic spinal surgery system,” *Robotica*, vol. 34. no. 01, pp. 226–242, Jan. 2016.

[14] G. B. Chung, et al., “An image-guided robotic surgery system for spinal fusion,” *Int. J. Control Autom. Syst.,* vol. 4, no. 1, pp. 30–41, Feb. 2006.

[15] Lee J et al., “Cooperative robotic assistant with drill-by-wire end-effector for spinal fusion surgery,” *Indust. Robot Int. J. 2009*, vol. 36, no. 1, pp. 60–72.

[16] R. Taylor et al., “A telerobotic assistant for laparoscopic surgery,” *IEEE Engineering in Medicine and Biology Magazine*, vol. 14, no. 3, pp. 279–288, 1995.

[17] P. Li et al., “Development of a robotic endoscope holder for nasal surgery,” in *Proc. Information and Automation (ICIA) IEEE International Conference*, 2013, pp. 1194–1199.

[18] J. Rosen et al., “The BlueDRAGON—A system for measuring the kinematics and the dynamics of minimally invasive surgical tools in-vivo,” in *Proc. IEEE Int. Conf. Robotics and Automation*, 2002, pp. 1876–1881.

[19] G. Zong et al., “Classification and type synthesis of 1-DoF remote center of motion mechanisms,” *Mech. Mach. Theory*, vol. 43, pp. 1585–1595, Dec. 2008.

[20] P. Berkelman and J. Ma, “A compact modular teleoperated robotic system for laparoscopic surgery,” *Int. J. Robotics Res.*, vol. 28, pp. 1198–1215, 2009.

[21] P. Berkelman et al., “Ler: The light endoscope robot,” Presented at the 2003 IEEE/RSJ International Conf. Intelligent Robots Syst., (IROS 2003), Oct. 2003, vol. 3, pp. 2835–2840.

[22] N. Hata, K. Masamune, E. Kobayashi, et al., “Needle insertion manipulator for CT- and MR-guided stereotactic neurosurgery,” *in Interventional MR: Techniques and Clinical Experience*, F. A. Jolesz, I. R. Young Eds. London: Martin Dunitz, 1998, pp. 99–106.

[23] S. Shim, S. Lee, D. Ji, et al., “Trigonometric ratio-based remote center of motion mechanism for bone drilling,” in *Proc. IEEE/RSJ Int. Conf. Intell. Robot. Syst. (IROS)*, Madrid, 2018, pp. 4958–4963.

[24] Y. Kasahara, H. Kawana, S. Usuda, and K. Ohnishi, “Telerobotic-assisted bone-drilling system using bilateral control with feed operation scaling and cutting force scaling,” *Int. J. Med. Robot*., vol. 8, no. 2, pp. 221–229, June 2012.

[25] Y. L. Hsu, S. T. Lee, and H. W. Lin, “A modular mechatronic system for automatic bone drilling,” *Biomed. Eng. App. Bas. C*., vol. 13, no. 4, pp. 168–174, Aug. 2001.

[26] I. Díaz, J. J. Gil, and & M. Louredo, “Bone drilling methodology and tool based on position measurements,” *computer methods and programs in biomedicine*, vol. 112, no. 2, pp. 284-292, Nov. 2013.

[27] G. B. Chung, S. Kim, S. G. Lee, B. J. Yi, W. Kim, S. M. Oh, Y. S. Kim, B. R. So, J. I. Park, and S. H. Oh, “An image-guided robotic surgery system for spinal fusion,” *Int. J. Control Autom. Syst*., vol. 4, no. 1, pp. 30–41, Feb. 2006.

[28] J. Lee, I. Hwang, K. Kim, S. Choi, W. K. Chung, Y. S. Kim, “Cooperative robotic assistant with drill-by-wire end-effector for spinal fusion surgery,” *Indust. Robot. Int. J*., vol. 36, no. 1, pp. 60–72, Jan. 2009.

[29] W.-Y. Lee and C.-L. Shih, “Control and breakthrough detection of a three-axis robotic bone drilling system,” *Mechatronics*, vol. 16, no. 2, pp. 73–84, Mar. 2006.

[30] J. Long, P. Cinquin, J. Troccaz, S. Voros, P. Berkelman, J. Descotes, C. Letoublon, and J. Rambeaud, “Development of miniaturized light endoscope-holder robot for laparoscopic surgery,” *Journal of Endourology*, vol. 21, no. 8, pp. 911-914, Sep. 2007

[31] Y. Chen, A. Squires, R. Seifabadi, S. Xu, H. Agarwal, M. Bernardo, P. Pinto, P. Choyke, B. Wood, and Z. Tse, “Robotic System for MRI-guided Focal Laser Ablation in the Prostate,” *IEEE/ASME Trans. Mechatronics*, vol. 22, no. 1, pp. 107–114, Feb. 2017.

[32] E. Franco, D. Brujic, M. Rea, W. M. Gedroyc, and M. Ristic, “Needleguiding robot for laser ablation of liver tumors under mri guidance,” *IEEE/ASME Trans. Mechatronics*, vol. 21, no. 2, pp. 931–944, Apr. 2016.

[33] C. R. Maurer, J. M. Fitzpatrick, M. Y. Wang, R. L. Galloway, R. J. Maciunas, and G. S. Allen, “Registration of head volume images using implantable fiducial markers,” *IEEE transactions on medical imaging*, vol. 16, no. 4, pp. 447-462, Aug. 1997.

[34] T. Ortmaier, H. Weiß, U. Hagn, M. Grebenstein, M. Nickl, A. Albu-Schaffer, C. Ott, S. Jorg, R. Konietschke, L. Le-Tien, and G. Hirzinger, “A hands-on-robot for accurate placement of pedicle screws,” in Proc. 2006 IEEE Int. Conf. Robot. Autom., Orlando, FL, May 2006, pp. 4179–4186.

[35] P. Centore, “The coefficient of variation as a measure of spectrophotometric repeatability,” *Color Res. Appl*., vol. 41, no. 6, pp. 571–579, Dec. 2016.

[36] Y. Chen, I. S. Godage, Z. T. H. Tse, R. J. Webster and E. J. Barth, "Characterization and Control of a Pneumatic Motor for MR-Conditional Robotic Applications," *IEEE/ASME Trans. Mechatronics*, vol. 22, no. 6, pp. 2780-2789, Dec. 2017

[37] J. Aerssens, S. Boonen, G. Lowet, and J. Dequeker, “Interspecies differences in bone composition, density, and quality: Potential implications for in vivo bone research,” *Endocrinology*, vol. 139, no. 2, pp. 663–670, Feb. 1998.

[38] F. Stelzle, C. Frenkel, M. Riemann, C. Knipfer, P. Stockmann, and E. Nkenke, “The effect of load on heat production, thermal effects and expenditure of time during implant site preparation–an experimental ex vivo comparison between piezosurgery and conventional drilling,” *Clin. Oral. Implants Res*., vol. 25, no. 2, pp. 140-148, Nov. 2012.

[39] L. Xu, C. Wang, M. Jiang, H. He, Y. Song, H. Chen, J. Shen, and J. Zhang, “Drilling force and temperature of bone under dry and physiological drilling conditions,” *Chin. J. Mech. Eng*., vol. 27, no. 6, pp. 1240–1248, Nov. 2014.

[40] B. Allotta, F. Belmonte, L. Bosio, and P. Dario, “Study on a mechatronic tool for drilling in the osteosynthesis of long bones: Tool/bone interaction, modeling and experiments,” *Mechatronics*, vol. 6, no. 4, pp. 447–459, June 1996.

[41] J. Fitzpatrick, J. West, and C. Maurer. "Predicting error in rigid-body point-based registration." *IEEE transactions on medical imaging*, vol. 17, no. 5, pp. 694-702, Oct 1998.

[42] D. Stoianovici, L. L. Whitcomb, J. H. Anderson, R. H. Taylor, and L. R. Kavoussi, “A modular surgical robotic system for image guided percutaneous procedures,” in *International Conference on Medical Image Computing and Computer-Assisted Intervention*, Berlin/Heidelberg, Germany: Springer, 1998, pp. 404–410.

[43] M. J. S. Maciel, C. J. Tyng, P. N. V. P. Barbosa, A. G. V. Bitencourt, J. P. K. Matushita, Jr., C. E. Zurstrassen, W. T. Chung, and R. Chojniak, "Computed tomography-guided percutaneous biopsy of bone lesions: Rate of diagnostic success and complications," *Radiol. Bras.*, vol. 47, no. 5, pp. 269–274, Oct. 2014

[44] P. Berkelman and J. Ma, "A compact modular teleoperated robotic system for laparoscopic surgery," *The International Journal of Robotics Research*, vol. 28, pp. 1198–1215, 2009.

[45] P. Berkelman, E. Boidard, P. Cinquin, and J. Troccaz, "Ler: The light endoscope robot," in *2003 IEEE/RSJ International Conference on Intelligent Robots and Systems*, (IROS 2003), vol. 3, pp. 2835–2840. Oct. 2003.

[46] S. Harris, Q. Mei, R. Hibberd, and B. Davies, "Experiences using a special purpose robot for prostate resection," *in Advanced Robotics, 1997. ICAR* '97. Proceedings, 8th International Conference on, July 1997, pp. 161–166.

[47] N. Hata, K. Masamune, E. Kobayashi, et al., "Needle insertion manipulator for CT- and MR-guided stereotactic neurosurgery," In Interventional MR: Techniques and Clinical Experience, Jolesz FA, Young IR (eds). Martin Dunitz: London, pp. 99–106, 1998.

[48] R. Taylor, J. Funda, B. Eldridge, S. Gomory, K. Gruben, D. LaRose, M. Talamini, L. Kavoussi, and J. Anderson, "A telerobotic assistant for laparoscopic surgery," *Engineering in Medicine and Biology Magazine*, IEEE, vol. 14, no. 3, pp. 279–288, 1995

[49] P. Li, H. M. Yip, D. Navarro-Alarcon, Y. Liu, C. Tong, and I. Leung, "Development of a robotic endoscope holder for nasal surgery," in *Information and Automation (ICIA)*, 2013 IEEE International Conference on, pp. 1194–1199, Aug. 2013.

[50] J. Rosen, J. D. Brown, L. Chang, et al., "The BlueDRAGON—A system for measuring the kinematics and the dynamics of minimally invasive surgical tools in-vivo," In *Proceedings of IEEE International Conference on Robotics and Automation*, pp. 1876–1881, May 2002.

[51] D. Stoianovici, L. L. Whitcomb, J. H. Anderson, et al., "A modular surgical robotic system for image guided percutaneous procedures," In *Proceedings of Medical Image Computing and Computer-Assisted Intervention* - MICCAI '98, Cambridge, MA, USA, pp. 404–410, 11–13 October 1998.

[52] Center robotic arm with five-bar spherical linkage for endoscopic camera, by B. Schena. (2007). International Patent No. WO2007114975.

[53] J. S. Navarro, N. Garcia, C. Perez, et al., "Kinematics of a robotic 3UPS1S spherical wrist designed for laparoscopic applications," *Int J Med Robotics Comput Assist Surg,* vol. 6, no. 3, pp. 291-300, 2010.

[54] A. C. Lehman, M. M. Tiwari, B. C. Shah, et al., "Recent advances in the CoBRASurge robotic manipulator and dexterous miniature in vivo robotics for minimally invasive surgery," Proc *IME, Part C: J Mech Eng Sci*, vol. 224, no. 7, pp. 1487–1494, 2010.

[55] C.-H. Kuo, J. S. Dai, and P. Dasgupta, "Kinematic design considerations for minimally invasive surgical robots: an overview," *Int. J. Med. Rob. Comput. Assist. Surg*, vol. 8, no. 2, pp. 127–145, 2012.

[56] J. Li, Y. Xing, K. Liang, and S. Wang, "Kinematic design of a novel spatial remote center-of-motion mechanism for minimally invasive surgical robot," *ASME. J. Med. Devices*, vol. 9, no. 1, pp. 011003, 2015.

[57] G. Zong, X. Pei, J. Yu, and S. Bi, "Classification and type synthesis of 1-DoF remote center of motion mechanisms," *Mechanism and Machine Theory*, vol. 43, pp. 1585–1595, 2008.

[58] H. M. Yip, Z. Wang, D. Navarro-Alarcon, P. Li, Y.-H. Liu, and T. Cheung, "A new robotic uterine positioner for laparoscopic hysterectomy with passive safety mechanisms: Design and experiments," in Proc. *IEEE/RSJ Int. Conf. Intell. Robots Syst*., 2015, pp. 3188–3194.

[59] D. Kim, E. Kobayashi, T. Dohi, and I Sakuma, "A new, compact MRcompatible surgical manipulator for minimally invasive liver surgery," In *Proceedings of Medical Image Computing and ComputerAssisted Intervention* - MICCAI 2002. : Tokyo, Japan, 25–28 September 2002, pp. 99–106.

[60] A. Wolf, M. Shoham, M. Schnider, and M. Roffman, "Feasibility study of a mini, bone-attached, robotic system for spinal operations: Analysis and experiments," *Spine*, vol. 29, no. 2, pp. 220–228, 2004.

[61] H. Jaesung, N. Matsumoto, R. Ouchida, S. Komune, and M. Hashizume, "Medical navigation system for otologic surgery based on hybrid registration and virtual intraoperative computed tomography*," IEEE Trans. Biomed. Eng*., vol. 56, no. 2, pp. 426–432, Feb. 2009.

[62] T. Ortmaier, H. Weiss, S. Dobele, and U. Schreiber, “Experiments on ¨ robot-assisted navigated drilling and milling of bones for pedicle screw placement,” *Int. J. Med. Robot. Comput. Assisted Surg*., vol. 2, pp. 350–363, 2006.

[63] J. Bos, M. Steinbuch, and H. P. M. Kunst, “A new image guided surgical robot for precision bone sculpturing” Proceedings of the *16th International Conference of the European Society for Precision Engineering and Nanotechnology*, EUSPEN 2016, pp. 1-2, May. 2016.

[64] M. J. S. Maciel, C. J. Tyng, P. N. V. P. Barbosa, A. G. V. Bitencourt, J. P. K. Matushita, Jr., C. E. Zurstrassen, W. T. Chung, and R. Chojniak, “Computed tomography-guided percutaneous biopsy of bone lesions: Rate of diagnostic success and complications,” *Radiol. Bras*., vol. 47, no. 5, pp. 269–274, Oct. 2014.

[65] A. D. Wiles, D. G. Thomson, and D. D. Frantz, “Accuracy assessment and interpretation for optical tracking systems,” in Proc. *SPIE Med. Imag*., Visualizat., Image-Guided Proced., Display, 2004, vol. 5367, pp. 421–432.

[66] A. Bertelsen, J. Melo, E. Sánchez, and D. Borro, “A review of surgical robots for spinal interventions,” *Int. J. Med. Robot*., vol. 9, no. 4, pp. 407–422, Dec. 2013.

[67] A. Wolf et al., “Feasibility study of a mini, bone-attached, robotic system for spinal operations: Analysis and experiments,” *Spine*, vol. 29, no. 2, pp. 220–228, Jan. 2004.

[68] S. Shim et al., "Robotic system for bone drilling using a rolling friction mechanism," *IEEE/ASME Trans. Mechatronics*, vol. 23, no. 5, pp. 2295–2305, Oct. 2018.

[69] B. K. Horn, “Closed-form solution of absolute orientation using unit quaternions,” *JOSA A*, vol.4, pp. 629–642, 1987.

[70] P. Centore, “The coefficient of variation as a measure of spectrophotometric repeatability,” *Color Res. Appl.*, vol. 41, no. 6, pp. 571–579, Dec. 2016.

[71] J. Aerssens et al., “Interspecies differences in bone composition, density, and quality: Potential implications for in vivo bone research,” *Endocrinology*, vol. 139, no. 2, pp. 663–670, Feb. 1998.

[72] Y. Li et al., “Bone defect animal models for testing efficacy of bone substitute biomaterials,” *J. Orthop. Transl.*, vo. 3, no. 3, pp. 95–104, Jul. 2015.

[73] B. Allotta et al., “Study on a mechatronic tool for drilling in the osteosynthesis of long bones: Tool/bone interaction, modeling and experiments,” *Mechatronics*, vol. 6, no. 4, pp. 447–459, June 1996.

[74] L. Xu et al., “Drilling force and temperature of bone under dry and physiological drilling conditions,” *Chin. J. Mech. Eng.*, vol. 27, no. 6, pp. 1240–1248, Nov. 2014.

[75] C. J. Nycz et al., “Mechanical validation of an MRI compatible stereotactic neurosurgery robot in preparation for pre-clinical trials,” in *Proc. IEEE/RSJ Int. Conf. Intell. Robot. and Syst. (IROS)*, Vancouver, BC, 2017, pp. 1677–1684.

[76] T. Ortmaier et al., “Experiments on ¨ robot-assisted navigated drilling and milling of bones for pedicle screw placement,” *Int. J. Med. Robot. Comput. Assist. Surg.*, vol. 2, pp. 350– 363, Dec. 2006.

[77] J. Bos, M. Steinbuch, and H. P. M. Kunst, “A new image guided surgical robot for precision bone sculpturing” in *Proc. 16th Int. Conf. Eur. Soc. Precis. Eng. Nanotechnol*., EUSPEN 2016, pp. 1–2.

[78] M. J. S. Maciel et al., “Computed tomography-guided percutaneous biopsy of bone lesions: Rate of diagnostic success and complications,” *Radiol. Bras*., vol. 47, no. 5, pp. 269–274, Oct. 2014.

[79] P. Giataganas, et al., “Intraoperative robotic-assisted large-area high-speed microscopic imaging and intervention,” *IEEE Trans. Biomed. Eng.*, vol. 66, no. 1, pp. 208–216, Jan. 2019.

요 약 문

높은 강성을 갖는 소형 뼈 천공 로봇 시스템

본 연구에서 뼈 천공 수술을 위한 천공 메커니즘, 가이드 메커니즘, 그리고 네비게이션 시스템을 개발하였다. 이전에 제안되었던 직선과 회전 모터를 따로 사용하는 천공 메커니즘들과 달리 회전모터만을 사용하는 마찰력 기반의 천공 메커니즘을 제안하였다. 이로써 직선 가이드 없이도 천공 운동을 구현 할 수 있기 때문에 로봇의 크기를 줄 일 수 있었으며, 로봇과 드릴의 기계적인 채결이 필요 없기 때문에 위급상황 시에 간단하게 드릴의 움직임을 중단하고 제거할 수 있게 되었다. 또한, 볼 나사 기반의 직선 엑추에이터 기반의 RCM (Remote Center of Motion) 메커니즘을 개발하였다. 뼈 천공 수술에서 가장 중요하고 어려운 작업 중 하나는 목표 지점까지 드릴의 방향을 가이드해주고 천공 중에 발생할 수 있는 반력에 삽입 방향을 유지하는 것이다. 천공의 방향을 가이드해주기 위해 초기 삽입 지점을 유지하면서 방향을 목표 지점에 정렬해 줄 수 있는 RCM 메커니즘이 적합하다. 그러나 기존의 RCM 메커니즘은 단단한 조직을 다루기에 충분한 정밀도나 강성을 제공하지 않는다. 우리는 직선 엑추에이터 만을 사용하는 새로운 형태의 RCM 메커니즘을 개발하여 높은 정밀도와 강성을 달성하였다. 목표 위치로의 천공 및 방향 가이드를 위해 CT 영상 기반의 네비게이션 시스템을 개발 및 통합하였다. 팬텀을 통한 일련의 기초 실험과 돼지 대퇴골을 통한 생검 실험을 통해 통합 로봇 시스템의 효과가 입증되었다. 제안된 로봇 시스템은 실제 천공에 필요한 강성의 3 배인 51 N 까지의 외력을 버티며 삽입 각도를 유지하였고, 생검 실험의 평균 천공 오차는 1.2 mm 미만이었다.

핵심어: 뼈 천공, 영상 기반 네비게이션, 원격 중심 움직임 메커니즘, 천공 메커니즘